LUMINESCENCE SPECTROSCOPY OF NATURAL AND SYNTHETIC REE-BEARING MINERALS

Henrik Friis

A Thesis Submitted for the Degree of PhD
at the
University of St. Andrews

2009

Luminescence Spectroscopy of Natural and Synthetic REE-bearing Minerals

Submitted for the degree of Doctor of Philosophy
School of Geography & Geosciences
University of St Andrews

Henrik Friis
January 13th
2009

I, Henrik Friis, hereby certify that this thesis, which is approximately 33000 words in length, has been written by me, that it is the record of work carried out by me and that it has not been submitted in any previous application for a higher degree.

date signature of candidate

I was admitted as a research student in July 2005 and as a candidate for the degree of Doctor of Philosophy in July 2005; the higher study for which this is a record was carried out in the University of St Andrews between 2005 and 2009.

date signature of candidate

I hereby certify that the candidate has fulfilled the conditions of the Resolution and Regulations appropriate for the degree of Doctor of Philosophy in the University of St Andrews and that the candidate is qualified to submit this thesis in application for that degree.

date signature of supervisor

Restricted

In submitting this thesis to the University of St Andrews we understand that we are giving permission for it to be made available for use in accordance with the regulations of the University Library for the time being in force, subject to any copyright vested in the work not being affected thereby. We also understand that the title and the abstract will be published, and that a copy of the work may be made and supplied to any bona fide library or research worker, that my thesis will be electronically accessible for personal or research use unless exempt by award of an embargo as requested below, and that the library has the right to migrate my thesis

into new electronic forms as required to ensure continued access to the thesis. We have obtained any third-party copyright permissions that may be required in order to allow such access and migration, or have requested the appropriate embargo below.
The following is an agreed request by candidate and supervisor regarding the electronic publication of this thesis:

Access to Printed copy and electronic publication of thesis through the University of St Andrews.

Embargo on all part of printed copy and electronic copy for the same fixed period of one year on the following ground:
Publication would preclude future publications

date signature of candidate

date signature of supervisor

Contents

Contents

Glossary

Glossary

apfu	Atoms Per Formula Unit
A.U.	Arbitrary Units
BEI	Backscatter Electron Image
CL	Cathodoluminescence
CT	Charge Transfer
EDS	Energy Dispersive Spectrometer
EPMA	Electron Probe Micro Analyses
EPR/ESR	Electron Paramagnetic/Spin Resonance
EXAFS	Extended X-ray Absorption Fine Structure
FTIR	Fourier Transformed Infrared Spectroscopy
IL	Ionoluminescence
IMA	International Mineralogical Association
IR	Infrared
LA-ICPMS	Laser Ablation Inductively Coupled Plasma Mass Spectrometry
LED	Light Emitting Diode
LOD	Limit of Detection
nm	Nanometre 10^{-9} m
NMR	Nuclear Magnetic Resonance
OSL	Optically Stimulated Luminescence
φ	Represents all anions in a coordination polyhedron
PL	Photoluminescence
PMT	Photo Multiplier Tube
ppb	Parts Per Billion
ppm	Parts Per Million
REE	Rare Earth Elements, only includes the Lanthanides (La-Lu)
RL	Radioluminescence
SEM	Scanning Electron Microscopy
SIMS	Secondary Ion Mass Spectrometry
SXRF	Synchrotron X-ray Fluorescence Spectroscopy
TL	Thermoluminescence
UV	Ultraviolet
V_p	Volume of a coordination polyhedron
WDS	Wavelength Dispersive Spectrometer
XRD	X-ray Diffraction
XRF	X-ray Fluorescence Spectroscopy
Å	Ångström 10^{-10} m

Abstract

Abstract

This study investigates the photoluminescence (PL), cathodoluminescence (CL), radioluminescence (RL) and ionoluminescence (IL) of natural and synthetic minerals. The natural minerals (fluorapatite, leucophanite, meliphanite and zircon) are mostly from Ilímaussaq Alkaline Complex in South Greenland, Langesundsfjord in Norway and from different localities within Scotland. Synthetic fluorapatite (manufactured as part of the present study) and zircon doped with rare earth elements (REE) were used to compare single and multidoped materials.

This study has shown that many of the generally accepted applications of luminescence are not as straightforward as often suggested by the current literature. For example, the study demonstrates how site distribution of REE, based on luminescence, is greatly affected by the dopant level and structural changes, and that different conclusions can be drawn on the same sample depending on method applied. Furthermore, it is clearly demonstrated that using luminescence as a tool for quantitative trace element determination is not going to be a standard technique in the near future if ever. The two main findings supporting this conclusion are the non-linear intensity decrease between different REE activators in the same sample and a large variation between activators at the concentration at which self-quenching starts.

In contrast to the general perception that luminescence related to REE is mostly independent of the host, this study has shown a strong interaction between host and REE activators. This conclusion is supported by the change in the activator’s coordination polyhedron observed with single-crystal and powder X-ray diffraction combined with full chemical characterisation. When combining the weak interaction between some REE with the strong host interaction this study has shown the potential for designing new types of colour tuneable and “white light” LEDs based on natural minerals. This study also reveals that zircon doped with Gd^{3+} and Eu^{3+} can potentially have quantum-cutting properties.

Introduction

Introduction

The luminescence of materials is widely studied and a simple keyword search on Web of Knowledge using “luminescence” returns 40243 hits over the last ten years. Of these only 103 are within Mineralogy, but in contrast 7954 are in Material Science. This begs the question, why study the luminescence of minerals from a mineralogical standpoint when chemists and physicist do the majority of research in the field? Can mineralogists contribute anything to the general understanding of luminescence?

Mineralogists provide particular perspectives to the study of solid state materials. Minerals have particularly high states of order, whether in terms of site allocation, defect ordering or exsolution microtextures. Minerals are also always impure systems with several simultaneous chemical substitutions, Mineralogists are therefore particularly well placed to study properties that are based around chemical substitutions, states of structural order and multidoped systems.

In the mineral kingdom, several minerals are particularly good hosts for lanthanides. Many synthetic solids with luminescence properties are mineral analogues. Here I study the luminescence properties of a suite of lanthanide bearing minerals. These are apatite, zircon and leucophanite, which are solids known to have particularly bright luminescence. I examine the properties of these systems, to understand more fully the mechanisms by which luminescence occurs in these systems, but also to gain a deeper understanding of luminescence in general.

The interest in luminescence within the Material Science community is driven by different goals to that of the Mineralogical community. Firstly, luminescent materials are used in LEDs as potential low energy light sources. Second, luminescent materials are used for dosimetry, the applications of which range from measuring the radioactive exposure, following a nuclear accident, of an area to measuring the exposure patients receive during radiation treatment for cancer. Third, luminescent materials are used in different scintillators to measure radiation intensities. For these applications the study of ‘natural’ minerals, with their complex chemistry, can supply important insights into luminescence that will not be observed in single-doped systems.

Although luminescence has been studied intensively for almost a century, many questions remain unanswered. This Thesis will investigate how different forms of excitation give different luminescence spectra for the same sample and explain how some differences arise from a general physical property usually neglected in the interpretation of luminescence spectra. Furthermore, it will investigate to what degree the REE activators interact with each other and the structure. Most studies of minerals are conducted with high-energy excitation, which generally excites most activators simultaneously and therefore, important information of REE interactions may not always be revealed.

Finally, by using both excitation and emission spectroscopy this study has identified some natural minerals that have the potential to work not only as colour tuneable LEDs, but also as close to “white light” LEDs. These properties are surprising and have only been revealed from the study of natural minerals.

As my old Professor Emil Makovicky once said in a lecture:

“Ohne Mineralogie ist alles nur Fantasie!!!”

Chapter 1

Luminescence and Minerals

Luminescence and Minerals

1.1 Aims and Objectives

The aim of this study is to evaluate and develop the current understanding of luminescence. Especially, the application of luminescence as a structural probe or for quantitative trace element analyses. Furthermore, the detailed spectroscopic analyses will explore the potential for new materials with unique luminescent properties based on natural minerals. This will be possible through the following objectives:

- compare the luminescence of natural and synthetic apatites;
- compare and contrast the luminescence of closely related mineral species, namely leucophanite and meliphanite;
- contrast the luminescence resulting from a range of excitation techniques, namely cathodoluminescence, ionoluminescence, photoluminescence and radioluminescence, of individual samples; and
- perform chemical and structural characterisation of natural and synthetic minerals to identify how chemical and structural changes may affect luminescence.

This chapter presents a brief introduction to luminescence and the samples studied, while Chapter 2 describes the analytical methods and synthesis techniques applied. Chapters 3-5 are written as independent chapters in paper form that will form the basis of material submitted for publication. Chapter 3 presents the photoluminescence of synthetic zircons; Chapter 4 combines several luminescence techniques of both natural and synthetic apatite, and the luminescence of leucophanite and meliphanite is described in Chapter 5. Chapter 6 relates all the data gathered in this study to draw together conclusions based on the individual chapters. The style of this thesis is a mixture of a classical monograph and the more continental paper style thesis. The intensity of the presented spectra cannot be compared directly as they have been scaled to generate easier understanding figures.

1.2 Luminescence

1.2.1 Terminology

Luminescence is the emission of light from a material when excited by some form of incident energy. Luminescence is caused by the structure of a material or defects, where defects can be vacancies, displaced atoms or foreign atoms in the structure. Another type of defects consist of additional electrons or holes in the valence band (Marfunin 1979). The presence of such imperfections can generate energy levels in the band-gap or “forbidden band” between the valance and conduction band (see Fig. 1.1).

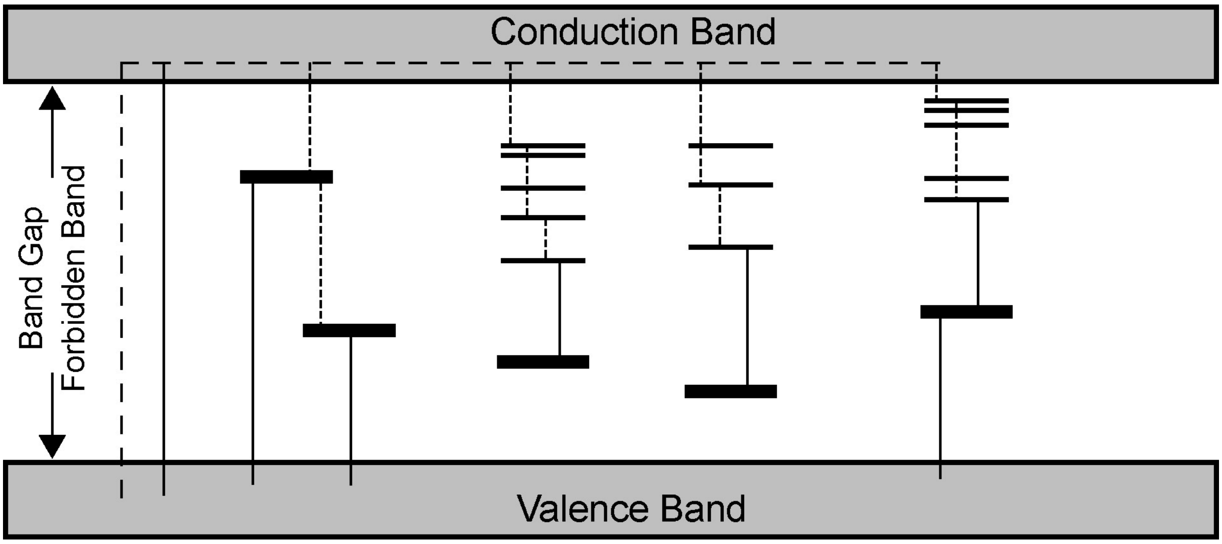

FIGURE 1.1: *Simplified sketch of the band structure of an insulator. The broken line indicates excitation from the valance to the conduction band and the free movement within the conduction band. Solid lines represent transitions that result in emission, whereas the fine dashed lines are radiationless transitions. The two thick horizontal lines to the left represent traps, and the three groups of lines represent three activators with different energy levels.*

Most non-sulfide minerals are insulators, *i.e.* band-gaps >5 eV (Marfunin 1979; Louis-Achille *et al.* 2000; Malins *et al.* 2004; and references therein), which means excitation from the valance to the conduction band is impossible by photoluminescence (PL) (typical photon energies in the UV are typically <5 eV). However, the energy levels created by the presence of defects in the material can be accessed by photoluminescence. The processes of excitation and emission are not always as straightforward as Fig. 1.1 suggests. Often energy transfer between different elements takes place and an element that transfers energy to another element, which then emits luminescence, is called a co-activator or sensitizer

(Marfunin 1979).

The wavelength of the luminescence generated depends on the energy difference between the energy levels from which the emission originates. The correlation between energy and wavelength is given by equation 1.1.

$$\lambda = \frac{hc10^{9}}{\mathrm{E}e} \qquad [1.1]$$

Where λ is the wavelength in nm, E is the energy between different energy levels in eV, *h* is Planck's constant (6.626×10^{-34} Js), *c* is the velocity of light in vacuum (2.998×10^{8} $\mathrm{ms^{-1}}$), and *e* is the charge of an electron (1.602×10^{-19} C).

Determining the wavelength of the luminescence alone is insufficient to ascribe an activator to the emission since the profile of the emission is also important. For example, $\mathrm{REE^{3+}}$ (in this thesis REE solely refers to the lanthanides La-Lu) emissions often coincide with other emissions like $\mathrm{Mn^{2+}}$ (*e.g.* Götze *et al.* 1999; Gorobets & Rogojine 2002). Emissions related to the structure, like defects, will typically show broad emission bands, as will element-activated luminescence from the transition elements, such as $\mathrm{Mn^{2+}}$ because they are linked to lattice vibrations (phonons). Since these types of emissions are connected to the structure, the peak position and width of the emission will vary from material to material depending on the degree of structure-activator interaction. Conversely, luminescence from $\mathrm{REE^{3+}}$ typically has narrow emission bands and the position of the emissions changes only subtly from material to material. In contrast to the d-group elements, the electrons causing emission from $\mathrm{REE^{3+}}$ are not valance electrons, but electrons closer to the nucleus and are therefore shielded by the valence electrons from the surrounding structure. So by combining shape and position of emission bands they can be ascribed to different activators.

1.2.2 Forms of Excitation

Most luminescence studies consider processes of excitation and emission within one structure. The majority of published studies rely on just one type of excitation; hence, beam-material interactions are rarely discussed. Using "Photoluminescence" as keyword in Web of Science between 1997 and 2007 returns

43116 hits and refining the search result with the keywords “Cathodoluminescence” or “Radioluminescence” reduces the result to 1208 and 35 hits, respectively. However, refining the original result first with “Cathodoluminescence” and subsequently with “Radioluminescence” reduces this to 4 hits. Table 1.1 summarises the luminescence techniques utilised in this study and some of their key characteristics.

TABLE 1.1. *Overview of the different excitation techniques used in this study*

Technique	Excitation	Energy	Penetration*	Power Density W/cm^2	 W/cm^3
Cathodoluminescence (CL)	Electrons	keV	<2 µm	56	56 x 10^6
Radioluminescence (RL)	X-rays	keV	Bulk	450	450
Ionoluminescence (IL)	Ions	MeV	~10 µm	0.19	190
Photoluminescence (PL)	Light	eV	Surface to bulk	0.0003$^\#$	

** Depth of penetration is material dependent and the values given are relative to each other based on leucophanite under typical excitation conditions.*

$^\#$ The power delivered at PL depends on the wavelength as the lamp used is most efficient in the blue region. As the penetration changes too, no value of power per volume is given.

Table 1.1 shows that the depth from which luminescence is generated does not necessarily correlate with the energy of the excitation source. For example, cathodoluminescence (CL) has very shallow penetration (~µm), despite high (keV) incident energy. Townsend *et al.* (1999) showed that the surface condition of a material can strongly influence the CL. Therefore, as a result CL provides information about the surface rather than the bulk material and mineral surfaces may not comply with models for the mineral bulk structure. Table 1.1 also demonstrates that although the total power delivered by CL is smaller than that delivered by radioluminescence (RL), the power density per volume is orders of magnitude greater for CL.

One of the most important, but rarely discussed, issues in understanding mineral luminescence is transparency. Most minerals are transparent in the visible (~400 – 700 nm) spectrum, but opaque in the UV region (<400 nm). This property is readily exemplified by ordinary window glass. For example, if you sit indoors in front of a window on a sunny day, you will not become sunburnt, *i.e.* the UV-radiation that causes sunburn does not pass through the window. However, when looking out through the window you can still see all the different colours outside, *i.e.* the visible region passes through the window.

As a consequence of this optical property, changes in photoluminescence as a function of excitation, may not only be caused by activation of new centres, but also by a change in the excited volume. The importance of optical absorption is therefore not only relevant for understanding excitation of the sample, but also for interpreting the subsequent emission. If a material is more absorbent in the UV than the visible region then UV luminescence generated at depth is less likely to pass through the sample and be emitted from the surface. Figure 1.2 summarises the different depths of penetration and changes in the resulting luminescence spectra of a UV opaque material.

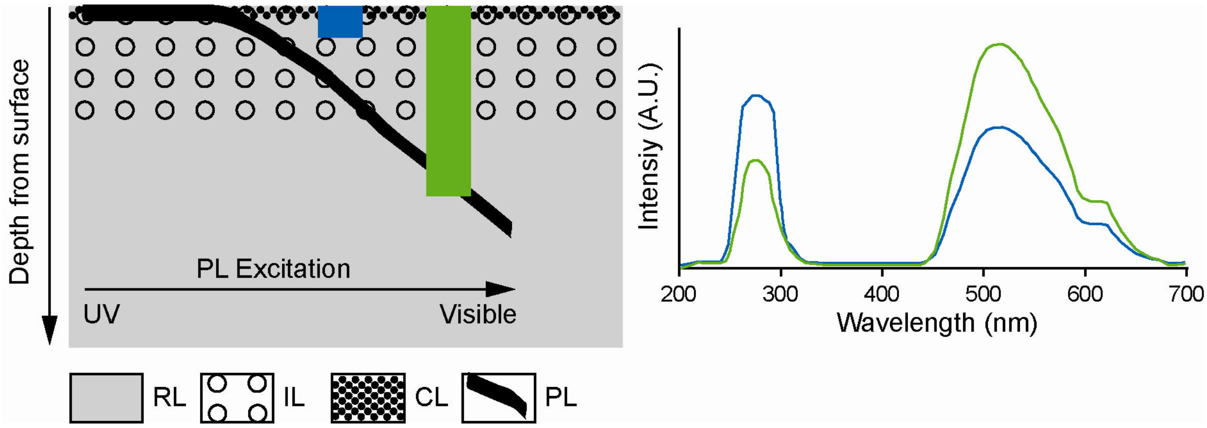

FIGURE 1.2: *Excitation and emission of a highly UV absorbent material. The depth from which luminescence is generated depends on the excitation source. For PL the excitation wavelength varies between UV to visible (left to right in the diagram). Variation in the two emission spectra is not caused by variation in composition of the two regions in which the luminescence is generated, but is solely related to UV absorption. Note: the spectra are constructed for illustrative purposes. The unit "A.U." is an abbreviation of Arbitrary Units that will be used throughout this thesis.*

With a PL system in which both excitation and emission can be controlled independently, it is possible to excite discrete energy levels of activators and traps within the band-gap. In contrast, CL, RL and IL (ionoluminescence) all have excitation energies much higher than that of the band-gap and can therefore explore luminescence arising from relaxation from, or centres close to, the conduction band. By comparing and contrasting different forms of excitation, the electronic structure above and within the band-gap is explored in the bulk, interface and surface regions of a material.

1.2.3 Applications

Luminescence is the property exploited in TV screens, phosphors, lasers and LEDs. UV-excited luminescence is widely used by amateur mineralogists as a diagnostic tool and thermoluminescence (TL) and Optically Stimulated Luminescence (OSL) of quartz and feldspar are used as a dating tool for archaeological artefacts, Quaternary sediments and lavas. Interest in mineral luminescence is driven by two goals. First, it is clear that luminescence is strongly influenced by subtle changes in composition and structural state. Therefore, changes in the physical or chemical conditions under which minerals grow are often reflected as luminescent zoning. Second, minerals grow over geological timescales and can show exceptionally high degrees of site and defect ordering that cannot be achieved easily in synthetic systems. Furthermore, some minerals, particularly those hosting radioactive elements, such as U and Th, can accumulate significant radiation damage (Ewing *et al.* 2003). Consequently, studies of minerals provide important insights into systems that have high degrees of ordering and/or those with substantial radiation damage that cannot be readily replicated in synthetic systems.

Due to the many technical applications of luminescence, the majority of research has focused on synthetic materials. It is clear that luminescence is an extremely sensitive structural probe, which provides detailed information about the local coordination around defects and activator ions. Some reviews of mineral luminescence have been published (*e.g.* Marfunin 1979; Marshall 1988; Pagel *et al.* 2000; Gorobets & Rogojine 2002; Gaft *et al.* 2005). In addition, chapters devoted to mineral luminescence, either as a technique or luminescence of specific minerals, can be found in some review volumes, for example Waychunas (2002) and Nasdala *et al.* (2003, 2004a).

Studies of synthetic materials are often based on a compound doped with a single activator or infrequently two. This method is excellent for exploring the host-activator interaction, but such results cannot necessarily be directly applied to the interpretation of natural mineral luminescence, not even if they have the same structure. Natural minerals often have a simple ideal formula, but they incorporate multiple trace elements, most of which can be in concentrations large enough to influence luminescence. Therefore, the complex chemistry of natural minerals can rarely be modelled as the interaction between a single defect and the lattice. However, studying minerals is an effective route for studying the interaction between several activators, *i.e.* they can be considered as multi-doped materials.

1.3 Sample Descriptions

1.3.1 Apatite

Apatite is hexagonal (*P*6$_3$/*m*) with the ideal formula $Ca_5(PO_4)_3(OH,F,Cl)$ and depending on which monovalent anion is dominant, has been named hydroxyl-, fluor- or chlorapatite (Elliott 1994). However, Burke (2008) presents a number of changes to the IMA-approved mineral naming convention among which are some members of the apatite group. According to the new nomenclature, the apatite members are called apatite-(CaOH), apatite-(CaF) and apatite-(CaCl), to emphasise chemical and structural relationships within the mineral group. However, I do not agree with this change as it complicates, rather than simplifies the naming of apatite-group minerals if the IMA "law" is followed strictly. Furthermore, the change is not applied rigorously to the mineral group, for example, belovite-(Ce) ($Sr_3NaREE(PO_4)_3F$) is a member of the apatite group and following the new IMA nomenclature should be named apatite-(NaCeSrF)-*T* (where "*T*" shows it is trigonal). However, IMA still retains the name belovite-(Ce). For these reasons I will use the old names, *e.g.* fluorapatite.

The apatite structure contains two slightly different *Ca* sites (note elements written in italics refer to a structural site) into which a large amount of di- and trivalent trace elements can be incorporated. The sites not only differ in size, but also in their site-symmetry, with *Ca1* having C_3 and *Ca2* C_S symmetry (see Figure 1.3).

The difference in site-symmetry makes it possible to use luminescence spectroscopy to evaluate REE distribution between different sites, since the intensity of luminescence derived from some energy transitions is strongly dependent on the site-symmetry. Furthermore, the site-symmetry influences the number of sub-bands anticipated for an emission band. Such studies have been carried out using Eu^{3+} in several synthetic and natural apatites and apatite-like structures (*e.g.* Blasse 1975; Jagannathan & Kottaisamy 1995; Gaft *et al.* 1997; Marimuthu *et al.* 2001; Piriou *et al.* 2001; Nasdala *et al.* 2004a; Li *et al.* 2006). Apatite has a strong CL and because the structure readily incorporates trace elements, most luminescence colours have been reported (*e.g.* Roeder *et al.* 1987; Mitchell *et al.* 1997; Barbarand & Pagel 2001; Kempe & Götze 2002). Homman *et al.* (1994) combined ionoluminescence with particle induced x-ray emission to correlate IL intensities with trace element

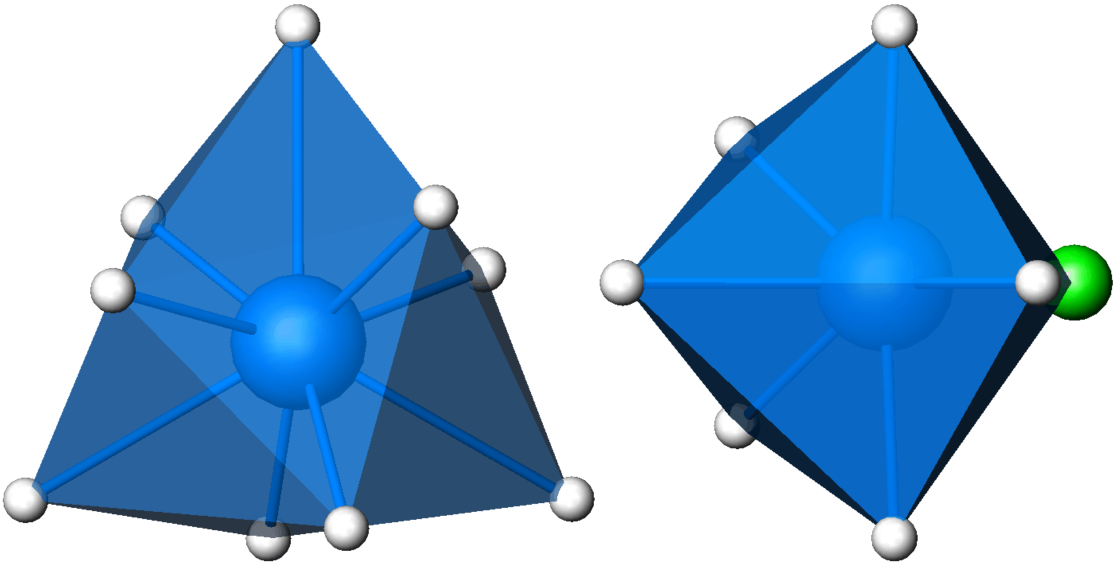

FIGURE 1.3: *The nine- and sevenfold coordination of the* Ca1 *and* Ca2 *sites in fluorapatite, respectively. The white ligands are oxygen and the green is fluorine. The figure is based on the structure solution of sample ATL (see Table 1.2).*

concentration. Data have also been published for both continuous-wave and time-resolved PL (*e.g.* Knutson *et al.* 1985; Gaft *et al.* 1997, 1999, 2001; Gorobets & Rogojine 2002; Waychunas 2002; Gaft *et al.* 2005).

The distribution of REE between the two *Ca* sites has also been the focus of several x-ray crystallographic studies that has found that the lighter REE (LREE) preferentially substitute into *Ca2*, but that the ratio of REE in *Ca2*/*Ca1* decreases with increasing atomic number of the REE (Hugh *et al.* 1991b; Fleet & Pan 1995, 1997; Comodi *et al.* 1999). In a series of EPR studies of synthetically Gd doped fluorapatites, Chen *et al.* (2002a,b) and Pan *et al.* (2002a,b) found that Gd fits into both sites, but is dependent on factors like concentration (sub ppm to >10000 ppm levels), mechanism for charge balance, type and temperature of synthesis. Fleet & Pan (1995) found that Na preferentially enters the *Ca1* site, but when the method of synthesis was altered to create a Nd-rich apatite, Na entered the *Ca2*.

Larger divalent cations (Sr and Ba) have an affinity for the *Ca2* site (Hughes *et al.* 1991a; Chakhmouradian *et al.* 2002; Rakovan & Hughes 2000). No natural mineral with the ideal end-member composition $Ca_3NaREE(PO_4)_3F$ has been described. However, three natural equivalents exist in which *Ca2* is fully replaced by Sr or Ba, namely belovite-(Ce), belovite-(La) and kuannersuite-(Ce) (Klevtsova & Borisov 1964; Pekov *et al.* 1996; Friis *et al.* 2004). REE and Na are ordered in *Ca1* splitting it into two individual sites. In both belovite and kuannersuite a significant amount of Cl replaces F, indicating that the larger Cl atom helps to stabilise the larger structure. The relationship between the presence of larger cations like Sr and Ba and the ability of the apatite structure to incorporate REE is not fully understood.

As part of the present study, comparisons are made between natural minerals and synthetic mineral analogues. Synthetic apatites can be produced by a number of methods including hydrothermal and solid-state diffusion synthesis (Long *et al.* 2008; and references therein). Many natural apatites are reported to produce growth zoning especially in hydrothermal systems (*e.g.* Rakovan 2002; and references therein and Figs. 1.5 and 1.6). Luminescence can be activated by minute (ppb-ppm) amounts of trace elements (Habermann *et al.* 1998; Götze *et al.* 1999) and therefore growth zones are clearly visible in cathodoluminescence. Hydrothermal methods assume that the partition coefficient between the liquid and crystal is constant from nucleation to final crystallisation. In reality, precipitation acts as closed-system (Rayliegh) fractionation where the composition of the resultant solid changes with time as the residual hydrothermal fluid becomes progressively enriched or depleted in REE. The zoning produced by hydrothermal synthesis is sufficiently small for many applications, but the complexity of mechanisms controlling light emission means that even a small degree of chemical or structural heterogeneity can influence the luminescence. The synthesis experiments of this study were performed using a solid-state diffusion method, to minimise these issues.

A total of 11 natural apatites have been investigated in this study. Table 1.2 gives a description of the different samples and their origin, as well as the sample abbreviations used throughout this thesis.

TABLE 1.2. *Description of apatite samples investigated*

Label	Description	Locality	Origin
AFG	Pink short prismatic crystal up to 2.5 cm across	Afghanistan	HF
ATL	Euhedral gem quality green crystal 1.5 cm big	Imilchil, Atlas Mountains, Morocco	GLAHM 111655
DUR	1 cm euhedral gem quality yellow brown crystal from	Durango, Mexico	From the exchange collection of NHM, London
GAR	Faint green gem quality crystal from the	Gardiner Alkaline Complex, East Greenland	Kindly made available by GM (no reference number)
GRA	Euhedral yellow greenish crystal up to a cm long, from an aegirin and fluorite pocket	Granit A/S, larvikite quarry, Tvedalen, Norway	Collected by HF in 2007
ILI	Light blue crystals from analcime dyke.	Kvanefjeld, Ilímaussaq Alkaline Complex, South Greenland	Kindly donated by private collector Tom Weidner
MOI	Yellow masses intergrown with quartz	North of Loch Shiel, Moidart, Scotland	GLAHM 134076
MUL	Light yellow massive with quartz and plagioclase	Ardalanish Bay, Mull, Scotland	GLAHM 134085
MUR	Euhedral whitish 1 cm crystal	Murcia, Spain	GLAHM 111113
ONT	Large dark green euhedral crystal	Ontario, Canada	HF
SHI	Light blue pebble	Port na Droigheann, Shiaba, Mull, Scotland	GLAHM 111112

HF – Author's Collection; GLAHHM – Glasgow Hunterian Museum
NHM – Natural History Museum, London; GM – Geological Museum, Copenhagen

Details of the chemical analyses used in this study can be found in Sections 2.2 and the chemical composition and formula calculations for the natural apatites are presented in Table 1.3. The natural samples were chosen due to their photoluminescence or parageneses. All but one sample (MUL), are dominated by F over Cl or OH and therefore classified as fluorapatite. MUL is slightly dominated by OH and can therefore be classified as a hydroxylapatite. The totals for GAR and ILI are very low (96.06 and 97.27 Wt.% oxide). This is a result of strong zonation and the chemical analyses being averaged over many data points where EPMA and LA-ICPMS data may not have been acquired at exactly the same points. The zonation of these samples will be described in more detail below. The trace element concentrations are presented in Table 1.4 and show that some samples have very low trace element concentrations (MUL), whereas others are enriched in REE (GRA), Sr (GAR), Mn (MOI), U (ILI) or Th (ONT).

TABLE 1.3. *Apatite compositions in wt.% and formula calculation* (apfu) *based on 13 anions*

	AFG	**ATL**	**DUR**	**GAR**	**GRA**	**ILI**	**MOI**	**MUL**	**MUR**	**ONT**	**SHI**
n	*10*	*10*	*9*	*50*	*10*	*20*	*10*	*10*	*10*	*10*	*9*
P_2O_5	42.1(4)	41.1(8)	41.6(7)	41(1)	38.4(6)	40.4(8)	41.8(8)	42.2(6)	40.4(6)	38.6(8)	40.1(7)
SiO_2	-	0.4(1)	0.20(2)	0.1(1)	1.4(5)	-	0.01(1)	-	0.15(4)	1.12(3)	0.70(4)
CaO	55.7(3)	55.1(4)	54.7(5)	52.0(7)	51.1(4)	53(2)	54.0(4)	55.6(2)	52.9(3)	54.5(3)	55.2(2)
MgO	0.01(1)	0.01(1)	0.04(1)	0.01(1)	0.01(1)	0.02(1)	0.09(1)	0.02(1)	0.23(3)	0.01(1)	-
Na_2O	-	0.02(2)	0.19(2)	0.05(5)	0.3(1)	-	0.15(3)	-	0.26(3)	0.03(2)	-
FeO	-	-	0.04(1)	-	-	-	0.44(5)	-	-	-	-
SrO*	0.25	0.08	0.05	3.22	0.12	0.19	0.03	0.09	1.02	0.19	0.34
MnO*	0.01	0.01	-	-	0.04	0.05	0.54	0.01	0.02	0.01	0.01
REE_2O_3*	0.01	0.64	0.94	0.24	5.75	1.53	0.70	-	1.71	1.77	0.35
F	2.09(9)	2.5(1)	3.3(2)	2.5(2)	3.6(2)	3.4(4)	2.8(1)	1.72(6)	3.5(3)	3.9(4)	3.1(1)
Cl	-	0.46(4)	0.29(3)	-	-	-	-	-	0.45(4)	0.04(1)	0.23(2)
SO_3	-	0.23(4)	-	-	-	-	-	-	0.07(2)	0.49(3)	0.79(6)
$H_2O^{\#}$	0.80	0.45	0.12	0.53	-	0.11	0.44	0.98	-	-	0.24
F=O	0.88	1.07	1.40	1.08	1.53	1.43	1.17	0.72	1.51	1.64	1.30
Cl=O	-	0.10	0.06	-	-	-	-	-	0.10	0.01	0.05
Total	**100.09**	**99.83**	**100.01**	**96.07**	**99.19**	**97.27**	**99.83**	**99.90**	**99.10**	**99.01**	**99.71**
apfu											
P	2.98(2)	2.93(5)	2.97(5)	3.00(8)	2.84(4)	2.95(6)	2.99(6)	2.99(4)	2.94(4)	2.81(6)	2.87(5)
Si	-	0.03(1)	0.02(1)	0.01(1)	0.12(4)	-	-	-	0.01(1)	0.09(1)	0.06(1)
Ca	5.00(3)	4.99(4)	4.94(4)	4.78(6)	4.79(4)	4.9(1)	4.88(3)	4.99(2)	4.87(3)	5.03(3)	5.00(2)
Mg	-	-	-	-	-	-	0.01(1)	-	0.02(1)	-	-
Na	-	-	0.03(1)	0.01(1)	0.05(2)	-	0.02(1)	-	0.04(1)	0.01(1)	-
Fe	-	-	-	-	-	-	0.03(1)	-	-	-	-
Mn	-	-	-	-	-	-	0.04	-	-	-	-
Sr	0.01	-	-	0.16	0.01	0.01	-	-	0.05	0.01	0.02
REE	-	0.02	0.03	0.01	0.19	0.06	0.03	-	0.05	0.06	0.01(1)
S		0.01(1)	-	-	-	-	-	-	-	0.03(1)	0.05(1)
F	0.55(2)	0.68(4)	0.89(5)	0.69(5)	1.00(8)	0.9(1)	0.74(5)	0.45(1)	0.97(9)	1.0(1)	0.83(3)
Cl	-	0.06(1)	0.04(1)	-	-	-	-	-	0.06(1)	0.01(1)	0.03(1)
OH	0.45	0.25	0.07	0.30	-	0.06	0.25	0.55	-	-	0.14

n *Number of analyses; Errors are 2σ; - Not determined, or below limit of detection;*
** From LA-ICPMS; # Determined by stoichiometry.*

TABLE 1.4. *Trace element concentration (ppm) in analysed apatite samples*

	AFG	**ATL**	**DUR**	**GAR**	**GRA**	**ILI**	**MOI**	**MUL**	**MUR**	**ONT**	**SHI**
n	*4*	*5*	*6*	*19*	*4*	*7*	*5*	*4*	*4*	*4*	*5*
Li	-	-	1	-	4	15	1	-	-	-	-
B	14	14	13	12	36	11	11	11	11	17	14
V	1	39	17	91	-	-	-	-	345	15	14
Mn	106	95	74	34	351	432	4251	97	164	128	97
Fe	138	-	277	134	143	155	1945	339	165	238	134
Zn	-	-	1	-	-	8	2	-	-	-	2
Sr	2182	714	434	28784	1075	1664	275	835	8658	1628	2881
Y	69	898	465	209	2092	7679	2869	37	617	1100	192
Ba	-	-	1	85	1	598	-	-	44	1	1
La	1	1218	2912	503	14169	355	286	1	2645	2803	550
Ce	4	1625	2995	697	21638	1073	687	3	5518	5862	1143
Pr	1	185	274	87	2229	198	101	1	803	789	166
Nd	9	776	953	381	6566	920	394	5	3636	3202	698
Sm	5	159	124	79	792	467	138	3	630	463	102
Eu	2	23	14	22	42	56	24	1	101	72	17
Gd	10	182	117	78	582	709	174	6	358	331	70
Tb	2	26	13	9	79	134	48	1	33	38	7
Dy	11	157	76	42	440	748	414	8	144	207	38
Ho	3	31	15	6	75	112	85	1	22	38	7
Er	7	86	40	12	186	251	259	3	49	101	17
Tm	1	11	5	1	23	29	42	-	6	13	2
Yb	5	61	29	6	109	165	265	1	32	77	13
Lu	1	7	4	1	11	19	31	-	4	10	2
Pb	2	1	-	1	19	36	45	9	8	58	10
Th	-	145	182	52	865	561	2	-	787	1058	174
U	-	14	6	1	5	449	87	-	3	87	11

n *Number of analyses; - Below limit of detection.*

The content of OH in the samples is based on stochiometry from the formula calculation to make $\Sigma_{(F,Cl,OH)} = 1$ (Table 1.3). To verify the presence of OH, FTIR analyses were made on a selection of samples and the spectra are presented in Fig. 1.4. AFG, ATL, MOI and MUL all have absorptions at 3535 cm^{-1}, which corresponds to OH vibration in apatite (*e.g.* Fleet & Liu 2008). Of the samples analysed with FTIR, these also have the highest content of OH based on stoichiometry, indicating that the resolution of the instrument is better than 1 Wt.% oxide. A double absorption at 1425 and 1453 cm^{-1} are observed for GRA, ONT and SHI, which corresponds to carbonate groups (Nikčević *et al.* 2004; Antonakos *et al.* 2007; Rintoul *et al.* 2007; Fleet & Liu 2008). The absorption at ~1080 cm^{-1} is related to stretching of the phosphate group.

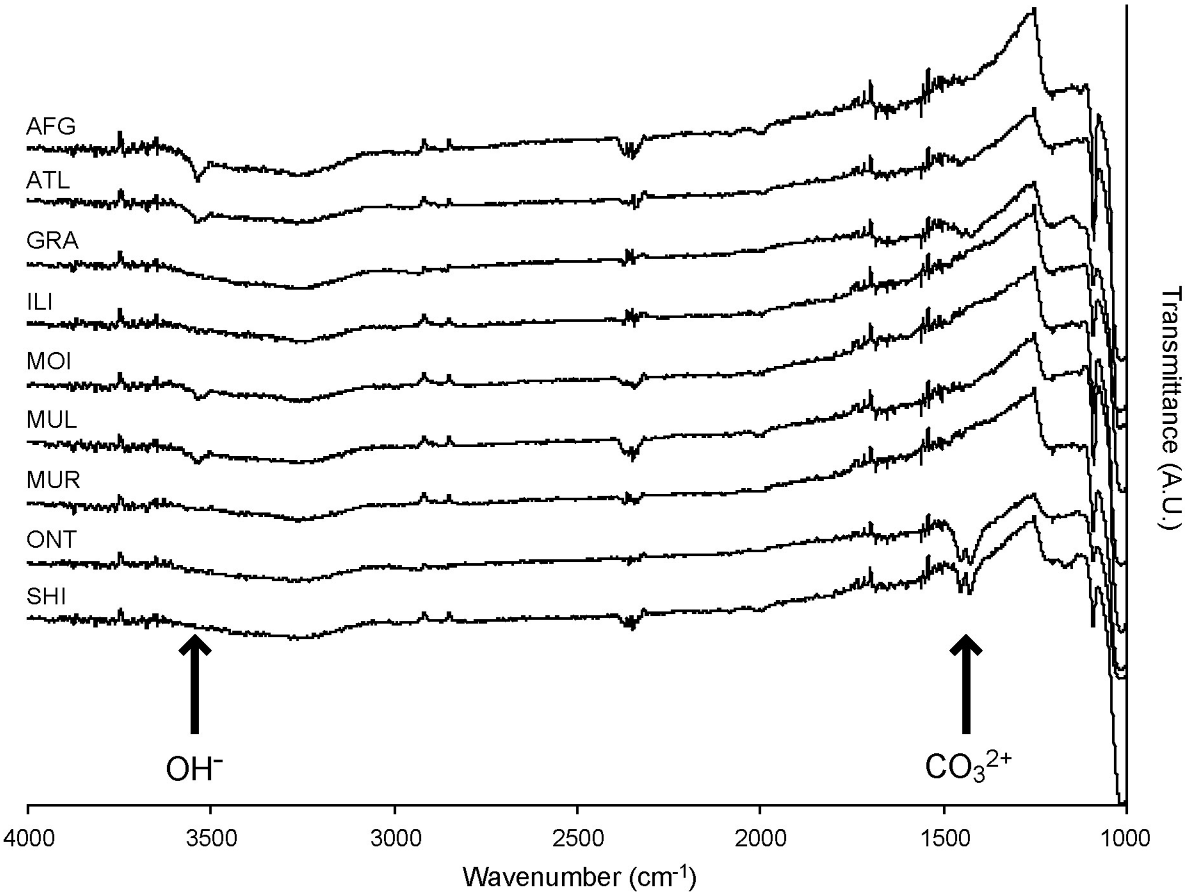

FIGURE 1.4: *FTIR spectra of a selection of analysed apatites.*

Apatite zonation

A series of spot trace element analyses were made from the rim towards the centre of a fragment of GAR cut perpendicular to the *c*-axis (Fig. 1.5).

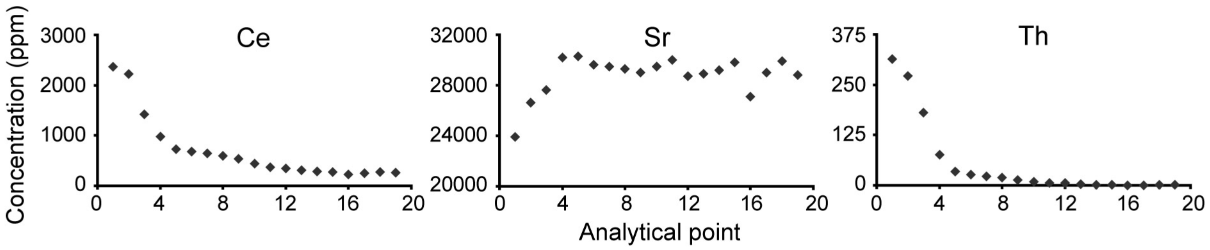

FIGURE 1.5: *Change in concentration of selected trace elements from the rim to the core of GAR.*

The concentration of Ce and Th decreases rapidly from the rim, whereas Sr increases. After the initial changes, Ce and Th continue to decrease slowly in concentration, whereas the Sr data suggest the presence of more internal zones with varying Sr concentration.

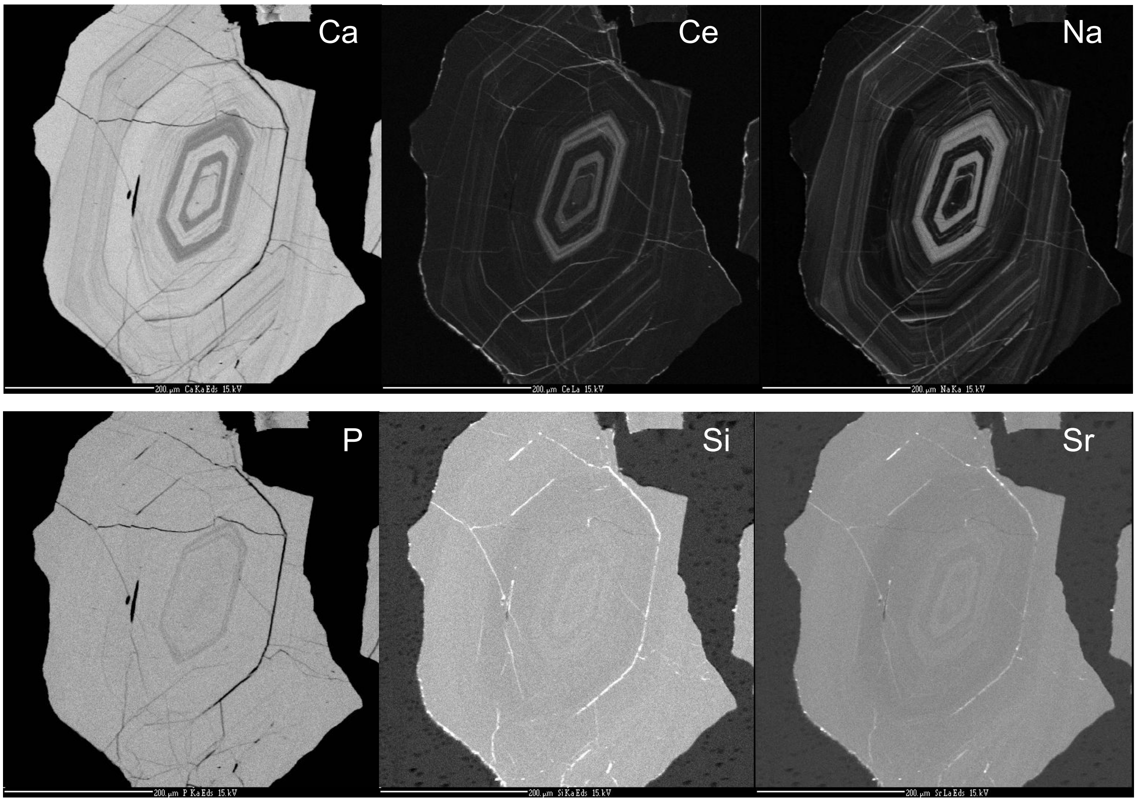

FIGURE 1.6: *EPMA element maps of a fragment of ILI. The scale bar is 200 µm.*

Fig. 1.6 demonstrates an oscillatory zonation in which Ce, Sr and Na substitute for Ca and Na balances the extra charge introduced by the Ce^{3+} for Ca^{2+} substitution. The P content does not show a great deal of variation, but it is significantly lower for the second Ce-rich zone (taken from the centre of the crystal), which also has an increased Si content. The Si-map also reveals an increase in Si within the first Ce-rich zone, but this Ce zone is not obvious in the P map. It is assumed that Si substitutes for P to charge balance, and therefore the first Ce-rich zone shows a lower P content compared to the outer zone. One explanation for the difference in P-Si maps of the two Ce-rich zones is that Si is concentrated in nanodomains of a different mineral, like britholite, in the inner Ce-rich zone.

1.3.2 Leucophanite and Meliphanite

Leucophanite, ideally $NaCaBeSi_2O_6F$, and meliphanite, ideally $Ca_4(Na,Ca)_4Be_4AlSi_7O_{24}(F,O)_4$, are chemically and structurally related and belong to the melilite group. Leucophanite is orthorhombic ($P2_12_12_1$) and meliphanite is tetragonal ($I\bar{4}$). Both minerals are found in alkaline complexes, but do not co-exist. The structural similarities and differences between the two minerals and their relation to the melilite group are described by Grice & Hawthorne (1989, 2002). Both minerals have two large cation sites (*Ca* and *Na*) that are eight-coordinated forming anti-square prisms (see Fig. 1.7).

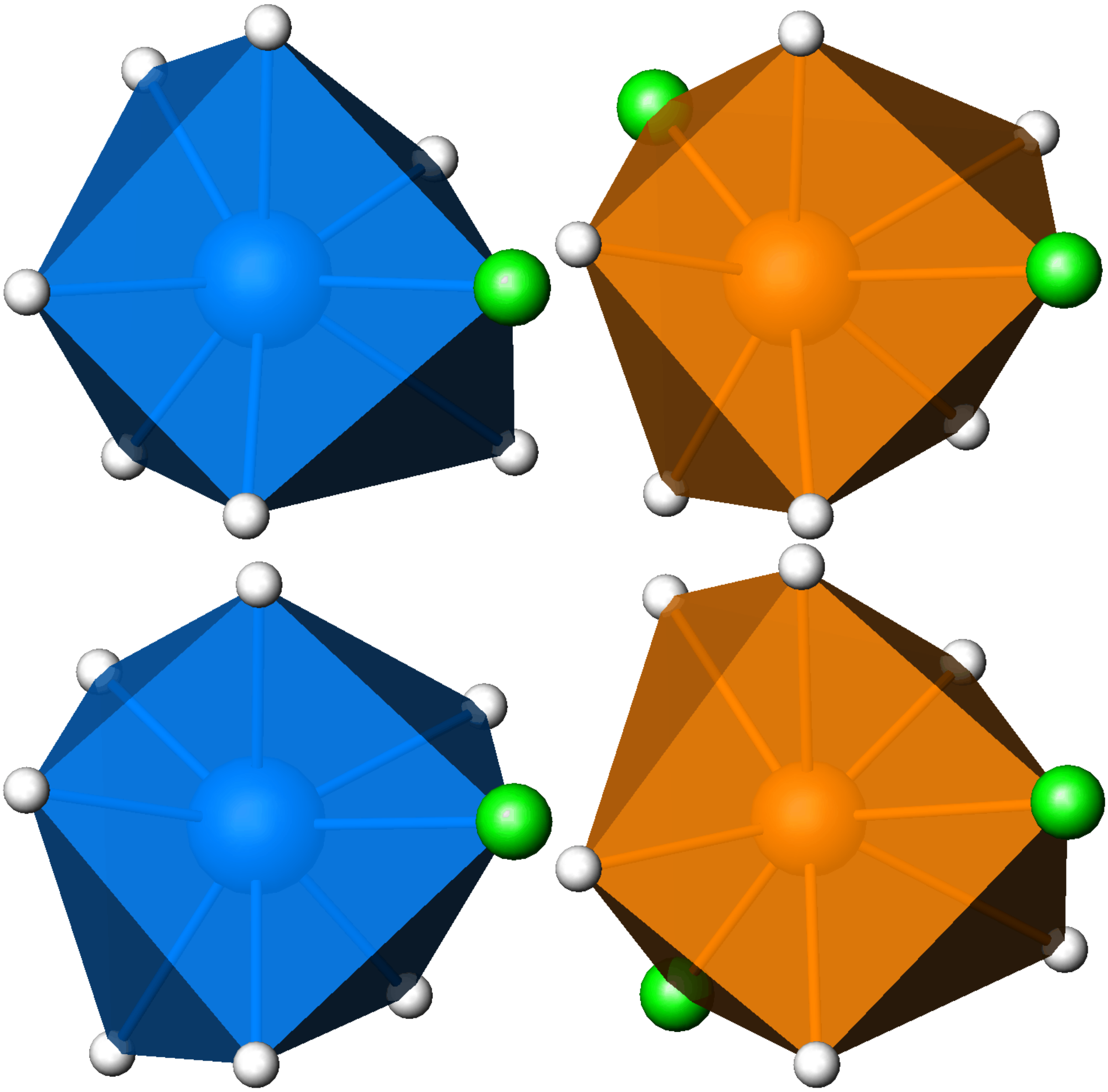

FIGURE 1.7: Ca *(blue) and* Na *(orange) coordination polyhedra for leucophanite (top) and meliphanite (bottom). White ligands are O and green are F. The structural data for leucophanite is for Leuco8 (this sample is analysed in the present study, Friis et al. 2007a) and meliphanite is from Grice & Hawthorne (2002).*

The *Ca* site is connected to one F, whereas *Na* is connected to two. Trace elements can substitute into both sites, but due to the difference in valence between the sites, it is likely that di- and higher valence cations will preferentially substitute into *Ca*. As can be seen from the formulae, the Ca/Na ratio is 1 in leucophanite but >1 in meliphanite, which may influence the mechanisms behind trace element incorporation and hence luminescent properties. Ionoluminescence of leucophanite has been published by Friis *et al.* (2007b). A detailed description of the structure and chemical effect of high REE content in leucophanite, including the samples used in this study, can be found in Friis *et al.* (2007a). For this reason only locality and chemical data for meliphanite are presented here (Tables 1.5 and 1.6).

TABLE 1.5. *Description of investigated meliphanite samples from Norway*

Label	Description	Locality	Origin
ARS	Transparent strong yellow	South end of Arøya Skjær, Langesundsfjord	AOL
BJO	Transparent yellow	Bjørndalen Quarry	AOL
HAK	Faint yellow	Håkestad Quarry, Tjølling	AOL
OST	Strong yellow	Østskogen Quarry, Tvedalen	HF
SAR	Thin faint yellow	Store Arøya, Langesundsfjord	HF
STO	Faint yellow transparent	Stoksundsholmen, Langesundsfjord	HF
TEL	Orange yellow	Telemarksporten; tunnel on E18	AOL
TRE	Whitish	Treschow Quarry, Tvedalen	AOL

AOL – Kindly provided by private collector Alf Olav Larsen
HF – Author's Collection

To investigate the Be distribution between the tetrahedral sites neutron powder data was collected for HAK and the resulting Rietveld refinement is presented in Fig. 1.8. For method description of the neutron experiment see Section 2.4.2.2. No major deviation from the structural model by Grice & Hawthorne (2002), or indication of hydrogen was observed.

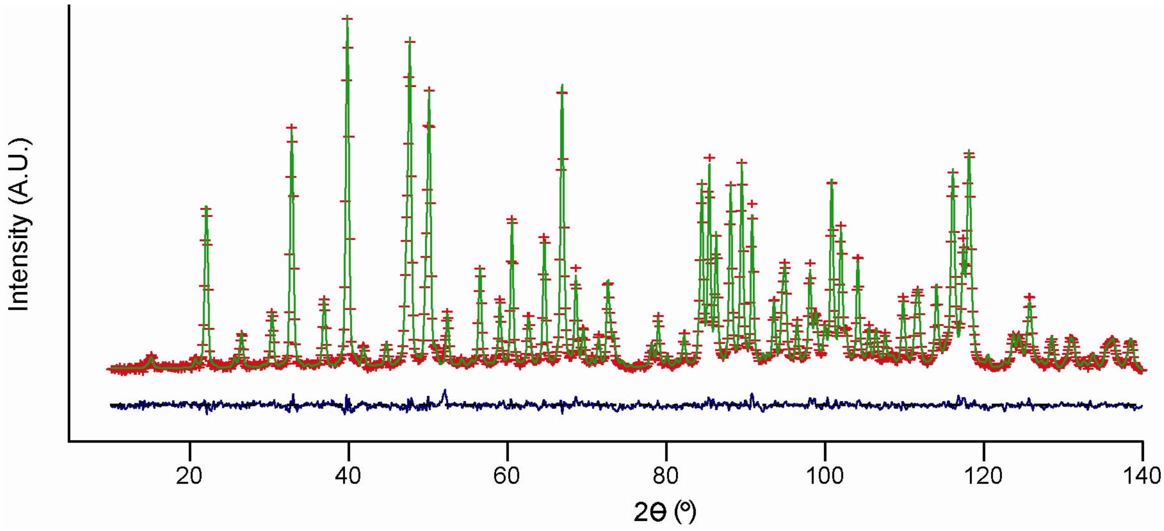

FIGURE 1.8: *GSAS refinement of the neutron powder diffraction of HAK. The crosses represent the experimental data and the full spectrum the model, with the difference plotted below the diffractogram.*

TABLE 1.6. *Meliphanite compositions in wt.% and formula calculation* (apfu) *based on 14 anions*

	ARS	**BJO**	**HAK**	**OST**	**SAR**	**STO**	**TEL**	**TRE**
n	*15*	*14*	*14*	*15*	*15*	*14*	*15*	*15*
SiO_2	42.2(1)	42.9(3)	41.8(4)	42.6(2)	41.8(2)	41.9(3)	42.6(2)	42.5(5)
Al_2O_3	4.3(1)	3.9(3)	4.12(8)	4.1(1)	4.4(1)	4.5(1)	3.98(8)	3.9(2)
CaO	30.7(3)	29.3(1)	30.0(2)	29.6(2)	31.3(2)	31.0(5)	29.9(3)	29.6(4)
Na_2O	8.1(1)	8.7(2)	8.2(1)	8.59(8)	7.7(1)	7.9(2)	8.6(1)	8.5(1)
FeO	0.16(2)	0.18(3)	0.24(4)	0.18(4)	0.17(4)	0.18(4)	0.21(3)	0.23(4)
F	6.9(1)	7.9(3)	7.6(1)	7.5(1)	7.0(1)	6.9(3)	7.4(1)	7.8(2)
SrO*	0.08	-	-	-	0.03	0.07	0.01	-
MnO*	0.05	0.24	0.46	0.28	0.08	0.06	0.14	0.22
REE_2O_3*	0.18	0.55	0.66	0.53	0.22	0.21	0.30	0.52
Li_2O	0.03	0.06	0.05	0.09	0.06	0.05	0.03	0.07
B_2O_3	0.61	0.07	0.42	0.19	0.76	0.65	0.16	0.18
$BeO^{\#}$	10.2	10.18	10.1	10.14	10.21	10.2	10.1	10.1
$H_2O^{\#}$	0.39	-	-	0.08	0.35	0.40	0.14	-
F=O	2.91	3.33	3.23	3.19	2.96	2.92	3.12	3.32
Total	**100.99**	**100.65**	**100.42**	**100.69**	**101.12**	**101.10**	**100.45**	**100.30**
apfu								
Si	3.44(1)	3.51(2)	3.45(4)	3.49(1)	3.40(2)	3.41(2)	3.50(1)	3.50(4)
Al	0.41(1)	0.38(3)	0.40(1)	0.40(1)	0.42(1)	0.43(1)	0.38(1)	0.38(1)
Ca	2.68(3)	2.57(1)	2.65(2)	2.60(2)	2.73(2)	2.71(5)	2.63(3)	2.61(4)
Na	1.28(2)	1.39(3)	1.31(1)	1.36(1)	1.22(2)	1.25(4)	1.37(1)	1.35(2)
Fe	0.01(1)	0.01(1)	0.01(1)	0.01(1)	0.01(1)	0.01(1)	0.01(1)	0.01(1)
Mn	-	0.02	0.03	0.02	0.01	-	0.01	0.02
Sr	-	-	-	-	-	-	-	-
REE	0.01	0.02	0.02	0.02	0.01	0.01	0.01	0.02
Li	0.01	0.02	0.01	0.03	0.02	0.01	0.01	0.03
B	0.08	0.01	0.05	0.02	0.11	0.09	0.02	0.03
F	1.78(4)	2.05(7)	1.99(4)	1.96(4)	1.80(4)	1.78(8)	1.92(4)	2.05(6)
OH	0.21	-	-	0.04	0.19	0.22	0.08	-
Be	2	2	2	2	2	2	2	2

n *Number of analyses; Errors are 2σ; - Not determined, or below limit of detection;* ** From LA-ICPMS;* $^{\#}$ *Determined by stoichiometry.*

Details of the trace elements and incorporation of REE in meliphanite is presented in Table 5.2. The infrared spectra for all meliphanites are presented in Figure 1.9 and are similar to that presented by Grice & Hawthorne (2002), who ascribed the absorptions between 1200 and 700 cm^{-1} to stretching of the SiO_4 tetrahedra. The spectra for all samples are similar and none show evidence for OH or H_2O.

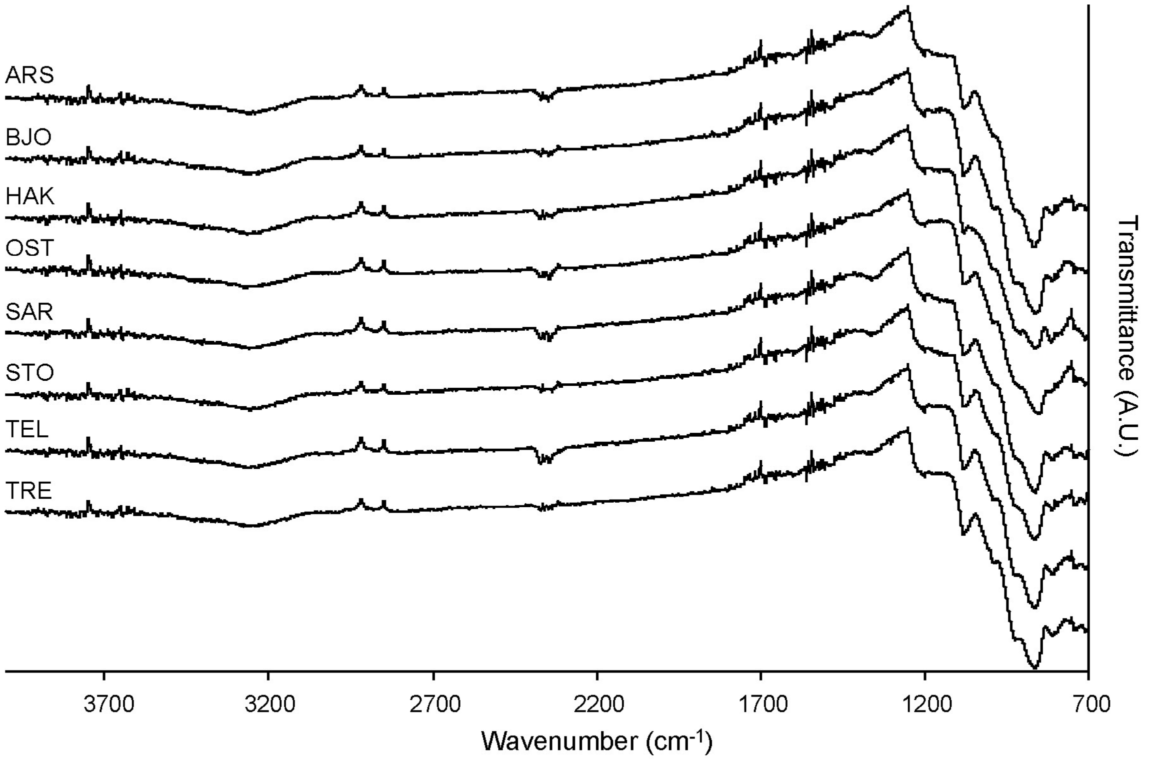

FIGURE 1.9: *FTIR spectra of meliphanite showing no evidence for OH or H_2O, which are expected at 3700-2900 or 1650-1600 cm^{-1} (Beran* et al. *2004).*

Leucophanite has been identified as a conspicuously efficient luminescent mineral under all types of excitation (Gorobets & Prokofiev 1981; Prokofiev *et al.* 1982; Gorobets & Rogojine 2002; Gaft *et al.* 2005; Friis *et al.* 2007b). It has therefore been included in this study since, for some of the methods used, enhanced signal is an important asset. In contrast, only PL and RL data have, so far, been published for meliphanite with the latter method being the only one resulting in identifiable centres (Gorobets & Rogojine 2002). A sample of meliphanite from the Langesundsfjord, Norway, showed a weak red luminescence under a normal long-wave UV-lamp, but it was intergrown with strongly luminescent microcline. An initial test of a cleavage fragment of the sample showed very weak luminescence. A recent find in the Østskogen Larvikite Quarry contained strongly red luminescent meliphanite under commercial UV-lamps. Consequently, a number of samples from several localities were collected in the Langesundsfjord region in autumn 2007 and private collector Alf Olav Larsen kindly donated several samples from old finds.

1.3.3 Zircon

Zircon, ideally $ZrSiO_4$, is one of the most studied accessory minerals in geology. Zircon is tetragonal ($I4_1/amd$) and REE readily substitutes into the eight-coordinate *Zr* site, which forms triangular dodecahedron (see Fig. 1.10). In spite of being resilient to mechanical and chemical weathering, the structure is relatively open as illustrated in Fig. 1.10. Finch & Hanchar (2003) describe two further possible distorted tetrahedral interstitial sites that may accommodate trace elements such as REE.

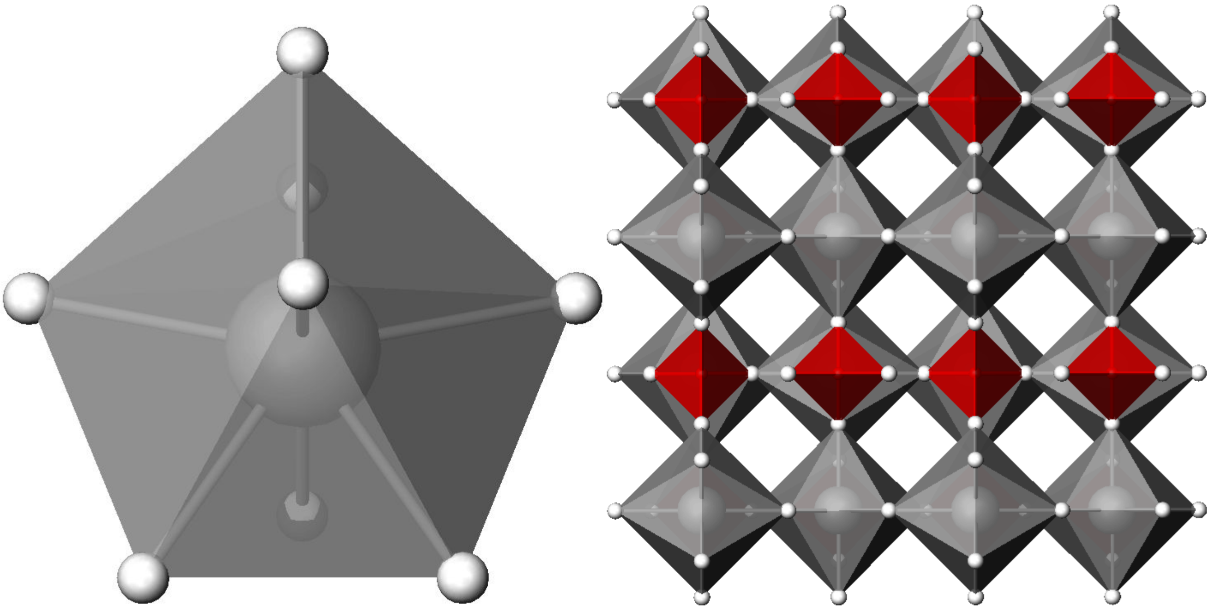

FIGURE 1.10: *Details of the Zr coordination and a view along the c-axis of zircon based on un-doped synthetic zircon (Finch et al. 2001).*

The luminescence of both natural and synthetic zircons has been investigated by a number of methods including PL (Nicholas 1967; Shinno 1987; Shinno & Sugihara 1989; Gaft 1992; Gorobets & Rogojine 2002; Gaft *et al.* 2005), laser induced time-resolved PL (Gaft *et al.* 1998, 2000a,b, 2001, 2002), CL (Yang *et al.* 1992), RL (Kirsh & Townsend 1987; Karali *et al.* 2000) and IL (Finch *et al.* 2004). The two main types of luminescence centres in zircons, which usually result in blue, green or yellow luminescence, relate to REE^{3+} or defects. Natural zircons often have a broad yellow luminescent band between 560 and 600 nm and the broad shape is consistent with a defect. The type of defect causing the emission is still a topic of great debate in the literature. However, most studies agree that the emission is related to defects generated by structural radiation damage caused by the decay of U and Th incorporated into the structure.

Understanding fully the luminescence of natural zircons, especially the controversy of the yellow emission band, is a topic beyond the scope of the present study. Therefore, this study only focuses on REE-based luminescence of zircon. John Hanchar kindly made a series of synthetic REE^{3+} doped zircons available for this study. For details on the synthesis, crystal structure and chemical composition see Hanchar *et al.* (2001) and Finch *et al.* (2001). The RL and TL luminescence properties of these samples have been described by Karali *et al.* (2000) and IL luminescence on a selection of samples by Finch *et al.* (2004). The luminescence data already available for these samples makes them ideal for comparing the effect of different methods of excitation on the resulting luminescence.

Chapter 2

Methodology and Synthesis

Methodology and Synthesis

2.1 Luminescence Spectroscopy

2.1.1 Photoluminescence (PL)

The system is a fluorolog 2, with a peltier-cooled red-sensitive Hamamatsu 928R photo multiplier tube (PMT). The instrument has been customized at the School of Geography & Geosciences, University of St Andrews, to be used for geological and synthetic solid materials rather than solutions, *e.g.* the original sample stage has been replaced with a xyz-stage from an electron microscope. Several parts of the system were replaced and upgraded by Jobin-Yvon in 2000, including installation of new software and controllers. In the course of my PhD several other modifications have been made to the instrument, including the addition of a movable diaphragm iris and housing for filters (1 and 6 on Figure 2.1). In addition to the instrument changes, LabVIEW software has been developed in-house to run the instrument and perform data correction. A schematic drawing of the instrument is given in Figure 2.1. The benefits of the different modifications are given below.

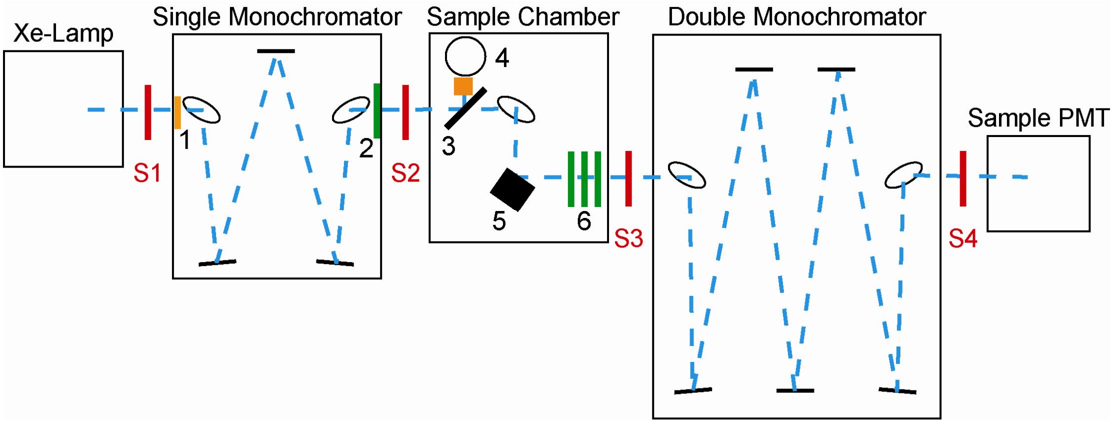

FIGURE 2.1: *Schematic drawing of the PL system. The blue line indicates the beam path. The oval shapes and black lines changing the beam path are mirrors and the diffraction gratings, respectively. S1 to S4 are adjustable slits, 1) Diaphragm, 2) Band-pass filter, 3) Beam splitter, 4) Reference PMT with a cuvette containing rhodamine-B in front of it, 5) Sample, 6) Holder for the secondary filters.*

2.1.1.1 Light Source

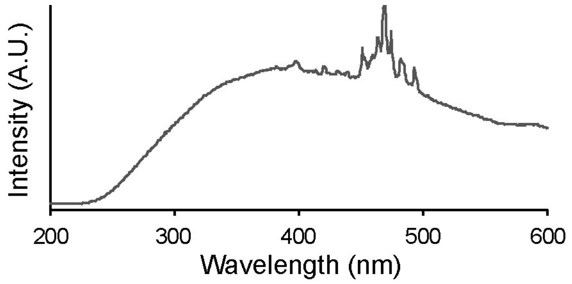

FIGURE 2.2: *Emission spectrum of the Xe-lamp showing the change in intensity with wavelength. Also, note the series of line emissions between 400 and 500 nm.*

A Xe-lamp with a wavelength range of ~240 to 600 nm is the excitation source. Figure 2 shows the emission profile of the lamp and a significant intensity dependence of the wavelength is observed. In order to correct for this effect a reference PMT is placed between the excitation monochromator and the sample. A cuvette containing rhodamine-B dissolved in 1,2-propanediol (99%) is placed in front of the reference PMT, which records the luminescence of the rhodamine-B. The signal recorded from the reference PMT is used to correct the data for the change in intensity as a function of wavelength of the Xe-lamp (Fig. 2.2).

2.1.1.2 Monochromators

Excitation

Scattering of the primary light source is a problem in single monochromators and it was found that the primary beam was reflected from the sample surface into the emission monochromator. For this study of REE luminescence it is further problematic as the line emissions of the Xe-lamp (Fig. 2.2) closely correspond to emissions expected to originate from Dy^{3+}. Therefore, the excitation monochromator was modified in this work to eliminate the scattering. Black paper partitions were added to isolate the individual light paths, and an iris diaphragm was fitted to avoid light from the lamp being scattered from the frame of the first focusing mirror.

A band-pass filter was placed at several different positions within the excitation monochromator to resolve the problem (see Section 2.1.1.3 for a detailed description of the band-pass filter). When the band-pass filter was placed just after the first mirror the Xe lines were still observed in the dataset. However, when it was placed immediately before the exit slits of the monochromator the lines disappeared. This indicates that the origin of the Xe-lines is stray light in the monochromator.

Emission

A Spex 1680 Double Spectrometer is used as monochromator for the emission. A double monochromator design is less prone to problems with stray light. During testing and data collection, no evidence for significant stray light through this monochromator was found.

2.1.1.3 Filters

Band-Pass

Three band-pass filters (Comar 320 GB, 330 GB and 360 GB) were tested to eliminate the problem with the lines of the Xe-lamp in the 400-500 nm region. Tests of the filters show that all the filters are efficiently removing any traces of the Xe line spectra in the 400-500 nm region (Fig. 2.3). GB 360 is not UV transparent and since GB 320 is transparent closer to the visible region than GB 330 is, the GB 320 filter is used in the system.

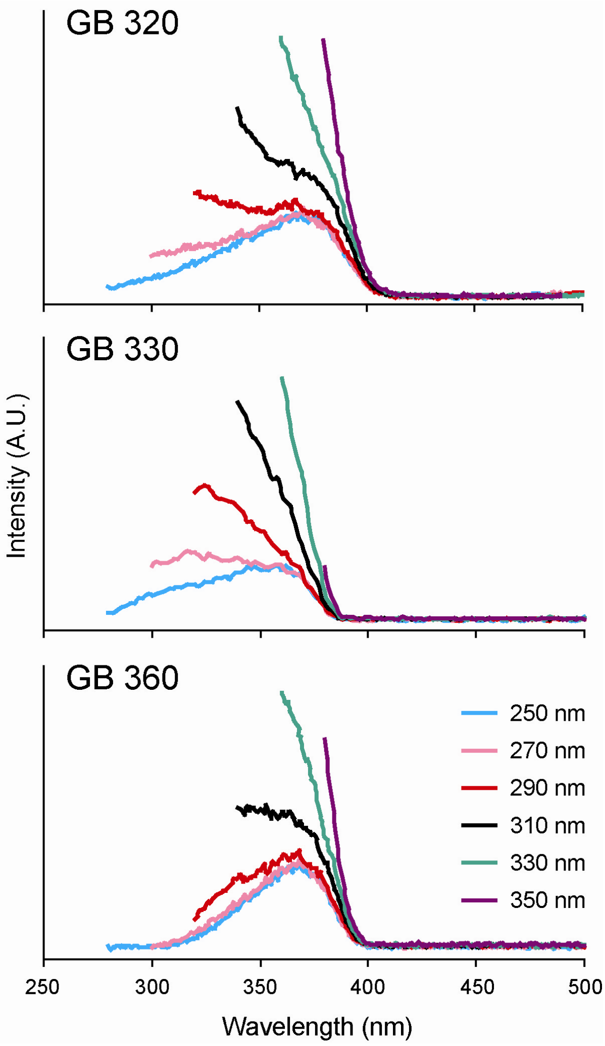

FIGURE 2.3: *Test of the three band-pass filters. The different wavelengths in the figure are different excitations.*

Care must be taken when interpreting emission data in the UV-region when a band-pass filter is used. Some spectra could resemble broad emission bands (Fig. 2.3), but the shape is caused by the increase in intensity of the lamp with increased wavelength combined with the increased absorption by the band-pass filter when getting closer to the cut-off wavelength for the filter. In other words, the peak represents the increase in background until the filter removes the background.

Secondary

A series of Comar long-pass filters were placed between the sample and the emission monochromator. These filters were placed in order to remove doublets of the primary beam, but also in cases where a strong emission was present in the UV region.

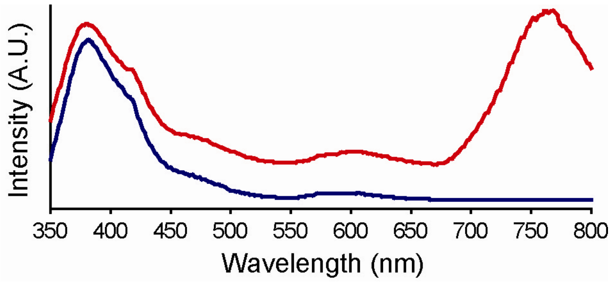

FIGURE 2.4: *Emission spectrum of Leuco8 under 290 nm excitation. Each spectrum consists of two part spectra, which are matched to give a whole spectrum. The red spectrum only has a 315 nm filter to remove reflection of the primary beam. The blue spectrum has an additional 495 nm filter to remove the doublet of the strong UV-Blue emission.*

Figure 2.4 shows the emission spectrum of Leuco8 under 290 nm excitation and the red spectrum shows the typical UV-Blue emission, but also a broad emission in the red to near-IR. This emission could be interpreted as Fe^{3+} luminescence. However, when a 495 nm filter is placed after the sample the broad emission in the red part of the spectrum disappears, revealing it is a doublet of the strong UV-Blue emission. For the majority of data collections, long-pass filters were used routinely.

2.1.1.4 System Response

Due to the combination of filters used during data collections, the filters were not characterised individually, but a whole dataset was collected by reflecting the primary beam off the brass sample holder. A Hg-lamp was used to calibrate the wavelength of the emission monochromator, which was then subsequently used to calibrate the excitation monochromator.

2.1.1.5 Errors and Resolution

Although secondary filters were used to remove doublets of the primary beam and UV emissions, instrument artefacts are still unavoidable. Figure 2.5 shows the excitation spectrum of the 563.5 nm Sm^{3+} emission in sample GAR together with a spectrum recorded at 565.5 nm. The spectrum consists of one broad and several line excitation bands. The majority of peaks are overlapping, but magnifying the scale (Fig. 2.5A) reveals some peaks have shifted. The first of these is ~282 nm and is at half the wavelength of the emission band monitored. The second peak is ~334 nm and this is at ~60% of the monitored emission band. Both bands are related to diffraction of the primary beam in the gratings in the monochromators. To ensure observed peaks were real and not artefacts, an additional data set with a slightly different excitation wavelength (for emission scans) or emission position (for excitation scans) was always acquired. The peaks showing a shift between the two were identified and removed from the data presented.

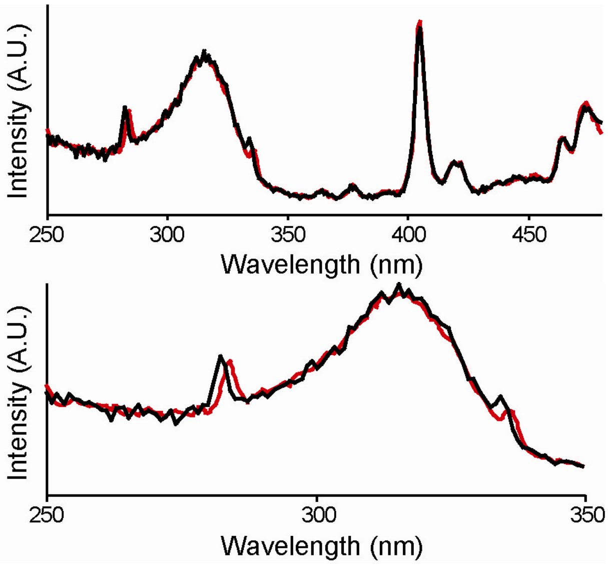

FIGURE 2.5: *The excitation spectrum of the 563.5 nm emission of GAR (black) and a spectrum recorded at 565.5 nm (red).* ***5A*** *(top) shows the two overlapping spectra, however, the detailed picture below (****5B****) shows that two of the peaks do not overlap indicating they are instrument artefacts.*

The wavelength resolution of the instrument is dependent on three main factors i) the intensity of the signal ii) the step-size used and iii) the slit-size used. When the luminescence signal is low, a decrease in the signal to background ratio reduces the resolution, but no constant correction can be given for this effect.

To asses the influence of step- and slit size on the instrument resolution, a series of tests were carried out examining the 480 nm series of Dy^{3+} emission in a zircon. To ensure similar conditions all data were collected without changing sample position or the first slits (S1 and S2 in Fig. 2.1).

Figure 2.6A shows the influence that the step-size has on the spectrum and hence resolution. When a step-size of 0.2 nm is used at least seven peaks can be distinguished, but with a step-size of 5 nm the entire series of line emissions merge into one broad emission. The same effect is seen in Fig. 2.6B, where the step-size is kept at 0.2 nm, but the slits after the sample (S3 and S4 in Fig. 2.1) are changed. The best resolution possible with a strongly luminescent material will be less than one nm.

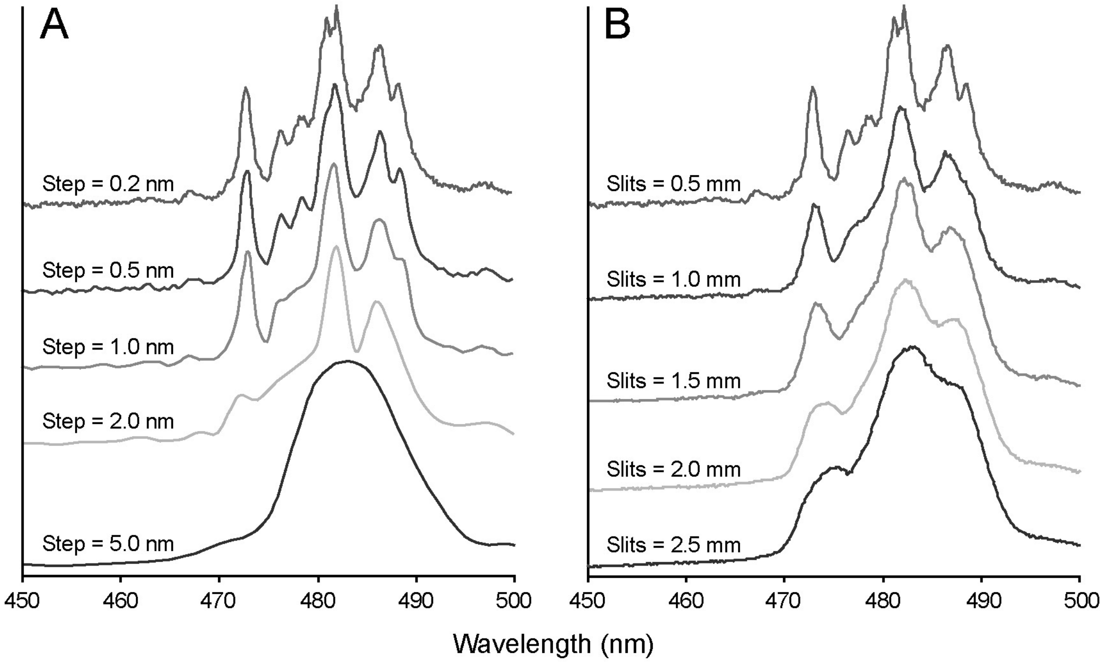

FIGURE 2.6: *The 480 nm Dy^{3+} emissions in a natural zircon at 350 nm excitation. A) shows the effect of increasing step size on the wavelength resolution, in all cases slits 3 and 4 are 0.5 mm. B) shows the effect of the change in slit size of S3 and S4 on the resolution, when the step size is 0.2 nm.*

2.1.2 Cathodo- and Radioluminescence (CL and RL)

The instrument used is a high-sensitive multiplex system developed at the University of Sussex. The instrument has f2/2 optics and the detectors are two imagine photomultiplier tubes that simultaneously collect two spectra centred in the UV and visible region, respectively. These are subsequently matched to give the full coverage range of 200 – 800 nm with ~4 nm resolution, after typical measurement times of 30 to 60 seconds. The two excitation sources are an electron gun and a Philips Cu X-ray tube. The instrument has a heating and cooling stage enabling data collection in the temperature range ~40 to 700 K. For a full description and later modifications of the instrument see Luff & Townsend (1993) and Wang (2007). During the project the instrument was moved from the University of Sussex to the School of Geography & Geosciences in St Andrews. In connection with the move damage occurred on different components of the instrument. For this reason the data collected on meliphanite is only with CL, room temperature and using the visible detector reducing the wavelength region to ~400 - 800 nm.

2.1.3 Ionoluminescence (IL)

A 3 MeV van de Graaf accelerator at the University of Sussex was used to generate high energy (H^+, H_2 or $^4He^+$) ion beams with acceleration potentials between 0.50 and 2.5 MeV, currents between 30 to 200 nA and a spot size of ~0.5 cm^2. The interaction of the ion beam with solids can be modelled using software like SRIM (Ziegler & Biersack 2003). By using low currents and voltage and H^+ ion beams, the damage caused by the ion implantation is minimised. Conversly, when heavier ions are chosen and the current increased, damage of the structure makes it possible to investigate the effect of defects on the luminescence. Furthermore, a combination of heavier ions and a change in the acceleration potential changes the penetration depth of the ions and hence the depth where the luminescence signal originates from, as the majority of the ionisation occurs at the end of the ion track.

Fresh cleavage fragments or powders glued onto an Al-foil were placed so that the incident beam strikes at an angle of ~22.5°. The light emission was collected by a quartz fibre optics, placed ~45° from the incident beam, and connected to an f/4 Spectrapro 300i monochromator. A Photek image intensified CCD camera was used as a detector in the wavelength range from 200 to 1100 nm with a 2 nm resolution. The program WinSpec32 was used to match two spectra and generate a continuous spectrum covering a wavelength range of 200 – 1100 nm. The instrument has different gratings and when a large spectral range was investigated a lower grating was used, while a 1200 lines/mm grating was used when detailed spectra with better resolution were acquired. In such cases, the whole spectrum was recorded without gluing several part-spectra together. This approach also eliminates the problem associated with fluctuation of the current of the ion beam, which can cause poor matching of the two part spectra. As the current cannot be monitored simultaneously with the data collection, there is no way of knowing if the dose-rate is the same in the two part spectra, *i.e.* care must be taken when comparing intensity changes between emission bands in the blue and the red region of a glued spectrum.

Most spectra were acquired at room temperature although an 8 W He compressor was used to record spectra in the temperature range down to ~40 K with a temperature resolution ~10 K. In cases where detailed temperature mapping was not required, a hollow sample holder filled with liquid nitrogen was used to reach a temperature ~77 K. The temperature resolution of these experiments is not constrained due to poor thermal conductivity. All experiments were conducted in a vacuum of ~10^{-6} mbar. A linear normalisation was used to correct the intensity data for variations in beam current, which was checked immediately before and after each acquisition. The intensity data were corrected for the system response using a W lamp and W emissivity data from Lide (1994).

2.2 Chemical Characterisation

2.2.1 Electron Probe Micro Analyses (EPMA)

Crystal fragments were imbedded in an epoxy mount prior to chemical analyses. Only sample GAR was made as two thick sections orientated parallel and perpendicular to the *c*-axis, respectively. The samples were carbon coated before the major element composition was analysed using a CAMECA SX100 at the Natural History Museum in London. The analyses were carried out in WDS-mode and a series of natural and synthetic standards were used (see Table 2.1). Some elements were analysed in different standards in order to minimise the matrix effect between standard and sample. An example is Ca where an apatite standard was used when analysing apatites but wollastonite when analysing meliphanite. The current was 20 nA and the acceleration voltage 15 kV, and depending on the mineral being analysed the

TABLE 2.1. *List of standards used for EPMA analyses*

Standard	Elements
Apatite	Ca, F, P
Celestine	S, Sr
Halite	Cl
Jadeite	Al, Na
Olivine	Fe, Mg
Sphalerite	Zn
Topaz	F
Uraninite	U
Wollastonite	Ca, Si
Zircon	Zr
KBr	K
$MnTiO_3$	Mn, Ti
$ScPO_4$	P
Pure Metal	Hf, Nb, Ta, Th
Synthetic Glasses	Ce, La, Nd, Y

beam was defocused to avoid damage of the sample and migration of Na and F. Mobile elements like Na and F were analysed first to further minimise migration and measurement times were between 10 and 60 seconds depending on element. Intensity data were corrected for inter-element overlaps, and for matrix effects using a Cameca version of the PAP PhiRhoZ programme (Pouchou & Pichoir 1984). In the case of Be-bearing minerals, the content of Be was not determined directly, but set to give an integer in the subsequent formula calculation. This is possible as Be rarely disorders with Si, despite of having similar sizes in a tetrahedral coordination, 0.27 and 0.26 Å, respectively (Shannon 1976; Hawthorne & Huminicki 2002).

2.2.2 Laser Ablation Inductively Coupled Plasma Mass Spectrometry (LA-ICPMS)

A variety of trace elements were determined by LA-ICPMS at the Natural History Museum in London using an Agilent 7500*cs* ICPMS coupled to a New Wave Research UP-213 A1 (213 nm laser with a power density of 3.5 J/cm^2 for a 60 µm spot). The spot size was adjusted to the trace element concentration to avoid overload of the detector. NIST 612 was used as the primary standard for machine fluctuation correction and Ca (for apatite and meliphanite) and Si for zircon, determined by EPMA, were used as internal standards. The analyses were carried out on the epoxy mounts after EPMA analyses.

2.2.3 X-ray Fluorescence Spectroscopy (XRF)

The purity of the reagents used for the synthesis was investigated using a Spextro X-Lab in the School of Geography & Geosciences in St Andrews. The instrument has a rhodium anode and Si detector and depending on the element analysed for a series of targets. The reagents were mixed with binder and pressed into pellets using a 13 mm die. The pellets delaminated and due to the costs of the reagents, no further attempts were made on making pellets. An alternative approach of placing a thin layer of reagent on a high purity 4 µm polypropylene film (Prolene) inside a plastic beaker did, however, prove successful.

2.2.4 Fourier Transformed Infrared Spectroscopy (FTIR)

After EPMA and LA-ICPMS analyses, the top layer of the epoxy blocks were repolished to remove the coating and any ablation residues. A Philips PU9800 FTIR spectrophotometer was used to collect reflective IR spectra in the range from 700 to 4000 wave numbers (cm^{-1}) to investigate the presence of H_2O, OH or CO_3. The instrument is located at the National History Museum in London and has a detection limit of approximately 1 Wt% for the relevant molecules. The relatively high detection limits for this experimental set-up make contributions from molecules in the air negligible.

2.3 Imaging

2.3.1 Scanning Electron Microscopy (SEM)

Images of the synthesised products were acquired using a JEOL JSM-5410 Scanning Microscope at the School of Geography & Geosciences in St Andrews. The grain size resolution is approximately 0.5 µm. The samples were carbon or gold coated to avoid charging.

2.3.2 Cathodoluminescence

A Technocyn 8200 Mk 3 Cathodoluminoscope fitted onto a Nikon Optiphot petrographic microscope at the School of Geography & Geosciences in St Andrews was used to investigate the heterogeneity of both natural and synthetic samples. The acceleration voltage was typically 14 kV, with a beam current of 600 µA at a spot size of ~1 cm^2, which gives a power density of < 100 kW/m^2. Images were collected with a DVC camera using XCAP 3.0 software and typical exposure times ~10 s.

2.3.3 Photomicrograph

An Infinity X camera from Deltapix attached to a Leitz LABORLUX 12 POL S petrographic microscope was used to acquire images of thick sections with the Delta View software (www.deltapix.com).

2.4 Crystallography

2.4.1 Single-crystal

2.4.1.1 Data Collection and Refinement

Single-crystal x-ray diffraction data were collected at room temperature for 11 natural apatites using a Bruker-AXS 4-circle diffractometer with a CCD detector, sealed Mo tube and graphite monochromator, at the Department of Geography and Geology, University of Copenhagen. For crystal orientation and data collection, the program SMART was used. The integrated intensities of Bragg reflections were obtained with the program SAINT+. An empirical absorption correction, based on an ellipsoidal approximation to the shape of the crystal fragments and idealised chemical formula was performed using XPREP. All programs are products of Bruker-AXS.

A Nonius Fr591 diffractometer with KappaCCD equipped with a Mo-tube operated at 90 kV and 60 nA, placed at the Department of Chemistry, University of Southampton, was used to collect single-crystal intensity data of some selected meliphanite samples. A continuous N_2 gas-flow ensured the data were collected at ~120 K. The instrument has focussing mirrors, making it possible to analyse small grains. However, the combination of a small grain size and the instrument primarily being used for organic compounds resulted in a lack of absorption correction of the data.

The initial structural model was in each case obtained from an inspection of the results of direct methods (SHELXS-97, Sheldrick 1997a) and then refined with SHELXL-97 (Sheldrick 1997b). Scattering factors for neutral atoms were used. The first cycles of least square structure refinement were made with isotropic individual atomic displacement parameters. In the subsequent refinements, the atomic displacement factors were made anisotropic and the occupancies of Ca and P were set free. The weighting scheme for the squares of structure factors was adjusted to give the best value for the goodness of fit (Goof) parameter and, where applicable, the coefficient of the secondary extinction was also refined.

2.4.1.2 Coordination Analysis

After the refinements were concluded to satisfaction, an analysis of the coordination polyhedra based on the centroid approach (Balić-Žunić & Makovicky 1996; Makovicky & Balić-Žunić 1998) was performed using the program IVTON (Balić-Žunić & Vicković 1996). The parameters calculated were Polyhedron Volume, Polyhedron Distortion, Eccentricity (the deviation of the central atom from the centroid of the polyhedron) and Asphericity (deviations of the bonding anions from a common sphere).

2.4.2 Powder

2.4.2.1 X-Rays

X-ray powder diffraction analyses were primarily conducted on a Philips 1050 with monochromated CoKα-radiation at the School of Geography and Geoscience in St Andrews. For determining unit cell parameters, the program SIROQUANT was used (www.sietronics.com.au).

A Philips PW3710 at the Department of Geography and Geology in Copenhagen with monochromated CuKα-radiation was used to collect detailed data on selected synthetic apatites for Rietveld analysis using the program TOPAS (Bruker-AXS).

2.4.2.2 Neutrons

Neutron diffraction data was collected at 120 K on the D20 instrument at the ILL in Grenoble. D20 is a high flux instrument making it possible to investigate smaller samples compared to more conventional neutron instruments. The benefit of neutron compared to x-ray analysis is that x-ray diffraction is based on scattering by the electrons, which makes accurate determination of heavy atom positions easy but lighter atoms like H and Be have larger errors. However, both H and Be scatter neutrons effectively, and hence better positions for these lighter elements can be obtained with neutrons. With the sensitivity of neutrons to Be it is possible to investigate small degrees of disorder between Be and other elements in tetrahedral coordination. The samples were ground to a fine powder and placed in a vanadium sample holder. The wavelength used was 1.86780 Å and the image plate covers a 2θ range of more than 150 degrees. A detailed description of the instrument can be found in Hansen *et al.* (2008). Rietveld refinement of the powder data was performed using GSAS with the EXPGUI interface (Larson & Von Dreele 2000; Toby 2001).

2.5 Solid State Diffusion Synthesis

Solid state synthesis is a method whereby known amounts of reagents are ground intimately and then fired as solids at elevated temperatures to initiate reaction and to produce a single-phase solid. The high temperature also increases the diffusion of ions in most solids (Atkins *et al.* 2006). This method is preferred to other types of syntheses (*e.g.* using fluxes) since the presence of the flux can in some cases contaminate the product and/or cause partition of key elements between the target structure and interstitial remnants of flux. A number of different methods will be described, which were investigated to generate homogeneous ceramics and single-crystals with predicted compositions. The term “ceramic” is used in the following section to describe microcrystalline aggregates of products (usually <2 µm) with no distinct crystal faces contrary to “single-crystals” which is describing crystals with clear crystal faces and with sizes between 50-170 µm.

It was initially intended to compare the structural influence on the luminescence properties of REE in slightly different structures by synthesising a limited number of samples with the same dopant levels of both a fluor and chlorapatite. In apatite the monovalent cations are found in channels running parallel to the *c*-axis. *F* is situated in the middle of a triangular coordination of *Ca2* contrary to chlorapatite where *Cl* is situated in-between the two *Ca2* triangles (Hughes & Rakovan 2002).

2.5.1 Apatite

The incorporation of REE for Ca in apatite results in an increased positive charge that needs to be balanced to produce stable, single-phase apatite structures. Equations 2.1 and 2.2 are the two main mechanisms for charge compensation, based on chemical data of natural REE-rich apatites (Rønsbo 1989).

$$REE^{3+} + Si^{4+} \leftrightarrow Ca^{2+} + P^{5+} \qquad [2.1]$$

$$REE^{3+} + Na^{1+} \leftrightarrow 2Ca^{2+} \qquad [2.2]$$

To simplify the synthesis in the present study, only Na was used for charge balance, *i.e.* charge balance in accordance with Eq. 2.2. This substitution is similar to that found in belovite and kuannersuite (see Section 1.3.1).

2.5.1.1 Reagents

The phase purity of the reagents was confirmed using XRD and XRF prior to synthesis. XRF revealed only minor (<100 ppm) contamination of a few reagents (contaminant): $CaCO_3$ (Sr, Ba, Cu), CaF_2 (Sr, Ba, Y, Zr), $NH_4H_2PO_4$ (Ca, Si), $Na_2CO_3 \bullet 10H_2O$ (Cu, Y) and Er_2O_3 (Y). To ensure the $CaCO_3$, CaF_2 and REE_2O_3 reagents were water free they were dried overnight at 550°C. As these powders rapidly adsorb water from the air, they were kept in the furnace between weighing out the individual samples. $NH_4H_2PO_4$ and $Na_2CO_3 \bullet 10H_2O$ have low thermal stability and for that reason they were not dried prior to use but neither is believed to be significantly hydroscopic, *i.e.* no instabilities were observed during weighing of these reagents. Table 2.2 gives a list of reagents used, purity and manufacturer. The reagents were weighed to 0.0001 g and ground in an agate mortar. A Carbolite tube furnace (STF 16/50/450) equipped with a programmable Eurotherm 3216 temperature controller was used in all methods.

TABLE 2.2. *Reagents used in this study*

Reagent	Purity (%)	Manufacturer	Reagent	Purity (%)	Manufacturer
$CaCO_3$	99.5	Alfa Aesar	La_2O_3	99.99	Johnson Matthew
$CaCO_3^{\#}$	>99	Aldrich	Nd_2O_3	99.99	NHM***
$MnCO_3$	99.985	Alfa Aesar	Sm_2O_3	99.99	Interachem Inc.
$SrCO_3$	>98.5	BDH	Eu_2O_3	99.9	Interachem Inc.
CaF_2	99	Acros	Gd_2O_3	99.99	NHM
NaF	99	Alfa Aesar	Dy_2O_3	99.9	Interachem Inc.
$NaF^{\#}$	TG*	BDH	Ho_2O_3	99.99	Interachem Inc.
$CaCl_2$	GPG**	Fisher Scientific	Er_2O_3	99.95	Interachem Inc.
$BeO^{\#}$	99.98	Aldrich	Tm_2O_3	99.99	Interachem Inc.
$Na_2CO_3{\bullet}10H_2O$	>99.0	VWR	Yb_2O_3	99.99	NHM
$NH_4H_2PO_4$	98.0	Alfa Aesar	$SiO_2^{\#}$	>99.995	Aldrich
$Pr_2(CO_3)_3{\bullet}8H_2O$	99.99	Alfa Aesar			

 # Reagents used in Southampton.
** Technical Grade – No purity percentage are given.*
*** General Purpose Grade – No purity percentage are given.*
**** Natural History Museum; Unknown manufacturer.*

The compositions of the synthetic fluorapatites are in the solid-solution series between the two end-members, $Ca_5(PO_4)_3F$ and $Ca_3NaREE(PO_4)_3F$. The reactions used to synthesis these end-members are:

$$6NH_4H_2PO_4 + 9CaCO_3 + CaF_2 \rightarrow 2Ca_5(PO_4)_3F + 9CO_2 + 6NH_3 + 9H_2O \quad [2.3]$$

and

$$\begin{gathered}6NH_4H_2PO_4 + 5CaCO_3 + CaF_2 + Na_2CO_3{\bullet}10H_2O + REE_2O_3 \rightarrow \\ 2Ca_3NaREE(PO_4)_3F + 6CO_2 + 6NH_3 + 19H_2O\end{gathered} \quad [2.4]$$

2.5.1.2 Ceramic Synthesis

The finely ground reagents were transferred to a 13 mm die and 2 tonne pressure was applied to create a pellet. The pellets were placed on Pt-foil in a feldspar boat, which can hold up to five pellets (Fig. 2.7). The boat becomes brittle after just a few heating cycles so to avoid it breaking during placement or removal from the furnace, and hence possible sample contamination, the boat was placed inside an open silica tube.

FIGURE 2.7: *Heterogeneous pellets of Mn doped fluorapatite (Mn content increases from left to right) after firing on Pt-foil in the feldspar boat inside a cut silica tube.*

The samples were preheated for three hours at 500°C before they were re-ground and re-pressed before being returned to the furnace at 1000°C for 12 hours. The samples were removed from the furnace, reground and re-pressed before firing for a further 12 hours at 1000°C. Figure 2.8 provides a schematic representation of the different parts of the synthesis.

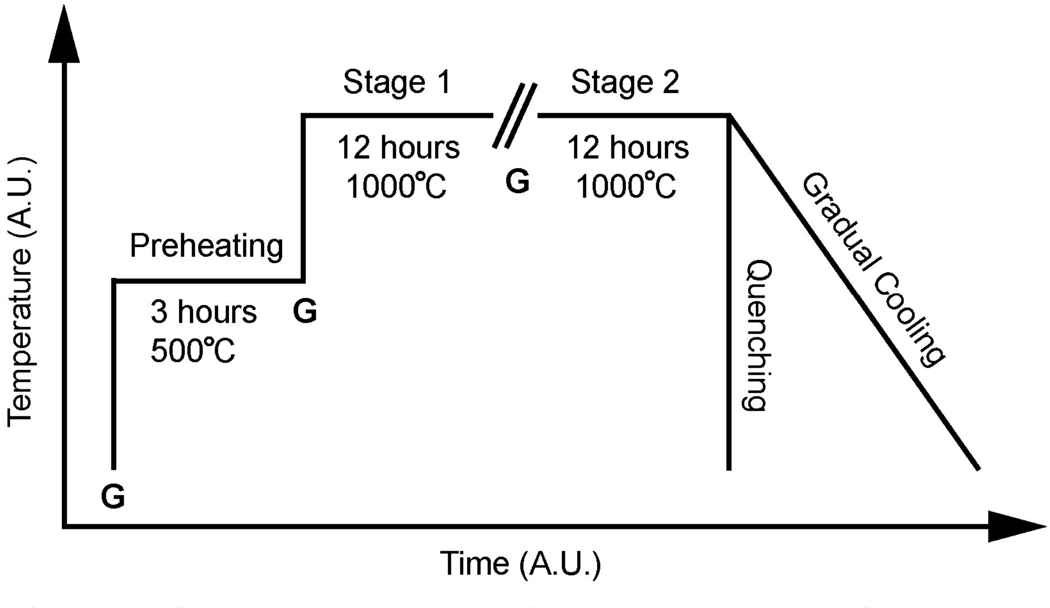

FIGURE 2.8: *Schematic overview of the different parts of synthesis. "G" represents a time when the samples were quenched, ground and pressed into pellets before being returned to the furnace at the correct temperature. Note that the "Gradual Cooling" only applies for the single-crystal growth experiments.*

To verify phase purity of the products (*i.e.* making sure that only the desired phase was formed and that no reagents were remaining) the samples were analysed by powder XRD after each grinding. These tests showed no significant difference in the XRD whether the samples had been left for 12 or 24 hours at 1000°C. However, to ensure chemical homogeneity Stage 2 was always performed. This method is the one used for all the synthetic ceramics in thesis.

The above procedure was developed during the early stages of the project and several aspects of the procedure were found to be critical to the formation of single-phase products. For example, if the temperature is too low during the initial preheating (<500°C) or if the preheating time is extended, CaO (lime) will form. Lime has a high thermal stability (melting point ~2570°C) and is therefore still present as a run product after heating at 1000°C. CaO is also produced if the Stage1+2 temperatures are <800°C. However, phase pure apatite forms at Stage1+2 temperatures from 900°C upwards. Diffusion rates increase with temperature so to increase homogeneity one synthesis was performed with Stage1+2 temperatures 1100°C. However, SEM of this material showed that the aggregates were significantly smaller than 1 μm compared to syntheses at 1000°C, for which aggregates typically were 1-2 μm. If the size of formed products start approaching nanocrystal sizes the increased surface to volume ratio can drastically change the physical properties of a material (Alivisatos 1996). Tanaka & Masumoto (2000) and Suyver *et al.* (2001, 2003) found that the luminescence properties of ZnS:Mn^{2+} nanocrystals differ significantly compared to luminescence of bulk material, which was ascribed to the change in band-gap energy with change in particle size. In order to minimise the probability of forming nanocrystals, and hence products that may display special luminescence not comparable with luminescence of natural fluorapatites, the synthesis were performed at 1000°C. The abbreviations and ideal composition of all synthesised ceramic phases are given in Table 2.3.

TABLE 2.3. *Names and ideal composition of ceramic products*

Name	Formula	Name	Formula
FAPSm1	$Ca_{4.9}Na_{0.05}Sm_{0.05}(PO_4)_3F$	FAPEr3	$Ca_{4.7}Na_{0.15}Er_{0.15}(PO_4)_3F$
FAPSm3	$Ca_{4.7}Na_{0.15}Sm_{0.15}(PO_4)_3F$	FAPEr5	$Ca_{4.5}Na_{0.25}Er_{0.25}(PO_4)_3F$
FAPSm5	$Ca_{4.5}Na_{0.25}Sm_{0.25}(PO_4)_3F$	FAPEr10	$Ca_{4.0}Na_{0.50}Er_{0.50}(PO_4)_3F$
FAPSm10	$Ca_{4.0}Na_{0.50}Sm_{0.50}(PO_4)_3F$	FAPEr15	$Ca_{3.5}Na_{0.75}Er_{0.75}(PO_4)_3F$
FAPSm15	$Ca_{3.5}Na_{0.75}Sm_{0.75}(PO_4)_3F$	FAPEr20	$Ca_3NaEr(PO_4)_3F$
FAPSm20	$Ca_3NaSm(PO_4)_3F$	FAPTm3	$Ca_{4.7}Na_{0.15}Tm_{0.15}(PO_4)_3F$
FAPEu3	$Ca_{4.7}Na_{0.15}Eu_{0.15}(PO_4)_3F$	FAPTm5	$Ca_{4.5}Na_{0.25}Tm_{0.25}(PO_4)_3F$
FAPEu5	$Ca_{4.5}Na_{0.25}Eu_{0.25}(PO_4)_3F$	FAPTm10	$Ca_{4.0}Na_{0.50}Tm_{0.50}(PO_4)_3F$
FAPEu10	$Ca_{4.0}Na_{0.50}Eu_{0.50}(PO_4)_3F$	FAPTm15	$Ca_{3.5}Na_{0.75}Tm_{0.75}(PO_4)_3F$
FAPEu15	$Ca_{3.5}Na_{0.75}Eu_{0.75}(PO_4)_3F$	FAPTm20	$Ca_3NaTm(PO_4)_3F$
FAPEu20	$Ca_3NaEu(PO_4)_3F$	FAPLa20	$Ca_3NaLa(PO_4)_3F$
FAPDy1	$Ca_{4.9}Na_{0.05}Dy_{0.05}(PO_4)_3F$	FAPGd20	$Ca_3NaGd(PO_4)_3F$
FAPDy3	$Ca_{4.7}Na_{0.15}Dy_{0.15}(PO_4)_3F$	FAPYb20	$Ca_3NaYb(PO_4)_3F$
FAPDy5	$Ca_{4.5}Na_{0.25}Dy_{0.25}(PO_4)_3F$	FAPSm0.1Dy0.05	$Ca_{4.7}Na_{0.15}Sm_{0.10}Dy_{0.05}(PO_4)_3F$
FAPDy10	$Ca_{4.0}Na_{0.50}Dy_{0.50}(PO_4)_3F$	FAPSm0.1Dy0.1	$Ca_{4.6}Na_{0.20}Sm_{0.10}Dy_{0.10}(PO_4)_3F$
FAPDy15	$Ca_{3.5}Na_{0.75}Dy_{0.75}(PO_4)_3F$	FAPMn1	$Ca_{4.99}Mn_{0.01}(PO_4)_3F$
FAPDy20	$Ca_3NaDy(PO_4)_3F$	FAPMn2	$Ca_{4.98}Mn_{0.02}(PO_4)_3F$
FAPHo3	$Ca_{4.7}Na_{0.15}Ho_{0.15}(PO_4)_3F$	FAPMn3	$Ca_{4.97}Mn_{0.03}(PO_4)_3F$
FAPHo5	$Ca_{4.5}Na_{0.25}Ho_{0.25}(PO_4)_3F$	FAPMn4	$Ca_{4.96}Mn_{0.04}(PO_4)_3F$
FAPHo10	$Ca_{4.0}Na_{0.50}Ho_{0.50}(PO_4)_3F$	FAPMn5	$Ca_{4.95}Mn_{0.05}(PO_4)_3F$
FAPHo15	$Ca_{3.5}Na_{0.75}Ho_{0.75}(PO_4)_3F$	FAP	$Ca_5(PO_4)_3F$
FAPHo20	$Ca_3NaHo(PO_4)_3F$		

2.5.1.3 Unsuccessful Ceramic Syntheses

Fluorapatite:Pr^{3+}

Pr is a well-known activator for luminescence and is used in many phosphors due to its ability to adopt several luminescence colours depending on the host matrix (*e.g.* Savoini *et al.* 1997; Jia *et al.* 2006, 2007; Li *et al.* 2007). However, Pr often has mixed oxidation states making non-stoichiometric oxides (*e.g.* Pr_6O_{11}) and hence is not suitable for the reaction given in Equation 2.4. One synthesis was attempted using $Pr_2(CO_3)_3•8H_2O$, but already after the preheating stage the pellet had expanded more than any synthesis with REE_2O_3 growing over the Pt-foil and came in direct contact with the feldspar boat. This is most likely caused by the additional amount of CO_2 being formed making the reaction more volatile. Furthermore, the pellet was dark coloured indicating some kind of contamination. Due to the strong reaction during the synthesis, the discolouring combined with the fact that Pr^{3+} can oxidise to Pr^{4+} no further attempts were made to synthesis Pr^{3+} containing fluorapatites.

Fluorapatite:Mn^{2+}

Mn is often divalent and readily substitutes for Ca in numerous minerals, including apatite. Mn luminescence, contrary to REE luminescence, is mostly related to phonon activation (Marfunin 1979; Marshall 1988). Attempts were made to synthesise low Mn content fluorapatites and combining luminescence data with electron spin resonance to describe the coordination of the activator with increasing Mn content. Mn^{2+} readily oxidises to Mn^{3+} or even higher valences, and from Fig. 2.7 it is seen that the pellets show a brown colour typical for oxidised Mn. Figure 2.7 also reveals that the pellets are very heterogeneous, as in addition to the brown colour both bluish and white areas can be observed. The blue colour indicates pure fluorapatite as synthesis of fluorapatite without dopant gave bluish pellets whereas the white parts are most likely reagents that have not reacted. Due to the obvious heterogeneity of these syntheses, no further attempts to produce Mn doped fluorapatites were made.

Chlorapatite

During the XRD investigation of $CaCl_2$ it was found to be very hydroscopic. A powder sample of $CaCl_2$ was prepared for XRD analysis, but the sample was not run immediately but placed with other samples in the XRD sample holder. Less than an hour later the samples were ready to be loaded into the XRD, and it was observed that the $CaCl_2$ had expanded out of its sample holder due to water absorption from the air. It was therefore not possible to obtain an x-ray diffraction pattern and check the reagents phase purity. For this reason, no further syntheses to produce chlorapatite were attempted.

2.5.1.4 Single-crystal Syntheses

Five methods were explored to produce visible single-crystals of REE-fluorapatite that might be suitable for single-crystal XRD. Firstly, the same reagents and preheating was used as described above for the ceramics. However, the reagents were not pressed into pellets or ground between firings in order not to destroy any formed crystal. The temperature for Stage 1 (Fig. 2.8) was increased to 1200°C and maintained for one hour before cooling to room temperature at a rate of 10°C/h. This method did not generate single-crystals, but a material similar to the powders. Secondly, a small portion of the material from the experiment described in the beginning of this paragraph was retained and the remainder was ground. The two portions were then mixed, placed in the furnace and subjected to the same heating and cooling as described above. The aim was to generate a size difference between the particles in hope the difference in surface energy would initiate growth of the larger particles by consuming the smaller, known as Ostwald Ripening. However, this was not observed and solid state methods to produce large (>2 μm) crystals were not followed further.

Thirdly, the method described by Toumi *et al.* (2000) for making Sm fluorapatites ($Ca_3SmNa(PO_4)_3F$), using NaF as the source for both F and Na, but added in 10-fold excess to also act as a flux was followed. In this experiment Dy rather than Sm was used. Ionic fluxes are commonly used in solid state synthesis to enhance crystal sizes since the flux melts at relatively low temperatures (*e.g.* 996°C for NaF) and enhances diffusion of elements. Preheating for four hours at 400°C prior to regrinding, followed by firing at 1200°C then held for one hour, and finally cooled with 10°C/h down to room temperature. Despite following the procedure closely no crystals were formed. In fact, the majority of the reagents had disappeared leaving a greenish coloured layer on the top of the Pt-foil and a shiny glaze on the feldspar boat. EDS analyses of the product, the glazed boat and a fresh boat revealed that the product consists of two parts: a dominating Na and Dy oxide and minor amounts of a Na, Ca, Dy phosphate (Fig. 2.9).

By comparing the glazed with the unglazed feldspar boat (Fig. 2.10), it was found that the glaze is predominately Ca compound. However, no evidence of

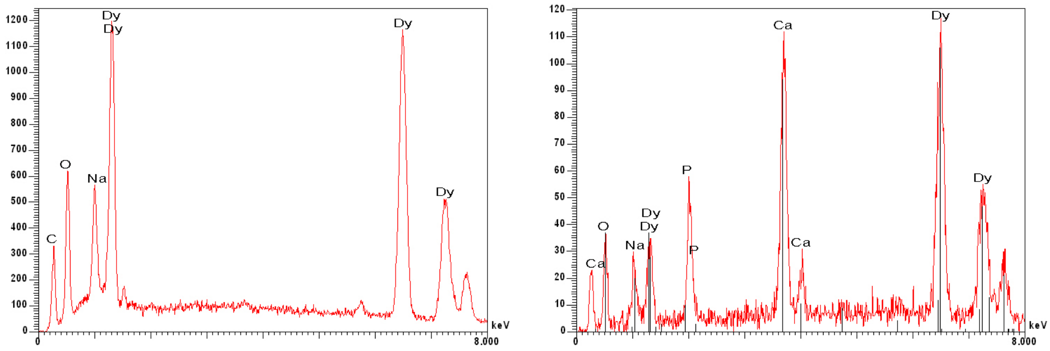

FIGURE 2.9: *EDS of the two different phases remaining on the Pt-foil after the synthesis following the method described by Toumi* et al. *(2000).*

fluorine was found in either the formed compounds (Fig. 2.10) or the glazed boat. The EDS of the glazed boat also revealed the presence of Mg and Fe together with an unidentified peak. The high amount of NaF made the reagent mixture extremely volatile and it seems that fluorine's reaction potential managed to remove Mg and Fe from inside the tube of the furnace and deposit it in the glaze.

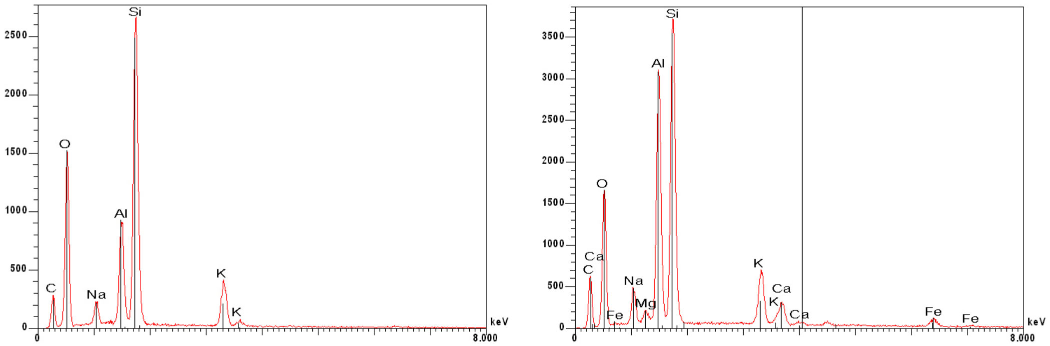

FIGURE 2.10: *EDS of the fresh feldspar boat (left) and the glazed part (right). Note how the glaze contains Ca from the reagents but also Mg and Fe, which most likely have been removed by the formed fluorine gas. The samples used are not polished but just carbon-coated fragments, hence observed changes in relative intensities between the two spectra are most likely caused by absorption effects due to different orientation.*

Fourthly, to estimate the optimum NaF content, a series of batches were made with NaF in 1-, 3- and 5-fold excess. In order to run these under identical conditions the experiments were conducted using small disposable Al_2O_3 crucibles. Pt crucibles would have been preferred, but there was concern that the F-rich flux would attach to Pt and thereby destroy several thousand pounds worth of crucibles in a single experiment. These experiments showed that NaF in 3-fold excess was ideal for generating elongated hexagonal crystals. However, the crucible reacted with the NaF and the other reagents to form several unexpected phases, including euhedral cuboctahedra of SmAl-oxides and also a large amount of elongated hexagonal CaSmNaF-phosphate crystals (Fig. 2.11).

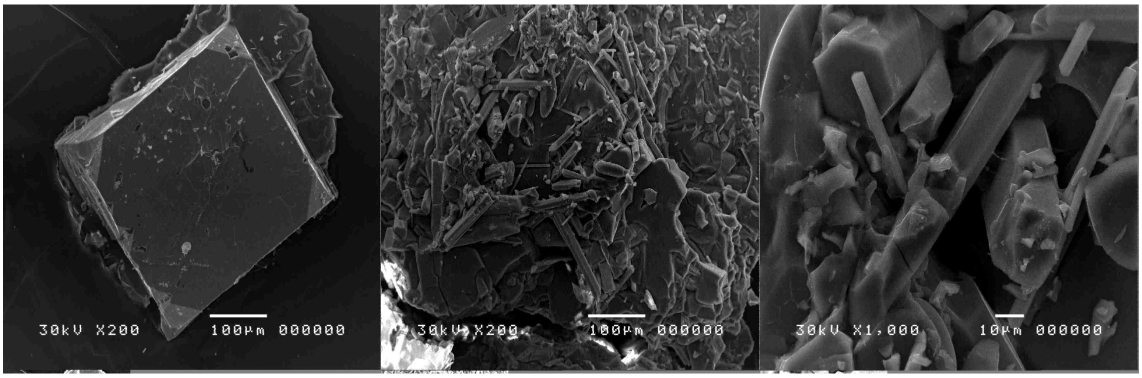

FIGURE 2.11: *SEM image of the formed SmAl-oxide (left) and the hexagonal apatite crystals (middle and right).*

Finally, an experiment was carried out with Sm and NaF in 3-fold excess in a Pt crucible. Figure 2.12 shows the backscatter electron images of the products. It is seen that the individual apatite crystals are unzoned and form mainly under a F-Sm-oxide “lid” with high mean atomic number. The lid seems to inhibit further volatilisation and promote growth of large crystals. Figure 2.12 also reveals a banded pattern, which is caused by oscillations in the Sm, Ca and Na content of the apatite.

FIGURE 2.12: *BEI of the Sm-fluorapatite single-crystal synthesis. The image to the left shows that the crystals formed under a Sm-rich “lid” (white on the picture due to high average Z) and the banded pattern. The image to the right shows that the formed apatite crystals are unzoned. The white colour associated with most crystals is not a high Z phase but a shadow effect as the sample polished poorly and left a high relief, especially around the apatites.*

This method was then applied to generate single-crystals with other REE. These were successful for REE lighter than Sm, but for heavier REE no crystals large enough to see under a binocular microscope (~100 µm) were produced, and hence too small for use in conventional single-crystal XRD. When these samples were turned in the light, reflections were observed indicating that crystals had formed. Although La and Nd-fluorapatite single-crystals were formed, there was a clear decrease in crystal size with lowering of the atomic number from Sm. This observation can be explained by Hughes *et al.* (1991b), who found that Pm and Sm preferentially substitute into the *Ca1* site, whereas lighter REE preferentially substitute into the *Ca2* site. As mentioned in Section 1.3.1 no natural mineral with the ideal end-member composition $Ca_3NaREE(PO_4)_3F$ has been described but two natural equivalents exist where *Ca2* is fully replaced by Sr or Ba, with REE and Na ordering into the *Ca1* site. This suggests that in order to generate a stable ordered fluorapatite end-member like structure, Sm should be the dominating REE (due to its preference for the *Ca1* site) as this gives a cation ordering similar to that found in belovite and kuannersuite. Only a few natural minerals have been described with Sm being the dominant REE, which may explain why a $Ca_3NaREE(PO_4)_3F$ mineral has not been found.

A few experiments were conducted to explore the possibility of increasing the crystal size for the light REE by making belovite ($Sr_3NaREE(PO_4)_3F$). However, these initial attempts did not yield any large crystals and no further attempts were made to explore this system.

2.5.2 Leucophanite

Attempts to synthesise leucophanite were initially been carried out by the Mark T. Weller group at the Department of Chemistry, University of Southampton using the procedure described by Prokofiev *et al.* (1982) with the reaction:

$$2SiO_2 + NaF + CaCO_3 + BeO \rightarrow CaNaBeSi_2O_6F + CO_2 \qquad [2.5]$$

The synthesis was initially attempted at 850°C and with NaF added in surplus as a flux, but all attempts failed to produce phase pure leucophanite.

During a visit to Southampton, attempts were made to synthesise leucophanite. The same reaction was used, but two different batches were prepared, one stoichiometric and one with NaF in 3-fold excess; two samples were made of each batch. As Be is highly toxic, all weighing, grinding and pressing of pellets were conducted in a glove box with nitrogen atmosphere. Contrary to the initial attempts, a preheating stage at 500°C was applied. Table 2.4 shows the heating scheme for the different samples. The final products were analysed by x-ray diffraction. However, for several reasons it was not possible to determine whether leucophanite was the only formed product. Firstly, some diffraction lines corresponded to chkalovite ($Na_2BeSi_2O_6$). Secondly, leucophanite is structurally related to the melilite group, which contains the Be-mineral gugiaite ($Ca_2BeSi_2O_7$). The ordering of Si and Be is different in the two mineral species and although gugiaite is tetragonal (Kimata & Ohashi 1982; Yang *et al.* 2001) and leucophanite orthorhombic but pseudotetragonal (Cannillo *et al.* 1967; Grice and Hawthorne 1989, 2002; Friis *et al.* 2007a) they have similar lengths of the *a* axes. This strong structural relationship between the two minerals makes them difficult to distinguish based on XRD, especially since the degree of order in the synthetic material is not known.

TABLE 2.4. *Leucophanite synthesis*

Batch	NaF Content	Stage 1 + 2
Leuco-A	x 1	900°C
Leuco-B	x 1	1000°C
Leuco-C	x 3	900 C
Leuco-D	x 3	1000°C

Beryllium is very toxic. With no access to facilities meeting the Health & Safety requirements for working with Be in St Andrews, no further attempts were made to synthesise leucophanite.

Chapter 3

Photoluminescence of Zircon ($ZrSiO_4$) Doped with REE^{3+} (REE = Pr, Sm, Eu, Gd, Dy, Ho, Er)

Photoluminescence of Zircon ($ZrSiO_4$) Doped with REE^{3+} (REE = Pr, Sm, Eu, Gd, Dy, Ho, Er)

3.1 Abstract

The photoluminescence properties of synthetic zircon, $ZrSiO_4$, doped with REE^{3+} (REE = Pr, Sm, Eu, Gd, Dy, Ho, Er) was investigated using combined excitation and emission spectroscopy. All samples showed luminescence characteristics of intra-ion energy transitions, similar to other lanthanide doped materials. However, differences caused by the different mode of excitation were observed as well as evidence for the lanthanides occurring in more than one structural site. Energy transfer between different lanthanides was observed in some samples with more than one lanthanide present, indicating that zircon is a possible host for luminescent materials with quantum efficiency >100%. Furthermore, emissions that were unassigned in previous studies of these samples could be assigned to specific lanthanides based on excitation spectra.

3.2 Introduction

Zircon, ideally $ZrSiO_4$, is tetragonal ($I4_1/amd$) and REE readily substitute into the eight coordinated *Zr* site, which forms triangular dodecahedron. The structure is relatively open and may also incorporate trace elements at interstitial sites (Finch & Hanchar 2003; and references therein). Zircon is a widespread natural material that is very resilient to mechanical wear and chemical dissolution. For materials purposes, synthetic zircon analogues are of widespread interest as pigment (Ocanã *et al.* 1998; Badenes *et al.* 2002; Kar *et al.* 2004; Niesert *et al.* 2004). The tetrahedral unit of the zircon structure type is easily replaced by either a phosphate or a vanadate group making it possible to synthesis a whole range of luminescent materials (*e.g.* Oomen *et al.* 1986; Riwotzki & Haase 1998). Furthermore, zircon readily incorporates actinides and the structure is particularly resilient to high radiation doses, making it attractive for the long-term storage of nuclear waste (Ewing *et al.* 1995, 2003 and references therein). Many of the properties important in the materials science of zircons rely intrinsically on knowing the position of the element within the structure. Hence, it is extremely important to determine the mechanisms by which elements substitute into zircon. Techniques such as ESR have identified defects connected to the Si tetrahedra or Zr polyhedra (Laruhin *et al.* 2002; Tennant *et al.* 2004, and references therein). Farges & Calas (1991) and Farges (1994) used EXAFS to show that metamictisation decreases the coordination number of Zr from 8 to 7 and NMR has been used on ^{29}Si and ^{17}O to show that an increased polymerisation of the Si tetrahedra occurs with increasing metamictisation (Farnan & Salje 2001; Ashbrook & Farnan 2004; Farnan *et al.* 2004). Less widely used is luminescence although luminescence is a sensitive probe of local coordination in materials and gives clear signals even at ppm levels, far below the detection limits of most other methods. Hence, luminescence can be used as a probe of local coordination in dilute and ultradilute systems.

The present paper presents photoluminescence (PL, *i.e.* luminescence following irradiation by UV or visible light) data from a suite of Rare Earth Element (lanthanide) doped synthetic zircons to understand more fully the role that lanthanides play in the luminescence of the zircon system. By examine the PL as a function of the energy of incident photons it is possible to explore the responses to obtain insights into the hosting of the lanthanides in the structure. This chapter will also examine the responses of samples doped with two lanthanides to understand more fully the energy transfer processes that occur between lanthanides and between lanthanides and the lattice. As well as describing energy transfer processes that may make zircon a suitable material for quantum cutting.

3.3 Previous Research

The luminescence of natural and synthetic zircons has been investigated by a number of methods including photoluminescence (PL, *i.e.* from excitation with UV or light) (Nicholas 1967; Shinno 1987; Shinno & Sugihara 1989; Gaft 1992; Gaft *et al.* 1998, 2000a,b, 2001, 2002; Gorobets & Rogojine 2002; Gaft *et al.* 2005; Lee & Kim 2008), cathodoluminescence (CL, by a beam of electrons) (Yang *et al.* 1992), radioluminescence (RL, from x-rays) (Kirsh & Townsend 1987; Karali *et al.* 2000) and ionoluminescence (IL, from a beam of ions) (Finch *et al.* 2004). Although defects play an important role in the luminescence of natural zircons, one of the most important groups of activators is the lanthanides. Hence, there is significant interest in the manner in which lanthanides activate and modify zircon luminescence. Luminescence from Dy^{3+} is one of the most commonly observed lanthanide emissions in natural zircons suggesting that other lanthanides effectively transfer energy to Dy. The efficient luminescence combined with the strong structural stability makes zircon an interesting luminescent material for potential use under non-ambient conditions.

PL of synthetic zircon has previously been described by Shinno (1987) and Gaft *et al.* (2000a,b). These zircons were grown as single crystals in a Li-Mo flux, and relied on O^- hole centres to charge compensate for REE^{3+} substituting for Zr^{4+}. However, the zircons in the present study are co-doped with P^{5+}, giving a solid solution towards YPO_4 (xenotime) according to the scheme:

$$Zr^{4+} + Si^{4+} = REE^{3+} + P^{5+} \qquad [3.1]$$

This mechanism allows complete solid-solution and is the most widespread in natural zircons. The radio- and thermoluminescence of the samples used in the present study have been described by Karali *et al.* (2000). Finch *et al.* (2004) published IL data on a selection of the samples. In addition, CL spectra of the Dy and Sm doped zircons are reported in Nasdala *et al.* (2003) and PL of the Sm doped zircon in Nasdala *et al.* (2004a).

3.4 Materials and Methods

Single-crystal zircons were grown from a Li-Mo flux with P^{5+} to charge balance for the REE^{3+} substituting for Zr^{4+}. Details on the synthesis and sample characterisation can be found in Hanchar *et al.* (2001) and Finch *et al.* (2001). All samples used in this study are powders. Sample names and dopant levels are presented in Table 3.1.

TABLE 3.1 *Sample labels and REE concentration (ppm) of the investigated samples*

Sample	ZirPr	ZirSm	ZirEu	ZirGd	ZirDy	ZirHo	ZirEr
REE*	2222	7762	18827	36699	69880	80401	98209

** The concentrations in ppm are calculated based on the Wt% REE_2O_3 values, obtained by EPMA, and presented in Table 3 in Hanchar* et al. *(2001).*

Photoluminescence data were collected using a SPEX Fluorolog 2 luminoscope in the School of Geography and Geosciences at the University of St

Andrews. A Xe-lamp with a wavelength range of approximately 240 to 600 nm was used as excitation and specific wavelengths were selected using a monochromator (Spex 1681 0.22 mm Spectrometer) and the emission analysed with a Spex 1680 Double Spectrometer. The primary radiation was passed through a UG5 glass band-pass filter to exclude the sharp lines of the Xe-lamp spectrum between 450-500 nm, when emissions from the sample in this region were investigated. A reference PMT placed in the primary beam enabled correction for intensity fluctuations of the primary beam. A series of long-pass filters were placed between the sample and the emission monochromator to remove doublets of the primary beam and also possible doublets from any strong UV luminescence. A peltier-cooled red-sensitive Hamamatsu 928R PMT was used to measure the light emitted up to ~750 nm. A Hg-lamp was used for wavelength calibration and all data were acquired at room temperature. By combining step- and slit-sizes, wavelength resolution <1 nm is achieved. The instrument is controlled, and system response correction applied, using LabVIEW based software developed in-house.

3.5 Results and Discussion

3.5.1 Pr^{3+}

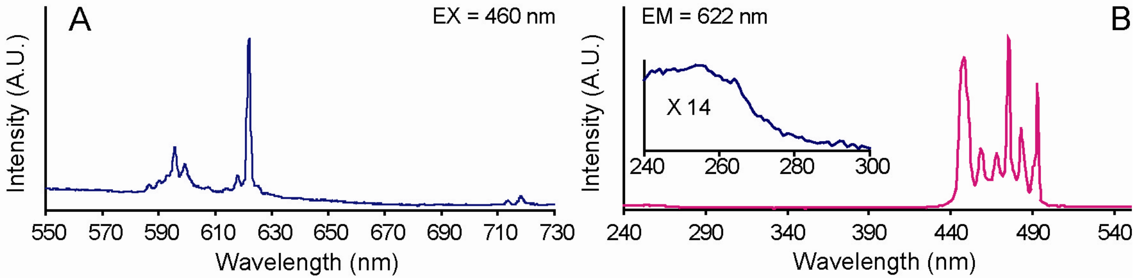

FIGURE 3.1: *Emission (A) and excitation (B) spectra of synthetic ZirPr. The inset in B shows the broad but weak excitation band in the UV region.*

Figure 3.1A shows the emission spectrum of Pr^{3+}-doped zircon. Its luminescence is dominated by peaks attributed to intra-ion energy cascades within Pr^{3+}, such as a doublet at 622 nm ($^3P_0 \rightarrow {}^3H_6$), a series of emissions centred ~595.6 nm ($^1D_2 \rightarrow {}^3H_4$) and a doublet at 713.8 and 718.2 nm ($^3P_0 \rightarrow {}^3F_4$). A very weak emission doublet occurs at 489.8 and 492.2 nm ($^3P_0 \rightarrow {}^3H_4$). The emissions corresponds to those reported for RL and IL (Karali *et al.* 2000; Finch *et al.* 2004).

Lee & Kim (2008) found that the 622 nm emission dominated under 295 nm excitation, but with 450 nm excitation the 615 nm emission dominated. Conversely, in this study the 622 nm emission dominates with 460 nm excitation. The emission intensity of the sample is relatively low compared to most of the other REE described here. Karali *et al.* (2000) and Finch *et al.* (2004) reported intense luminescence by RL and IL. The intensity dependence of excitation indicates that energy is efficiently transferred from the conducting band to Pr^{3+}.

Fig. 3.1B shows that the excitation of Pr^{3+} is dominated by a series of narrow excitation bands between 448 and 493 nm, ascribed to excitations from the ground state ($^3H_4$) to ^3P_J (J = 0 - 2) and $^1I_6$ (Jia *et al.* 2006; Li *et al.* 2007). The sample is relatively weakly luminescent, which may result in an apparent slight peak shift or intensity exaggeration of these excitation bands as they partially overlap with line emissions found in the Xe-lamp. The inset in Fig. 3.1B shows a weak excitation band between ~275 and 240 nm. Broad UV excitation bands have been reported in several Pr^{3+} doped materials (*e.g.* Gaft *et al.* 1999; Oskam *et al.* 2002; Dorenbos *et al.* 2006; Jia *et al.* 2006, 2007; Li *et al.* 2007; You *et al.* 2007; Lee & Kim 2008). In Pr^{3+} the highest energy levels of the $4f^2$ configuration ($^1S_0$) are close to the lowest energy level of the 4f5d configuration, which is highly affected by the host (Oskam *et al.* 2002; You *et al.* 2007). The 4f5d level can either be above (energetically) or overlap with the $^1S_0$ level, but in either case peaks rather than a plateau would be expected. Dorenbos *et al.* (2006) found a similar broad plateau-like excitation band between 238 and 265 nm in $LaBr_3$:Pr, which they ascribed to a charge transfer (CT) band. Based on the similarity in shape of the UV excitation band to that described by Dorenbos *et al.* (2006) it is ascribed to charge transfer between the lattice and Pr^{3+}.

Shinno (1987) reported the dominant Pr^{3+} emissions to coincide with the 480 and 580 nm emissions of Dy^{3+} under UV excitation (330-380 nm), with no emission above 576 nm. The Pr-doped sample studied here has no significant excitation bands in the excitation region applied by Shinno (1987). Given the overlap of this emission with Dy^{3+} and that the strongest excitation band of Dy^{3+} is ~350 nm, it seems likely that the sample analysed by Shinno (1987) was contaminated with Dy^{3+}.

3.5.2 Sm^{3+}

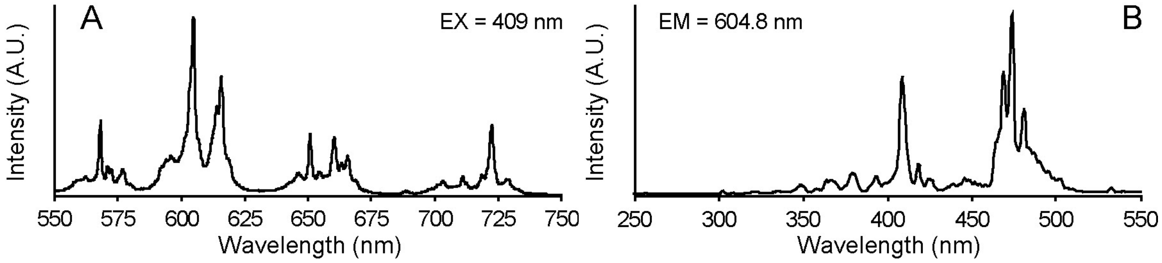

FIGURE 3.2: *Emission (A) and excitation (B) spectra of ZirSm.*

The emission spectrum of Sm^{3+} doped zircon is shown in Fig. 3.2A. The spectrum consists of four emission bands arising from transitions within Sm^{3+} from the excited $^4G_{5/2}$ state to $^6H_{5/2}$ (568 nm), $^6H_{7/2}$ (604.8 nm), $^6H_{9/2}$ (650.8 nm) and $^6H_{11/2}$ (722.6 nm) with 604.8 nm being dominant. In detail, each emission band comprises a series of minor features ascribed to crystal field splitting. Figure 3.2B shows that the excitation spectrum of the 604.8 nm emission is dominated by 474 and 409 nm absorptions from excitation of the ground state ($^6H_{5/2}$) to $^4G_{9/2}$ + $^4I_{15/2}$ and $^4K_{11/2}$, respectively. No differences were observed in the excitation spectra for the various emission bands. The excitation spectrum reveals the same splitting of the energy levels into several sublevels as observed for the emission spectrum.

3.5.3 Eu^{3+}

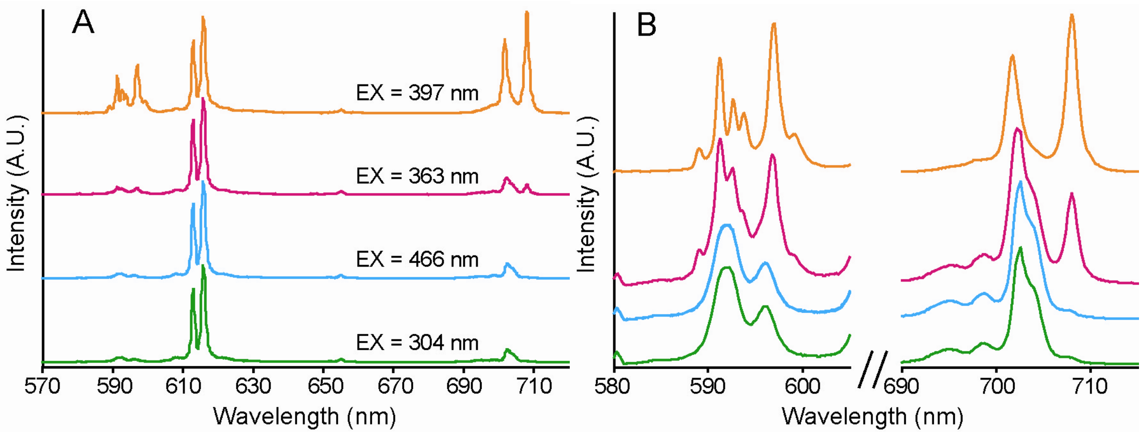

FIGURE 3.3: *Emission spectra of ZirEu under four different excitations. The intensities of the spectra in (A) have been normalised to the intensity of the 616 nm emission. (B) shows details of the effect different excitations have on the emissions of* $^7F_{0,1,4}$.

Figure 3.3 show the emission spectrum of ZirEu collected with four different excitations and normalised to the intensity of the 616 nm emission. The emissions originate from transitions between $^5D_0 \rightarrow {}^7F_J$ (J = 0 – 4) levels. Fig. 3.3A shows that the spectra under 304 and 466 nm excitation are similar and dominated by the 616 nm emission (J = 2). Eu PL is particularly informative in determining local site-symmetry (*e.g.* Blasse 1975; Jagannathan & Kottaisamy 1995; Gaft *et al.* 1997, 2000b; Nasdala *et al.* 2004a). Fig. 3.3B shows a weak 580.4 nm emission (J = 0) indicating that only one Eu^{3+} site is present as the transition to the $^7F_0$ level is forbidden and non-degenerate. The 580.4 nm emission is a singlet under all excitations. However, due to the intensity of the J = 1 emission (~595 nm) under 397 nm excitation, the emission appears absent. The J = 1 emissions are found as two broad lines centred at 592 and 596 nm under 304 and 466 nm excitation. However, with 363 nm excitation the broad emissions are split into four sharp peaks with two small shoulders, and with 397 nm excitation six sharp peaks can be identified. The splitting of the broad emission also shifts the position of the peaks slightly so that the strongest emissions with 397 nm are placed at 591.2 and 597 nm. For the 304, 363 and 466 nm excitations the higher energy transition (591.2 nm) dominates the J = 1 emissions but for 397 excitation the lower energy transition (597 nm) dominates. The weak J = 3 emission (655 nm) is present under all excitations.

One main emission related to J = 4 is found ~702.6 nm with a shoulder at the lower energy side and three weak emissions centred ~695, 698.8 and 708 nm with 304 and 466 nm excitation. The 708 nm emission is well-defined under 363 nm excitation and with 397 nm excitation it is the dominant emission in the spectrum. With 397 nm excitation, the shoulder on the lower energy side of the 702.6 emission has disappeared and as a result the single emission has moved to 701.8 nm. The differences in excitation is readily recognised in the excitation profiles of selected emission bands (Fig. 3.4).

Figure 3.4 shows that most of the excitation bands are typically narrow bands, but a broad band is centred ~304 nm. Similar bands have been ascribed in other materials to a charge transfer between an anion and the Eu^{3+} ion (*e.g.* Marimuthu *et al.* 2001; Li *et al.* 2006; Ferdov *et al.* 2008). For both the 596 and 708 nm emissions the 383 nm excitation dominates, whereas the 363 nm excitation dominates for the 616 nm emission.

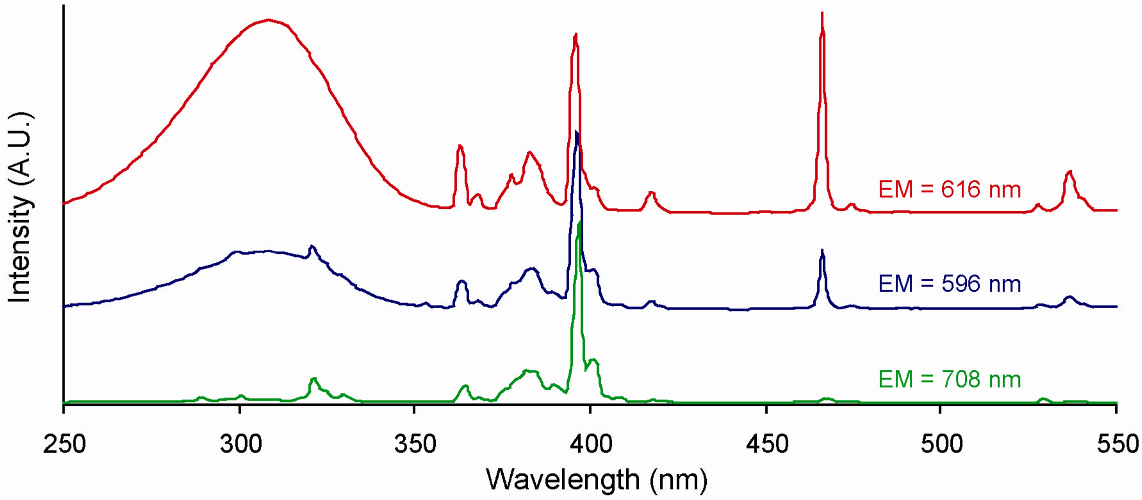

FIGURE 3.4: *Comparison of excitation spectra for three emission bands normalised to the 397 nm excitation band in Eu^{3+}-doped $ZrSiO_4$.*

When comparing the intensity between the 466 and 383 nm excitations, the former is significantly lower, slightly higher and significantly higher for the 708, 596 and 616 nm emissions, respectively. The changes in relative intensities between different excitation bands are caused by certain excitation bands being site-selective. CT bands are dependent on the distance between the Eu^{3+} and the coordinating O^{2-}, *i.e.* will only excite a specific site. On the other hand, 397 nm excitation corresponds to direct excitation of the $^7F_2$ level and hence will excite all Eu^{3+} present in the material. Although it was not possible to identify more than one site based on the 580 nm emission, the excitation spectra and the differences in the detailed emissions (Fig. 3.3B) indicate Eu^{3+} in more than one site. This is in agreement with Gaft *et al.* (2000b) who found three different sites in a synthetic Eu^{3+} doped zircon based on polarisation- and time-resolved luminescence.

3.5.4 Gd^{3+}

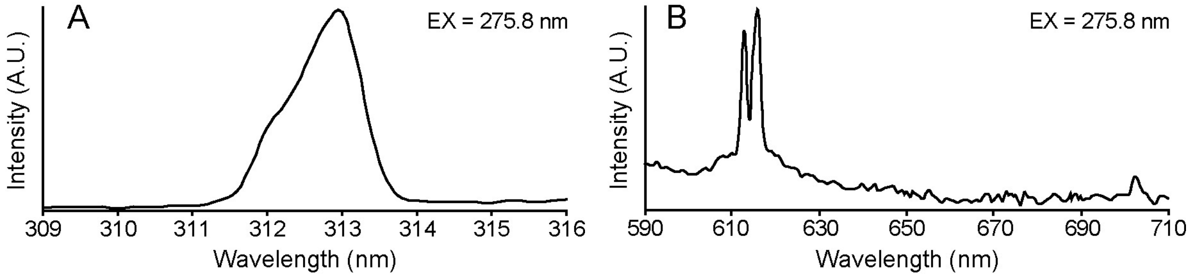

FIGURE 3.5: *Emission spectra of ZirGd under 275.8 nm excitation. (A) shows the well-known Gd^{3+} emission from the $^6P_{7/2} \rightarrow {}^8S_{7/2}$ transition, but also the presence of a shoulder at the high-energy side. (B) shows a doublet around 614 nm and a weak emission around 700 nm.*

Figure 3.5A shows the Gd^{3+} emission band centred around 313 nm, associated with energy transfer $^6P_{7/2} \rightarrow {}^8S_{7/2}$. However, there is a shoulder on the high-energy side (approximately 312 nm) indicating that the emission is related to energy transfer between sublevels of either the ground or excited states of Gd^{3+} (Wybourne 1966). Fig. 3.5B reveals a doublet in the red region with wavelengths 613 and 616 nm and a weak emission band ~700. Karali *et al.* (2000) mention that this sample is contaminated with another element, but do not suggest which. Finch *et al.* (2004) also observed the emissions, but ascribed them to artefacts in the detector.

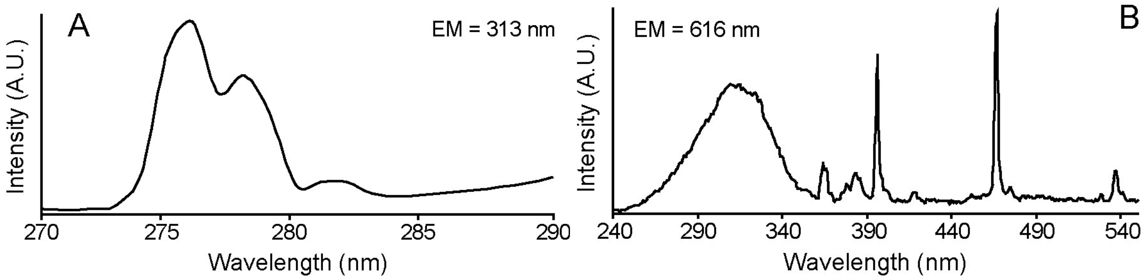

FIGURE 3.6: *Excitation spectra of the 313 (A) and 616 nm emission in ZirGd. (A) reveals a triplet of excitations related to the ^6I_J level in Gd^{3+}. (B) does not resemble a Gd^{3+} excitation spectrum, but is similar to that in Fig. 3.4.*

The excitation spectrum of the 313 nm emission (Fig. 3.6A) shows at least three bands (275.6, 276.8 and 281.8 nm) that relate to energy transitions between the ground state $^8S_{7/2}$ and the ^6I_J level. The presence of several excitation bands suggests that a number of ^6I_J levels are excited, but all pass the energy on non-radiatively to the $^6P_{7/2}$ level. The excitation spectrum of the 616 nm emission does not resemble that of the 313 nm emission (Fig. 3.6B). However, the low energy luminescence in the sample is consistent with emissions from Eu^{3+} (Fig. 3.3). Energy transfer from Gd^{3+} to Eu^{3+} can in some materials have the ability to emit two photons (from Eu^{3+}) for each absorbed photon (by Gd^{3+}), which in principle can give a quantum efficiency >100 %, called quantum cutting (Wegh *et al.* 1999). Two decay mechanisms are described by Wegh *et al.* (1999) – the first involves excitation of the high energy level (^6G_J) of Gd^{3+} followed by cross-relaxation energy transfer to the ^7F_J level in Eu^{3+} causing excitation to the $^5D_0$ level, which can then return to the ground state creating luminescence as described for ZirEu. The second mechanism involves energy transfer from the ^6P_J level in Gd^{3+} to energy levels in Eu^{3+} followed by a fast relaxation to the $^5D_0$ state in Eu^{3+} prior to emission.

Another possible mechanism for energy transfer from Gd^{3+} to Eu^{3+}, not considered by Wegh *et al.* (1999), does not involve direct energy transfer between the two lanthanides, but energy transfer via the host matrix. A comparison of the emission spectrum of Gd^{3+} with the excitation spectra of Eu^{3+} (Figs. 3.4 and 3.5A) shows that the 313 nm emission of Gd^{3+} coincides with the broad CT excitation band of Eu^{3+}. It is possible that a small fraction of the energy emitted from the transfer $^6P_{7/2} \rightarrow {}^8S_{7/2}$ in Gd^{3+} is absorbed by the CT band of Eu^{3+}, resulting in Eu^{3+} emission.

3.5.5 Dy^{3+}

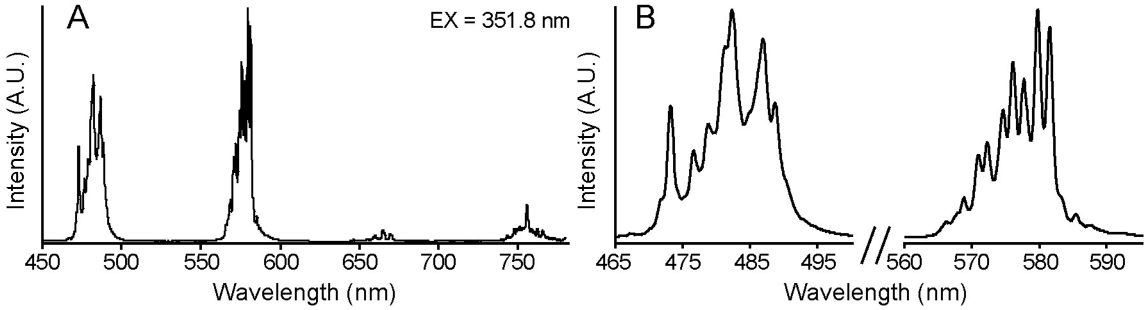

FIGURE 3.7: *Emission spectrum of ZirDy under 351.8 nm excitation. (A) shows the four main groups of emission bands and (B) details of the 480 and 580 nm emission bands.*

Figure 3.7A shows that the emission spectrum in ZirDy consists of four groups of bands centred around 480, 580, 666 and 765 nm corresponding to emissions from $^4F_{9/2} \rightarrow {}^6H_{15/2}$, $^6H_{13/2}$, $^6H_{11/2}$ + $^6F_{11/2}$ and $^6H_{9/2}$, respectively in Dy^{3+}. The 580 nm emission is the strongest. The same emissions were observed in RL by Karali *et al.* (2000) and IL by Finch *et al.* (2004). The latter found the main bands split into several sublevels, which is also the case in PL (Fig. 3.7B). Shinno (1987) observed the same general emission bands, but found the spectrum to be dominated by the 480 nm emission.

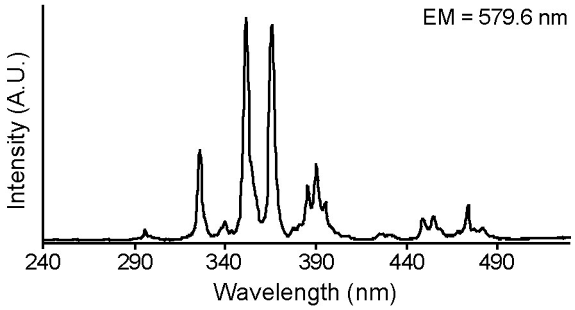

FIGURE 3.8: *Excitation spectrum of the 579.6 nm Dy^{3+} emission in ZirDy.*

Figure 3.8 shows the excitation spectrum for the strongest emission (579.6 nm). The two strongest excitation bands are at 351.8 and 366 nm and are associated with excitation from the ground state ($^6H_{15/2}$) to $^6P_{7/2}$ and $^6P_{5/2}$, respectively. No differences were observed in the excitation spectra for the different emission bands indicating that the energy transfer from the excited levels to the emissions band are the same and that only one site is present.

3.5.6 Ho^{3+}

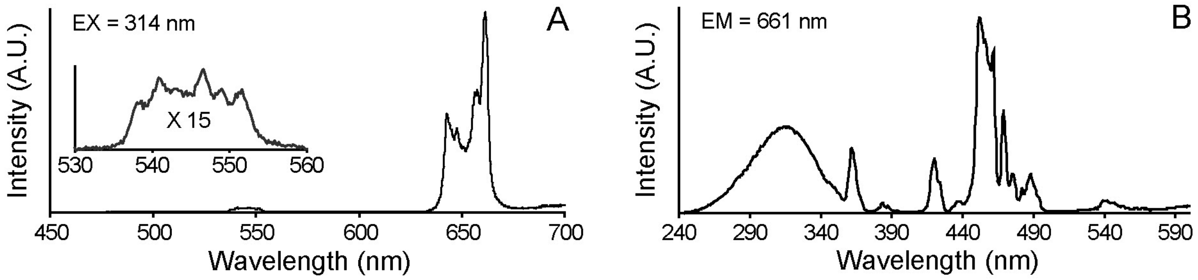

FIGURE 3.9: *Emission (A) and excitation (B) spectra of ZirHo. The inset in (A) show details of the weak 545 nm emission.*

Figure 3.9A shows the emission spectrum for Ho^{3+} doped zircon under 314 nm excitation, which is dominated by two doublets at 661.4/657 nm and 643/648 nm ($^5F_5 \rightarrow {}^5I_8$) and a series of lines centred at 545 nm ($^5F_4/^5S_2 \rightarrow {}^5I_8$). The splitting of the main emission into two distinct bands indicates that the $^5F_5$ or $^5I_8$ level or both are split by crystal field effects into sublevels, or the presence of multiple symmetrically non-equivalent sites. The excitation spectrum (Fig. 3.9B) is dominated by a series of closely-spaced line emissions arising from excitation from the ground state ($^5I_8$) to $^5G_6$,$^5F_1$; $^3K_8$; $^5F_2$ and $^5F_3$ (*e.g.* Liu *et al.* 2005; Karmakar 2005). Additional line excitation bands are present, as well as a broad excitation band centred around 314 nm, consistent with a CT band. CT bands are commonly observed with Eu^{3+}, but they are rarely described for Ho^{3+}. Both Karali *et al.* (2000) and Finch *et al.* (2004) found that the sample was contaminated with Dy resulting in the characteristic 480 and 580 nm emission bands. However, such emissions were not observed with PL indicating that there are no direct energy transfers occurring from Ho^{3+} to Dy^{3+}. On the other hand it is not possible to rule out energy transfer from the Dy^{3+} to Ho^{3+} as the 480 nm emission band of Dy^{3+} overlaps with the $^5I_8 \rightarrow {}^5F_2$ (472 nm) and $^5F_3$ (484 nm) excitations of Ho^{3+} (Karamakar 2005). Karali *et al.* (2000) and Finch *et al.* (2004) reported luminescence after excitation of electrons above the conduction band, and with the higher power density of these excitation forms the process of exciting the Dy^{3+} states seems to be faster than the process of energy transfer from Dy^{3+} to Ho^{3+}. This explains why Dy^{3+} emissions are present in high (keV or MeV) energy excitation studies (Karali *et al.* 2000; Finch *et al.* 2004), but not in the present study which uses far lower (eV) energy excitation. Finch *et al.* (2004) showed that energy transfer to Ho^{3+} and Dy^{3+} changed during implantation, *i.e.* with increasing defect concentration, showing that the structure is important for REE luminescence.

3.5.7 Er^{3+}

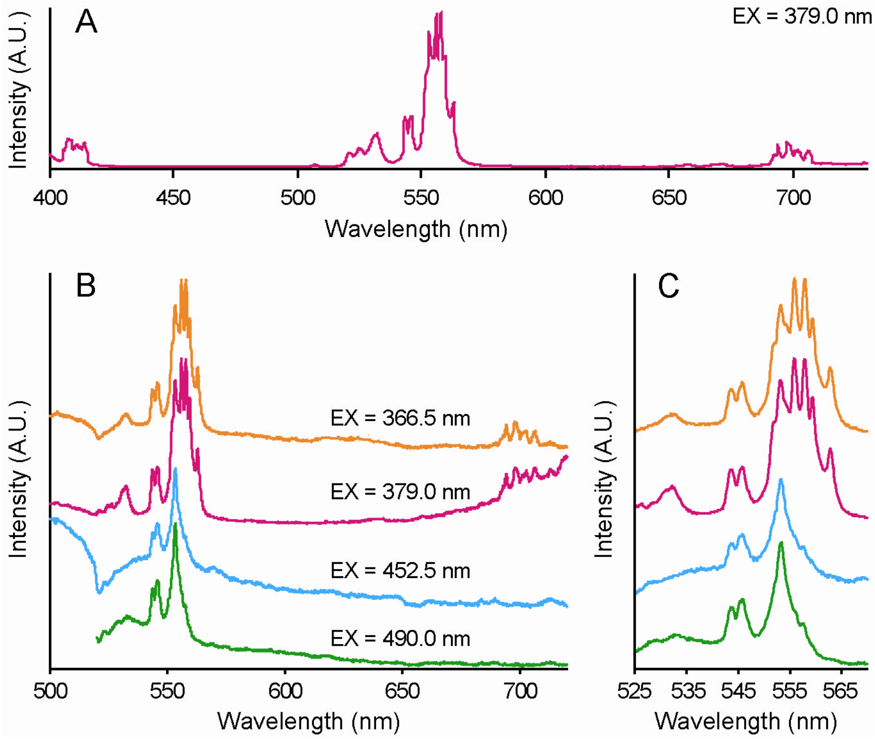

FIGURE 3.10: *Full emission spectrum of ZirEr under 379 nm excitation (A). B and C show details of the emission with four different excitations after being normalised to the 553.4 nm emission. The negative peaks at 521 and 656 nm observed in (B) correspond to optical absorption from the ground state ($^4I_{15/2}$) to $^2H_{11/2}$ and $^4F_{9/2}$, respectively. For 490.0 nm excitation the collection of emission data was not started until 520 nm to minimise background from the primary beam.*

Figure 3.10A shows the emission spectrum of Er^{3+} doped zircon under 379 nm excitation. Emission bands are found at 410, 530, 548, 556, 659, 672 and a series centred around 700 nm. The dominant emission is the 556 nm corresponding to the ($^4S_{3/2} \rightarrow {}^4I_{15/2}$) transition, which was also found to be dominant in RL by Karali *et al.* (2000). However, the PL emission differs in several ways to the RL data of Karali *et al.* (2000). Firstly, Karali *et al.* (2000) observed a strong emission band at 472 nm, which they ascribed to the transition $^2P_{3/2} \rightarrow {}^4I_{11/2}$ in Er^{3+}, but this emission was not found in the present PL study. Detailed excitation scans were carried out but did not reveal any emission around 472 nm. Second, although an emission is observed ~620 nm emission it is very weak. Third, the series of emissions around 700 nm (PL) was not observed in RL by Karali *et al.* (2000). The difference in emission spectra under the two types of excitation suggests that certain energy levels are accessible from the conduction band or cascade from the conduction band or an energy level close to the conducting band, which is outside the spectral range of the PL instrument.

Figs. 3.10B and C show how the emission bands are highly dependent on the excitation wavelength. For excitation with 452.5 and 490 nm the emission spectra are similar and dominated by the 553.4 nm emission. For 366.5 and 379 nm excitation the single peak at 553.4 is accompanied by stronger emissions at slightly lower energy giving a total of six emission bands centred around 556 nm. Excitation with 366.5 and 379 nm also results in a series of emissions around 700 nm, which are absent under the other excitations. A detailed study of the emissions from 684 to 713.4 reveals that the 684, 689.6 and 713.4 nm emissions are weak but observed under all excitations. However, emissions at 694.2, 697.6, 701.8 and 706.4 nm are only found with 366.5 and 379 nm excitation. In detail, these four peaks show further splitting into several sub levels.

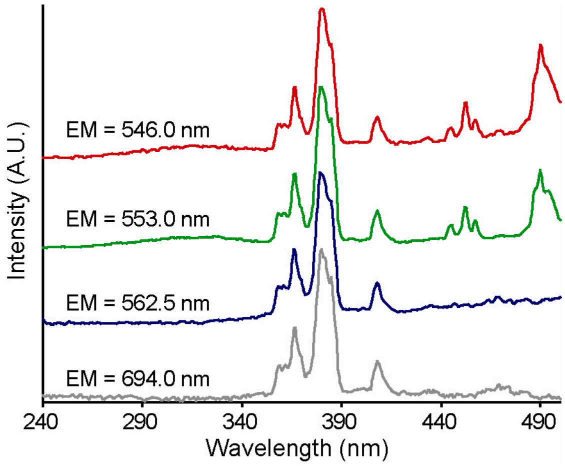

FIGURE 3.11: *Excitation spectra of four emission bands. Indicating the presence of Er^{3+} in more than one site.*

The excitation spectra of different emission bands are presented in Figure 3.11. The five main excitation bands can all be ascribed to promotion from the ground state $^4I_{15/2}$ to $^4G_{9/2}$ (367 nm), $^4G_{11/2}$ (379 nm), $^2H_{9/2}$ (408 nm), $^4F_{5/2}$ (453 nm), and $^4F_{7/2}$ (490 nm) in Er^{3+} with the 379 nm band being dominant for all emissions. Both the 453 and 490 nm excitation bands are only observed for the 546 and 553 nm emissions, which is also the case for a weak, broad excitation band ~318 nm, which could be a CT band. The variation in emission and excitation spectra of the sample indicates that Er^{3+} is present in more than one site with different site-symmetry. Site-selective excitation of Er^{3+} has been described in other host materials, although the majority of these works are dedicated to study the up-conversion properties and the site-selective properties of UV to visible excitation remain poorly understood. In a study of Gd_2SiO_5:Er^{3+} Camargo *et al.* (2002) found that the number of energy levels of the ground state is highly dependent on the site-symmetry.

3.6 Conclusions

Both the Eu and Er samples show great variations in emission spectra depending on excitation, indicating the presence of non-equivalent sites. This is consistent with Gaft *et al.* (2000b) who studied a Eu^{3+} doped synthetic zircon that was charge balanced by defect formation. It is not possible to distinguish more than two sites in data or ascribe them to possible structural sites, but the majority of REE is believed to substitute into the *Zr* site. Since REE is unlikely to substitute for Si, this confirms the presence of significant REE in interstitial sites. Of these, it is more likely that some REE would enter the distorted octahedral coordination rather than a tetrahedral site (Finch & Hanchar 2003). Although clear evidence of multiple sites was not obtained for all samples, the difference in dopant level between ZirEu and ZirEr suggests that multiple REE sites in zircon are common. The combination of time-resolved luminescence as a function of excitation energy may provide greater insights into the number of non-equivalent sites that REE occupy.

Strong CT bands were observed for Eu^{3+} and Ho^{3+} and weak ones for Pr^{3+} and Er^{3+}. The presence of CT bands in the majority of samples studied stresses the importance of considering the crystal structure when designing new materials, since a single host may efficiently mediate energy transfer to several different activators from a single UV excitation. Many lanthanide-bearing systems are superficially considered to conform to ‘free ion’ models for luminescence – the data presented here reinforce the view that the lattice plays a crucial role in the properties of lanthanide-bearing systems.

Zircon is an excellent luminescent host for REE^{3+}. However, the luminescence efficiency is highly dependent on the REE substituted, for example Eu^{3+} shows very strong luminescence whereas Pr^{3+} and Er^{3+} responses are weak. The large variation in dopant level between samples affects the luminescence efficiency in the samples, nevertheless it is clear that zircon luminescence is particularly efficient for some lanthanides and not others. The Eu^{3+} contaminated Gd sample shows energy transfer from Gd^{3+} to Eu^{3+} either directly or via a CT band, which opens up the possibility of using zircon as a host for quantum cutting. In contrast, no energy transfer was observed from Ho^{3+} to Dy^{3+} in the contaminated ZirHo sample. Energy has been shown to be efficiently transferred to Dy^{3+} in the contaminated ZirHo sample by both RL and IL excitation (Karali *et al.* 2000; Finch *et al.* 2004), but the lack of Dy^{3+} emission in this PL study suggests that the energy levels of Dy^{3+} in zircon are particularly accessible by energy cascades from the conduction band. This explains why Dy^{3+} luminescence is the most commonly observed REE^{3+} emission in the CL of natural zircons.

This study emphasises luminescence as a powerful tool to detect REE in multiple sites. Furthermore, the study illustrates how the application of different excitation sources can produce valuable information about the electronic structure of materials. Especially, when combining direct excitation of activators in the band-gap (PL) with excitation through the conduction band (RL, CL or IL). Additionally, the study shows that zircon is a promising host for designing pigments with attractive luminescent and potentially quantum cutting properties.

Chapter 4

Luminescence of Natural and Synthetic REE^{3+} Doped Fluorapatite

Luminescence of Natural and Synthetic REE^{3+} Doped Fluorapatite

4.1 Introduction

Apatite is hexagonal ($P6_3/m$) with the ideal formula $Ca_5(PO_4)_3(OH,F,Cl)$ and has two different *Ca* sites into which REE readily substitute. The two sites have different site-symmetry with *Ca1* having C_3 and *Ca2* having C_S symmetry. This has made apatite a case-study for using symmetry-dependent transitions in Eu^{3+} as a probe for Eu^{3+} distribution between different crystal sites (*e.g.* Blasse 1975; Jagannathan & Kottaisamy 1995; Gaft *et al.* 1997; Marimuthu *et al.* 2001; Piriou *et al.* 2001; Nasdala *et al.* 2004a; Li *et al.* 2006; Long *et al.* 2008).

The apatite structure can incorporate significant amounts of REE making it a much-studied mineral in geology and material science. Often, natural samples show bright cathodoluminescence (*e.g.* Roeder *et al.* 1987; Marshall 1988; Campbell & Henderson 1997; Mitchell *et al.* 1997; Barbarand & Pagel 2001; Kempe & Götze 2002), but in many cases the photoluminescence is relatively weak.

F-centres are readily formed in several mineral systems, including apatite and leucophanite, which are apparent when powders are exposed to an x-ray beam during XRD. How F-centres influence the luminescence of more complex minerals is rarely studied and hence, is poorly understood. Brooks *et al.* (2002) showed that the luminescence intensity of feldspar decreases with increased ion implantation (F-centre formation) and Friis *et al.* (2007b) found the same to occur in leucophanite. Finch *et al.* (2004) also showed a decrease in intensity with increased implantation in zircons. In addition, they also described a change in the fine structure of the 480 nm Dy^{3+} emission, which they ascribed to changes in the coordination of Dy associated with the formation of defects. Finch *et al.* (2004) also reported how implantation with N^{+} generated defect-related luminescence and made new sharp emission bands that relate to REE emission.

This chapter will explore the structural changes of the *Ca* sites with increasing REE content and how such changes influence the luminescence. Furthermore, a comparison of the response from single and co-doped synthetic fluorapatites with luminescence from natural fluorapatites will be provided together with comments on the energy transfer between REE activators. The chapter will also show how different methods of excitation give different results for the same sample and explain such behaviour. Finally, an evaluation of the REE and structure interaction and the effect of defects on the luminescence of apatite are given.

4.2 Materials and Methods

The luminescence methods applied in this chapter include PL, CL, RL and IL and are described in Section 2.1. The chemical and structural methods of characterisation for both natural and synthetic samples are described in Sections 2.2 and 2.4 and chemical results are given in Tables 1.3 and 1.4. Sample descriptions of the natural apatites are in Table 1.2 and Section 2.5.1 describes the method for making the synthetic apatites including a table with sample abbreviations and composition (Table 2.3).

4.3 Results

4.3.1 Eu^{3+}

Figure 4.1 shows the emission spectra of FAPEu3 and FAPEu20 under four different PL excitations. The emission spectra of FAPEu3 with 363 and 394 nm excitation are similar and have emissions typical for transitions between $^5D_0 \rightarrow {}^7F_J$ (J = 0 – 4) levels but they differ in the three doublets ~572, ~576 (J = 0) and ~590 nm (J = 1) (see Fig. 4.2 for detailed spectra). The emissions at 583, 601.8 and 608.2 nm (J = 2) are stronger under 300 and 464 nm excitation than under 363 and 394 nm excitation. The weak emission at 614.8 nm is only present with 363 and 394 nm excitation. The excitation-dependent emissions as well as the series ~700 nm (J = 4) are shown in detail in Fig. 4.2. The emission ~654 nm (J = 3) shows no notable changes with varying excitation. The strongest emission in both samples under all excitation is the ~618 nm emission, which shows a small peak shift from 618.4 to 618 nm as the Eu concentration increases. As the concentration is increased, the doublet ~576 nm merges into one peak and the 614.8 emission shifts to 614 nm and increases in intensity.

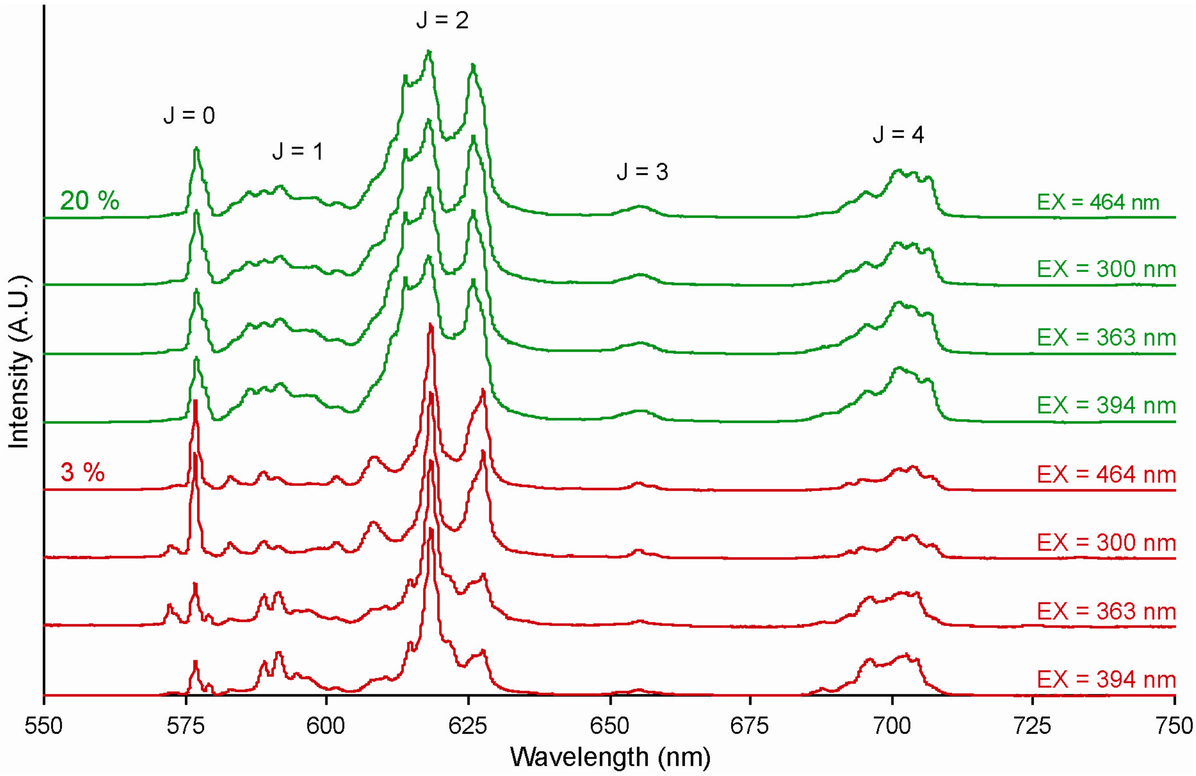

FIGURE 4.1: *PL spectra of FAPEu3 (red) and FAPEu20 (green) under four different excitations normalised to the 618 nm emission.*

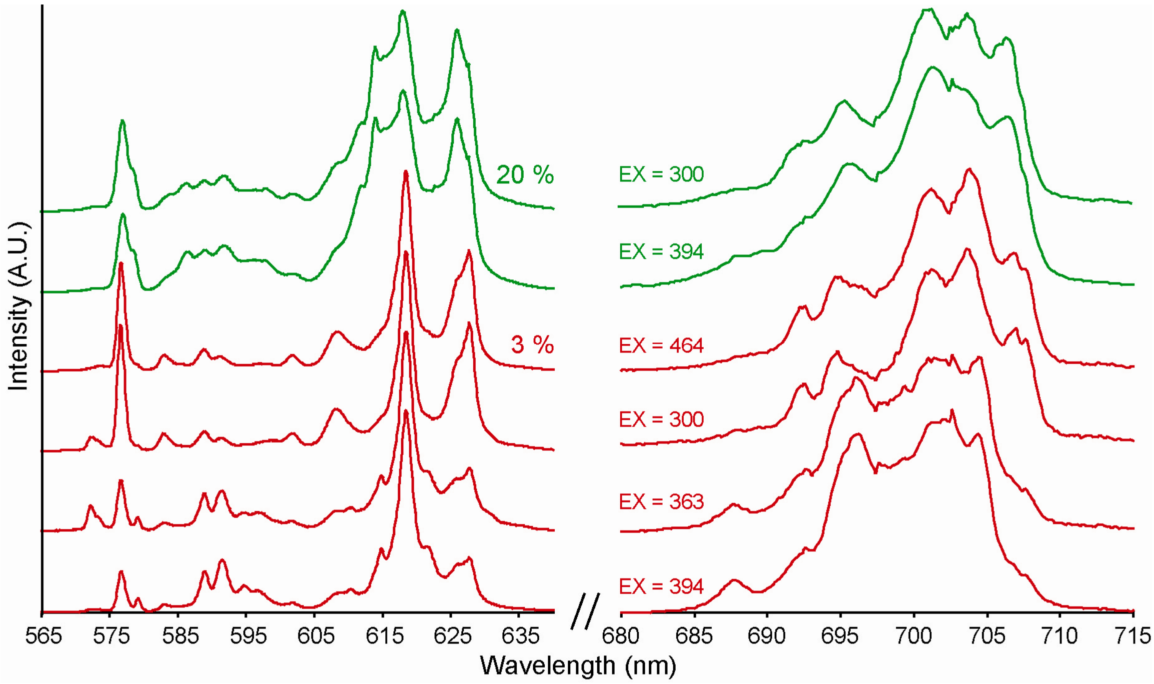

FIGURE 4.2: *Details of the emissions of FAPEu3 (red) and FAPEu20 (green) under different excitations. As only minor changes are observed for different excitations of FAPEu20 only two emission spectra are presented.*

In FAPEu3 the strong emission at 627.6 nm has a weak doublet at 626 nm, but in FAPEu20 the 627.6 nm emission is only a shoulder on the dominant 626 nm emission. The emissions of FAPEu20 do not have the same excitation dependences as FAPEu3. The only difference is in the intensity of the 614 and 626 nm emissions where the former dominates over the latter under 363 and 394 nm excitation but with 300 and 464 nm excitation the 626 nm emission is dominant.

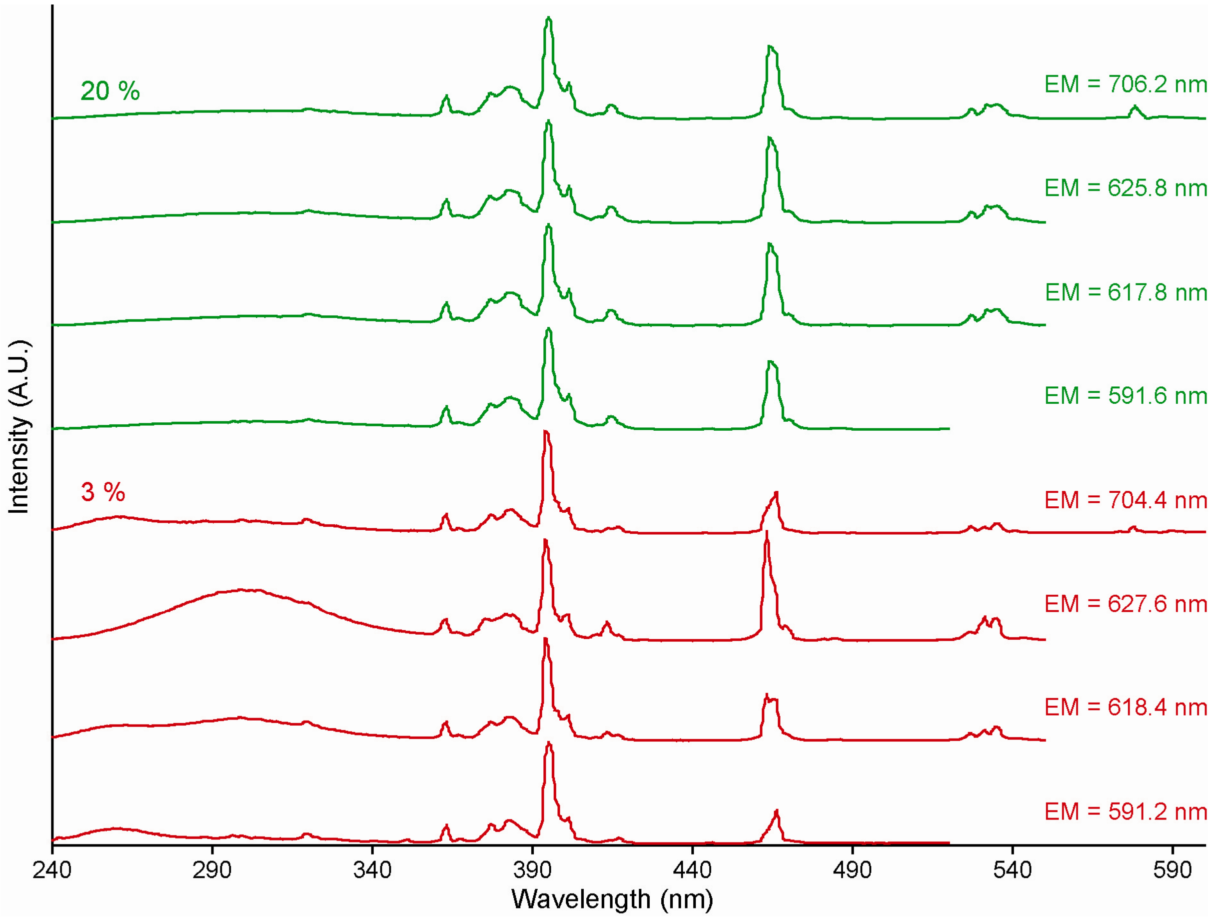

FIGURE 4.3: *Excitation spectra of four different emission bands in FAPEu3 (green) and FAPEu20 (red). All spectra have been normalised to the 394 nm excitation band.*

Figure 4.3 emphasises the differences observed in the emission spectra as a function of excitation. FAPEu3 shows that two broad excitation bands centred ~260 and ~302 nm are present for all of the FAPEu3 emission bands. Although the intensity of the 302 nm excitation band is very weak for the 591.2 and 704.4 nm emission bands, it is particular strong for the 627.6 nm band. All four emission bands, have very similar excitation profiles around the 394 nm excitation band, which is the most intense for all bands, except for the 627.6 nm emission, which is dominated by the 463 nm band excitation. This excitation is split into two bands, 463 and 466 nm, where the latter dominates the 591.2 and 704.4 nm emissions, and for the 618.4 nm emission they are equal in intensity. The intensity of the excitation bands around 535 nm is the greatest for the 627.6 nm emission. For FAPEu20 there are no differences observed in the excitation spectra for the different emission bands. They all show a broad, weak excitation band centred at 305 nm. Compared to FAPEu3, the excitation band ~464 nm does not shift for different emission bands, but the relative intensity is stronger. The remaining excitation bands are present at 320, 363, 377, 383, 401, 414, 485, and a triplet centred ~531 nm.

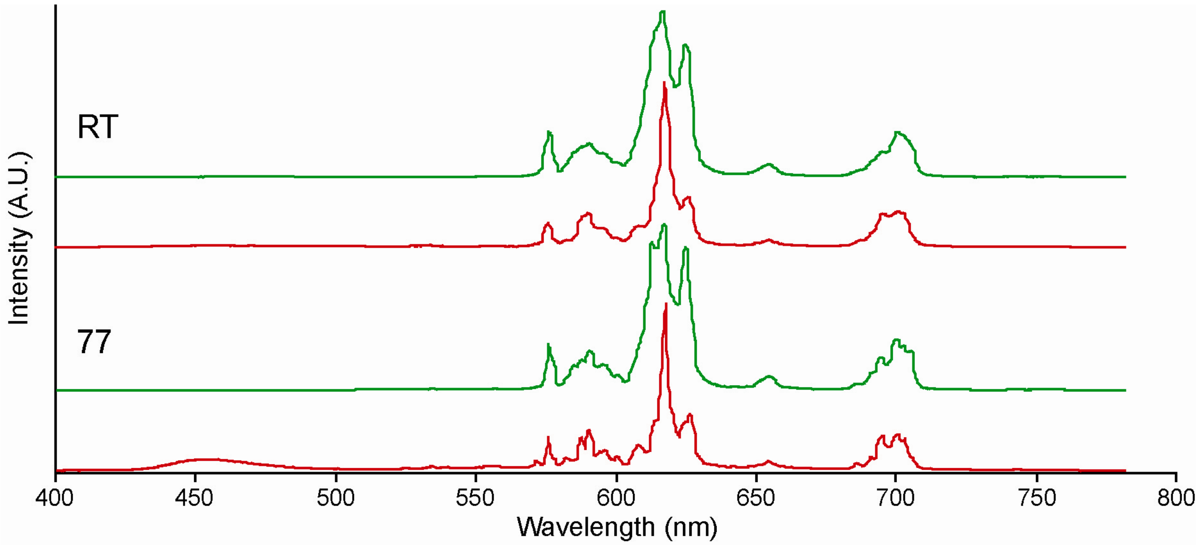

FIGURE 4.4: *The IL spectra of FAPEu3 (red) and FAPEu20 (green) at room temperature (RT) and 77 K.*

Figure 4.4 compares the IL of FAPEu3 and FAPEu20 at room temperature and 77 K. No new emission bands are observed in the extended wavelength region at room temperature compared to the PL spectra (Fig. 4.1). At 77 K a new broad emission occurs ~455 nm in FAPEu3, but not in FAPEu20. The only other change in the spectra at 77 K, compared to room temperature, is that the emission bands are all sharper and better resolved.

4.3.2 Dy^{3+}

Figure 4.5A shows that the PL spectrum of Dy^{3+} under 352 nm excitation contains four main emission at 480, 580, 666 and 765 nm, with the 580 nm emission dominating the spectrum. In addition, two weak emissions ~596 and ~704 nm are present.

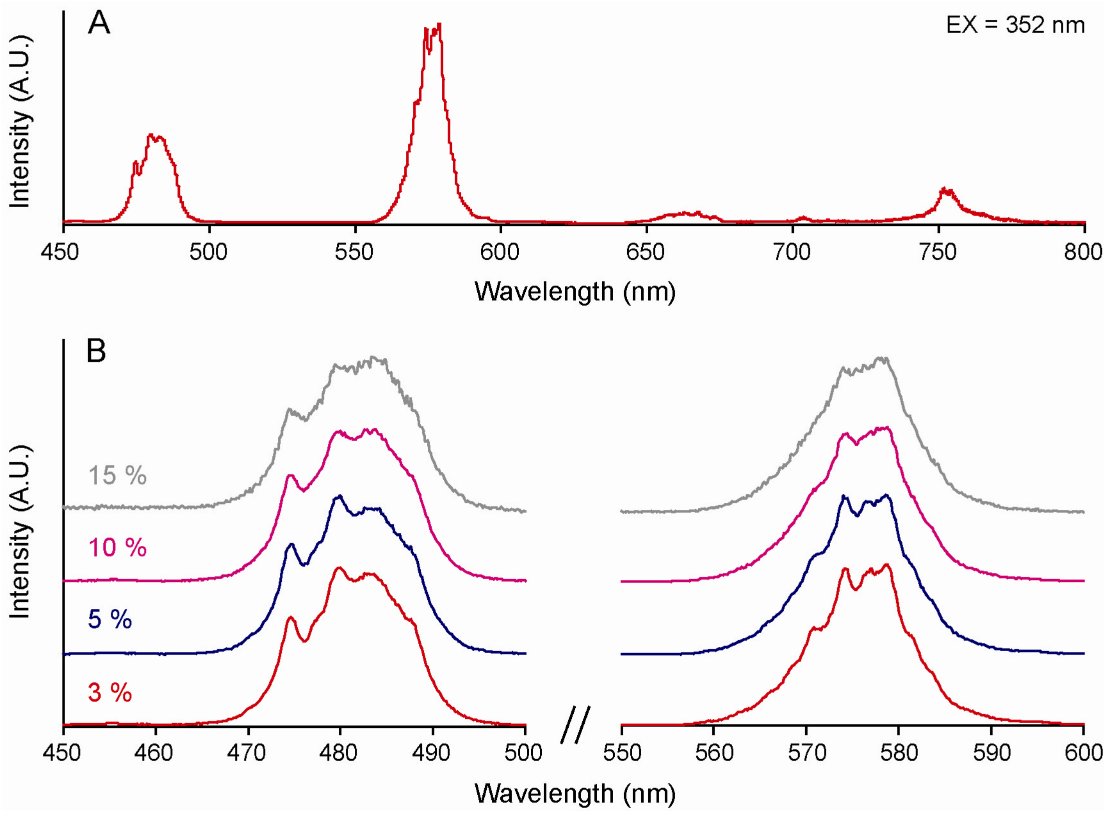

FIGURE 4.5: *Emission spectra of FAPDy under 352 nm excitation. Full spectrum of FAPDy3 (A) and changes in the 480 and 580 nm emissions with changing Dy^{3+} concentration (B).*

The detailed spectrum of the 480 and 580 nm emissions (Fig. 4.5B) demonstrates that the emission bands comprise a series of narrow emissions arising from subtle energy levels. Furthermore, the well-defined emission bands in FAPDy3 become less defined with increasing dopant level.

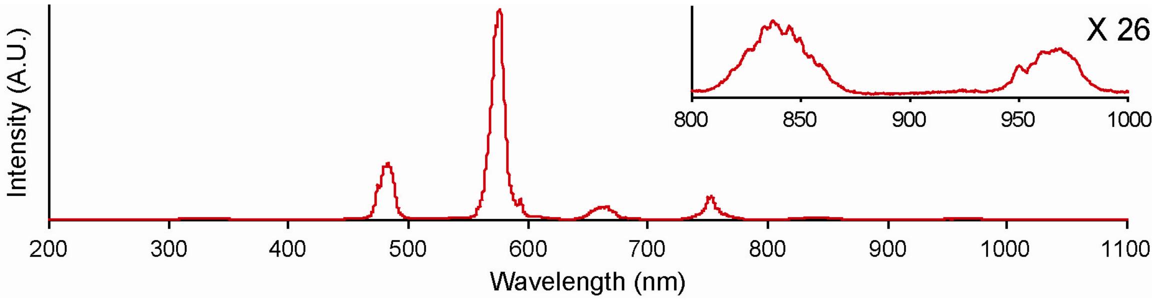

FIGURE 4.6: *IL spectra of FAPDy3. Inset shows details of two weak infrared emissions.*

The IL spectrum of FAPDy3 (Fig. 4.6) shows the same four main emissions and the weak 596 nm emission as was found in PL (Fig. 4.5A). The extended wavelength range in IL reveals two additional weak emission series in the infrared region ~845 and 966 nm (see inset in Fig. 4.6).

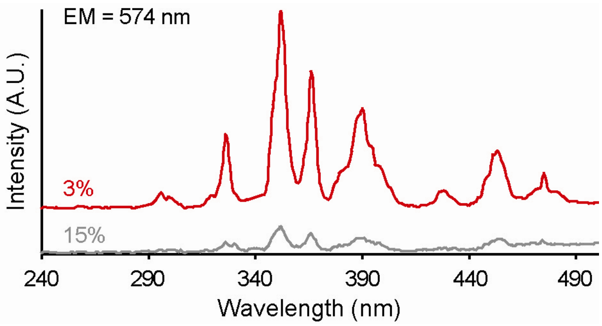

FIGURE 4.7: *Excitation spectra of the 574 nm emission in FAPDY3 and FAPDy15.*

The excitation spectra of FAPDY3 and FAPDY15 (Fig. 4.7) show that increased dopant level greatly reduces the luminescence efficiency. Line excitation bands are present at 300, 326, 352, 366, 390, 430, 453 and 475 nm and the two strongest excitation bands are 352 and 366 nm. No differences were observed in the excitation spectra for the different emission bands, but, as Fig. 4.7 illustrates, increased concentration has a strong weakening of the intensity of the excitation bands.

4.3.3 Sm^{3+}

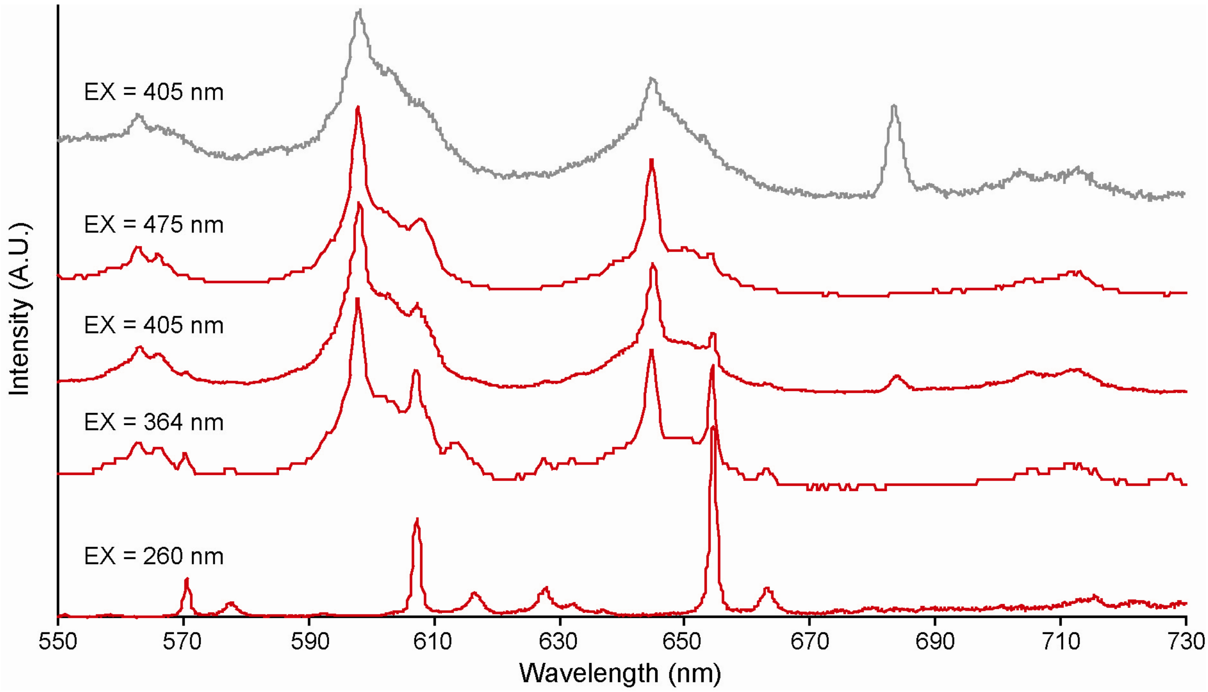

FIGURE 4.8: *Emission spectrum of FAPSm3 (red) and FAPSm15 grey) under different excitations.*

The emission spectra of FAPSm3 under 363, 405 and 475 nm excitation are similar (Fig. 4.8) and consist of four main bands at ~565, ~600, ~650 and ~705 nm, of which the 600 and 650 nm emissions are distinct doublets at 598/607 nm and 645/654.5 nm (especially visible with 364 nm excitation). The emission spectrum at 260 nm excitation lacks many of the emissions present with other excitations, including the strongest emissions at 598 and 645 nm and the spectrum is dominated by the 654.5 nm emission. All the emission bands with 260 nm excitation are also present under the other excitations, but the broadening of the emission bands, characteristic for the other excitations, does not occur. The emission spectrum of FAPSm15 under 405 nm has much broader features, and line emissions are disappearing when compared to the emission of FAPSm3 with the same excitation. The intensity of the emission bands is greatly reduced with increased dopant level, but the relative intensity of the 684 nm emission, when compared to the 598 nm emission, is stronger in FAPEu15 than in FAPSm3.

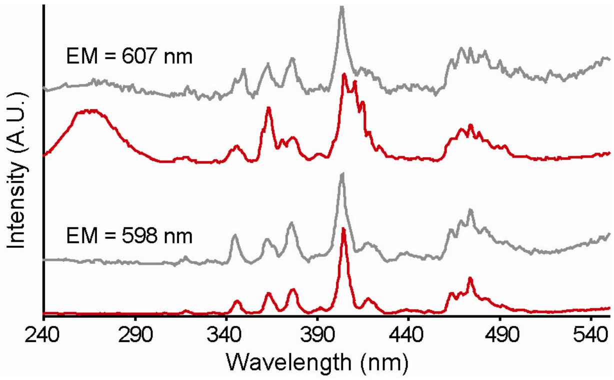

FIGURE 4.9: *Excitation spectra of FAPSm3 (red) and FAPSm15 (grey).*

Fig. 4.9 shows the difference in excitation between the 598 and 607 nm emissions and the concentration dependence in fluorapatite doped with Sm^{3+}. The main difference in the excitation spectra for the two emissions is the broad excitation band ~266 nm, which is only present for the 607 nm emission and is greatly reduced at higher Sm^{3+} content. For both emissions the strongest excitation band is ~405 nm, which, as with the remaining emission bands, is a line excitation band. Other excitation bands include: 346, 363, 376, 392, 411, 415, 418, 424, 464, 469, 474, 479 and 493 nm.

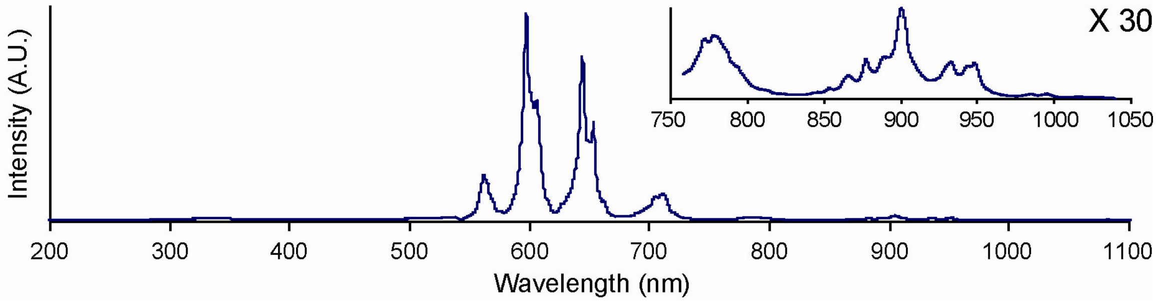

FIGURE 4.10: *IL spectrum of FAPSm5, with the four typical Sm^{3+} emissions and the inset shows additional emissions.*

Figure 4.10 shows the IL spectrum of FAPSm5, which has the same four main emissions as observed in PL (see Fig. 4.8). However, the extended spectral range for this instrument reveals an additional doublet ~776 nm and a series of emissions centred at 901 nm.

4.3.4 Ho^{3+}

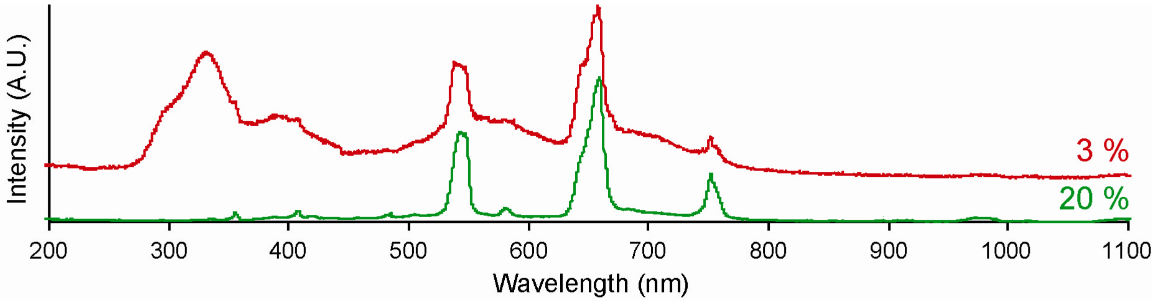

FIGURE 4.11: *IL spectra of FAPHo doped with 3 and 20 % Ho, respectively.*

The IL spectrum of FAPHo3 (Fig. 4.11) shows five line emissions dominated by an emission ~663 nm and three broad bands ~330, 400 and 560 nm. In FAPHo20 there is no evidence of the UV to blue broad emissions, but the same line emissions as in FAPHo3 as well as two at 480 and 550 nm and a weak broad emission ~980 nm are observed. The relative intensity of the three main emissions does not change with increased dopant level. No PL was detected for any of the samples.

4.3.5 Er^{3+}

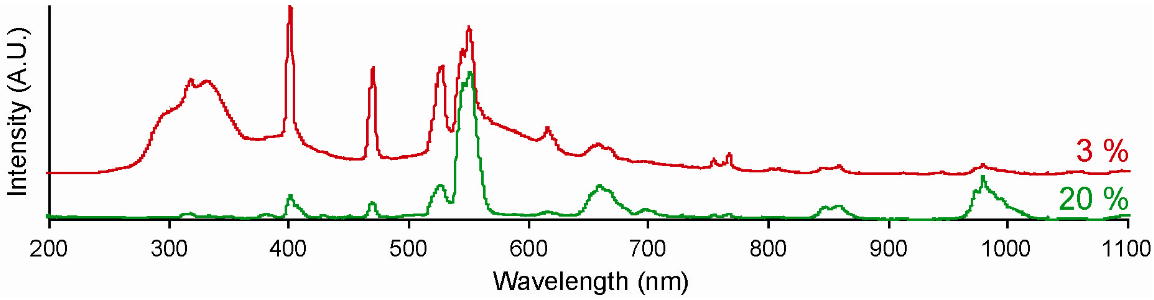

FIGURE 4.12: *IL spectra of FAPEr3 and FAPEr20.*

Figure 4.12 shows the IL spectrum of FAPEr3 with typical Er^{3+} emissions as well as broad emissions ~330 and 560 nm, similar to those observed in FAPHo3. The broad emissions are not observed in FAPEr20. Another difference between the two dopant levels is that the 402 nm emission for FAPEr3 is dominant, whereas it is the 551 nm emission for FAPEr20. There are no changes in the number of emissions between the two samples, only the relative intensities. It was not possible to detect

PL from any of the samples. However, the PL experiments revealed an absorption band ~521 nm (Fig. 4.13).

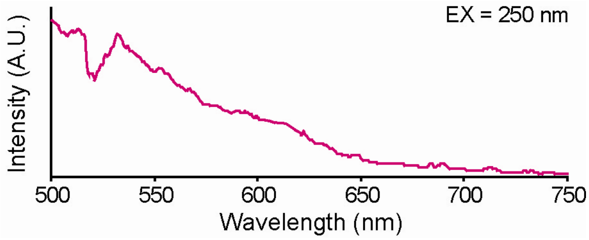

FIGURE 4.13: *PL of FAPEr10 showing no emissions bands, but an absorption band ~521 nm.*

4.3.6 Sm^{3+} and Dy^{3+} Co-doped

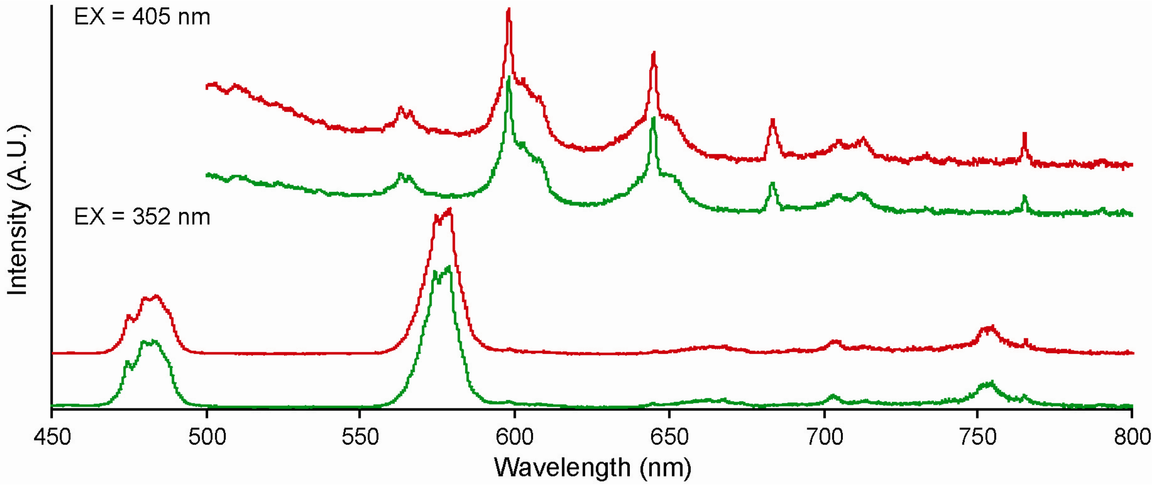

FIGURE 4.14: *The PL spectra of FAPSm0.1Dy0.05 (green) and FAPSm0.1Dy0.1 (red) under two different excitations.*

The PL spectra of the Sm and Dy co-doped samples excited by 352 and 405 nm are presented in Fig. 4.14. Each spectrum is indistinguishable from the single-doped materials (Figs. 4.5 and 4.8) under the same excitations. The different Dy content between the samples does not change the emission spectra significantly.

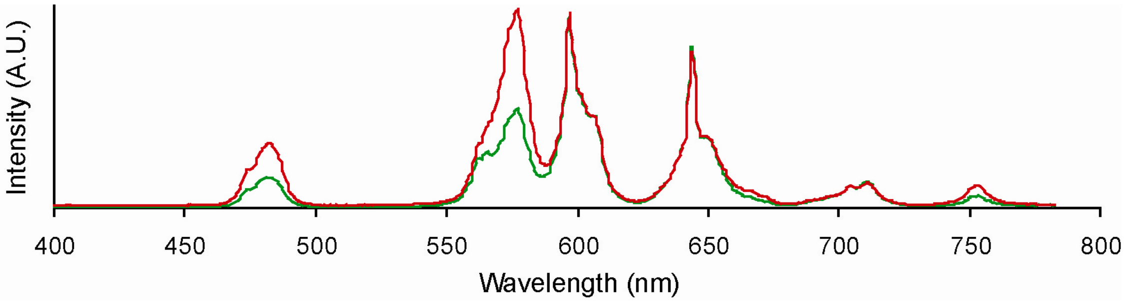

Figure 4.15: *IL spectra of the two co-doped fluorapatites FAP Sm0.1Dy0.05 (green) and FAP Sm0.1Dy0.1 (red). The intensities have been normalised to the 597 nm Sm^{3+} emission.*

Figure 4.15 shows the IL of the two samples after the intensities have been normalised to the 597 nm Sm^{3+} emission. Doubling the Dy content also amplifies the intensity of the Dy^{3+}-related emissions 2.1, 2.0 and 1.8 times for the 482, 577 and 753 nm emissions, respectively.

In the duration of the IL experiments the relative intensities of some emissions changed. Figure 4.16 shows how the emissions intensities of Sm and Dy respond differently to prolonged beam exposure, *i.e.* the intensity of the Dy emission relative to the Sm emission as a function of beam exposure.

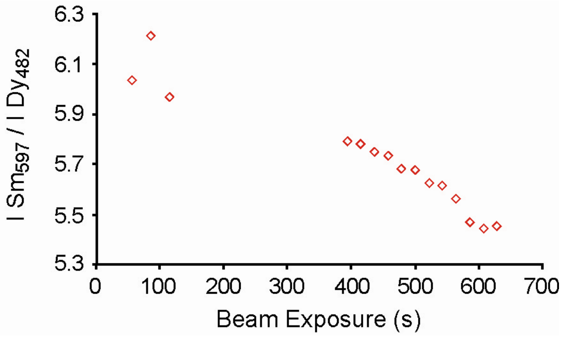

FIGURE 4.16: *The intensity of the 597 nm Sm^{3+} emission over the 482 nm Dy^{3+} emission as a function of beam exposure of sample FAPSm0.1Dy0.05. The gap is caused by data being collected in the IR region at those times,* i.e. *outside the Dy^{3+} emission range.*

The excitation bands for the two co-doped samples (Fig. 4.17) are similar to the same emission bands of the single doped materials (Figs. 4.7 and 4.9).

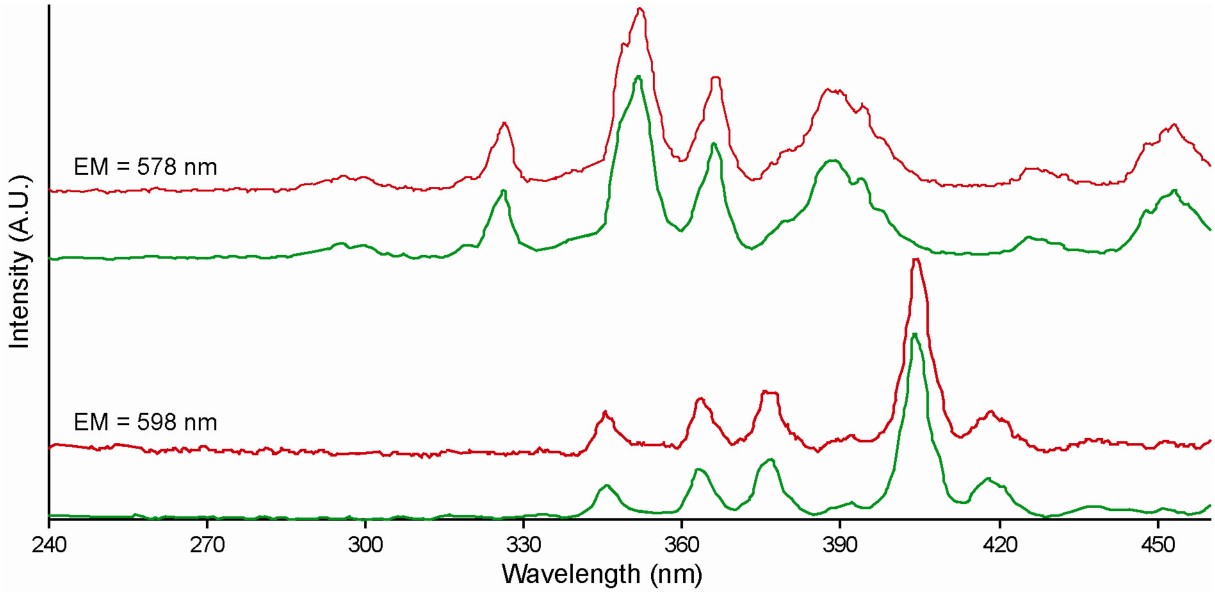

FIGURE 4.17: *Excitation spectrum of the Sm^{3+} (598 nm) and Dy^{3+} (578 nm) emissions in FAP Sm0.1Dy0.05 (green) and FAP Sm0.1Dy0.1 (red).*

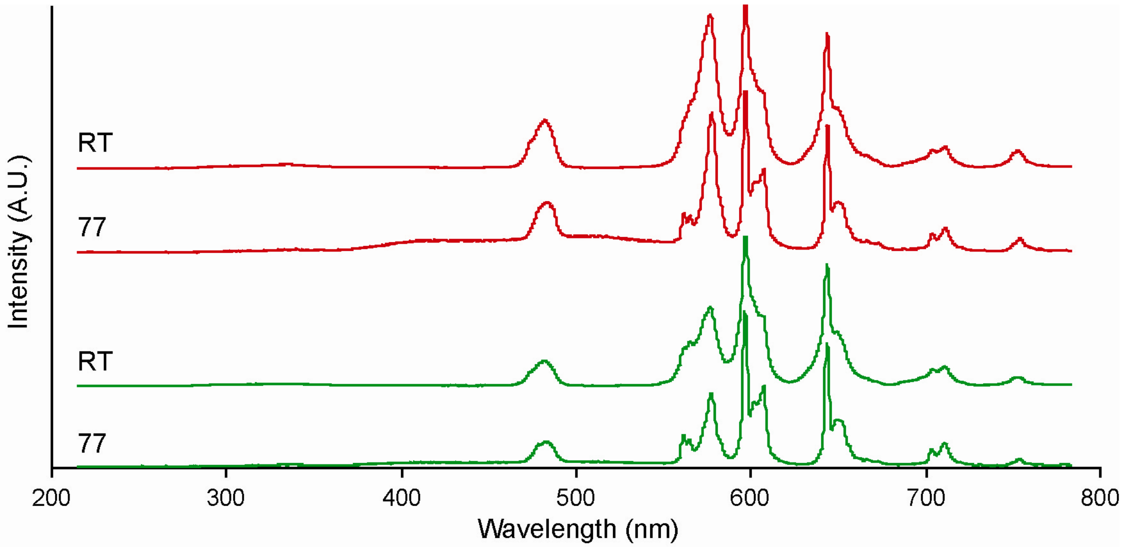

Figure 4.18: *Comparison between room temperature (RT) and 77 K (77) IL for FAPSm0.1Dy0.05 (green) and FAPSm0.1Dy0.1 (red).*

Figure 4.18 compares the ionoluminescence of the co-doped samples at room temperature and at 77 K. The emission bands narrow at low temperature and the peaks are better resolved. For example, at room temperature FAPSm0.1Dy0.1 has a broad asymmetric emission around 580, but at 77 K emission bands for both Sm^{3+} and Dy^{3+} can be distinguished, which is also the case for the two main Sm^{3+} emissions. A weak broad emission between ~370 and 540 nm is present at low temperature in both samples, but most intense in FAPSm0.1Dy0.1.

4.3.7 Natural Apatite

4.3.7.1 IL, CL and RL

The IL spectra for DUR and GAR are presented in Fig. 4.19. DUR was analysed parallel to both *c* and *a* axes, labelled DUR C and A, respectively. The IL spectra of the natural fluorapatites consist of a series of line emissions and a broad emission in the UV-Blue region. GAR has a weak line emission 312.5 nm, which is not observed in DUR and the broad emission ~375 nm in GAR has a shoulder ~360 nm, whereas for DUR the broad emission is centred ~354 nm. The following emissions are observed in the samples: 487, 548, 568-580, 598, 617, 645, 653, ~705, 756, ~803, 875-905 nm and a series ~1057 nm. The 653 nm emission becomes more distinct at low temperature, whereas the emissions ~803 nm disappear.

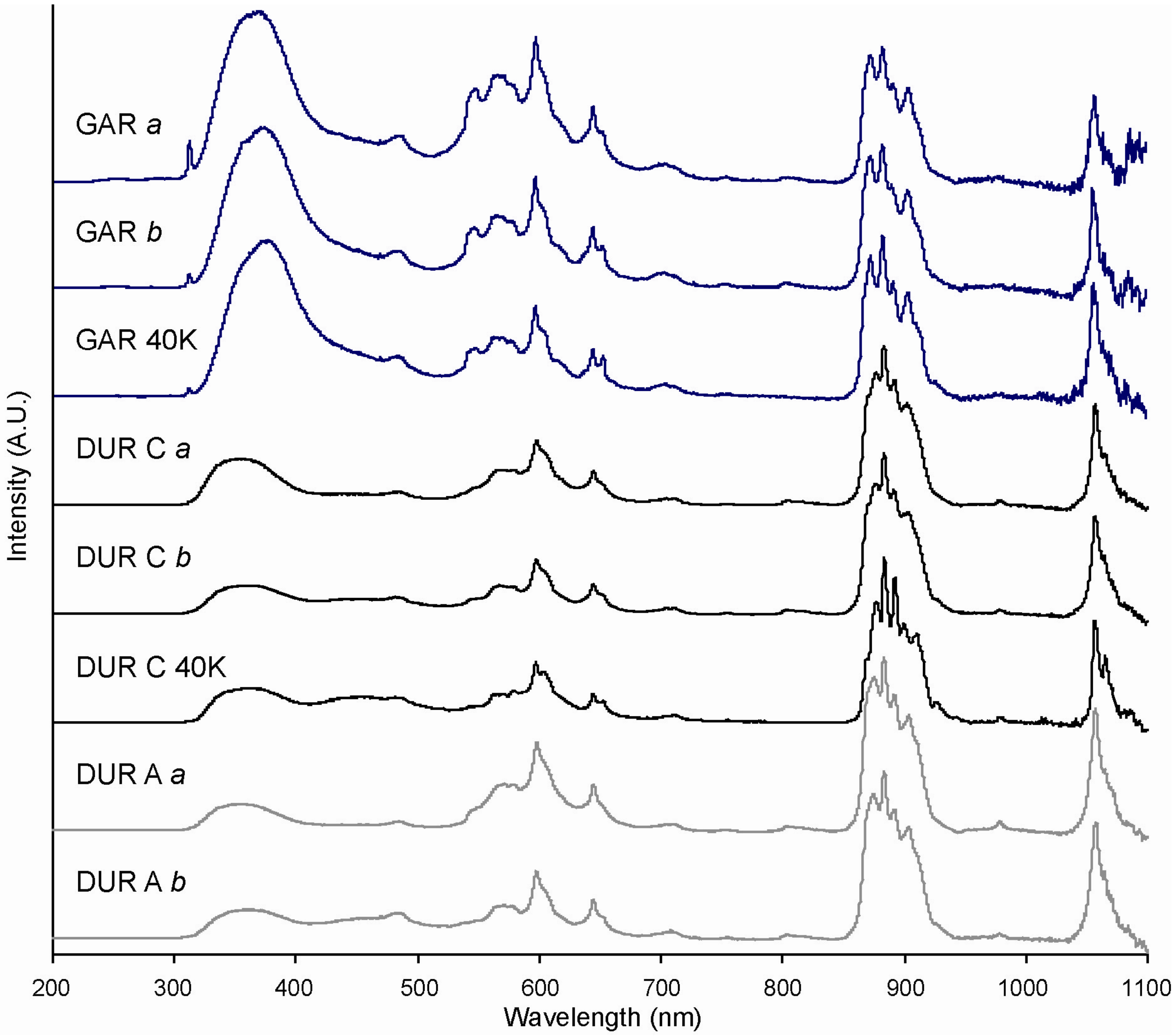

FIGURE 4.19: *IL of two natural fluorapatites. DUR C and DUR A are the same sample analysed parallel to the* c *and* a *axes, respectively. The italic suffixes "a" and "b" represent data collected immediately after sample alignment and after implantation. Most samples are at room temperature but 40K refers to the temperature of the measurement.*

At low temperature, a weak broad emission appears ~450 nm in DUR, which is not observed in GAR. The UV-Blue emission experiences a small peak shift towards lower energy during the implantation. There is no significant change in IL between the two different orientations of DUR.

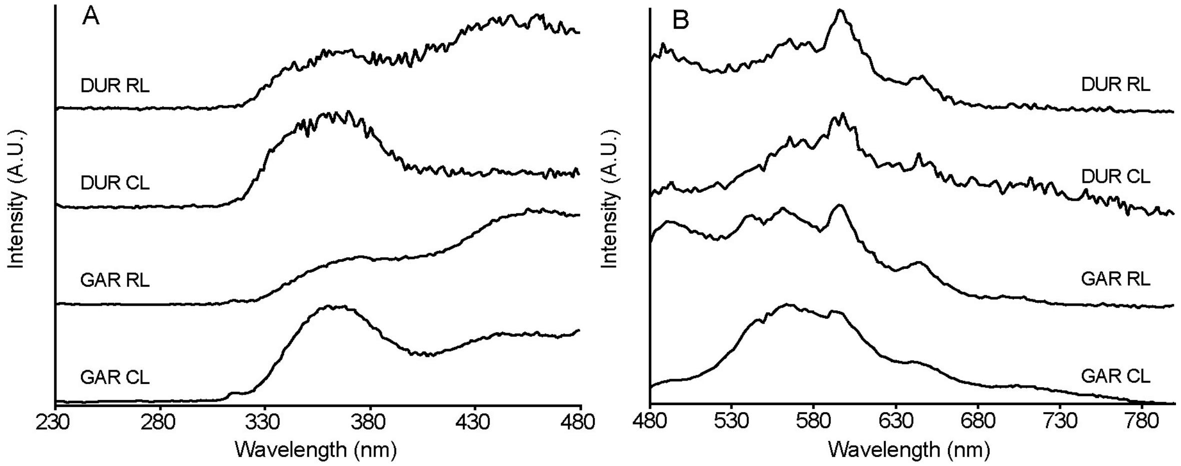

FIGURE 4.20: *RL and CL of DUR and GAR.*

In CL, both samples are dominated by a broad emission centred ~360 nm and GAR has an additional weak broad emission ~440 nm (Fig. 4.20A). However, in RL both samples are dominated by a broad emission ~460 nm. The main difference between CL and RL in the visible region Fig. 4.20B, is that the emission ~490 nm is more dominant in RL than in CL. In spite of the lower wavelength resolution of the system, the same emissions are observed for RL and CL as in IL (Fig. 4.19). However, in IL there is a difference in position of the UV emission between the samples, which is not apparent in RL in CL.

4.3.7.2 PL

The natural samples were screened with a Long-Wave UV-lamp, such as that used by amateur mineralogists, in order to select samples for PL. However, the majority of apatites display no or only weak luminescence. As a result, the quality of data collected is not of a similar signal-to-noise standard as that of the other materials and methods in this study. Therefore, in line with the aim of this chapter, only a few selected results are presented.

During a break in sample alignment of ILI, it was noticed that the PL intensity slowly decreased. A new sample was mounted and Fig. 4.21 shows the intensity of the luminescence as a function of time. Although the data are presented as starting at time zero, the sample had already been moved slightly to optimise its position and hence been exposed to the beam. The two linear parts can be resolved into two decay components with life-times of ~45 and ~126 s, respectively.

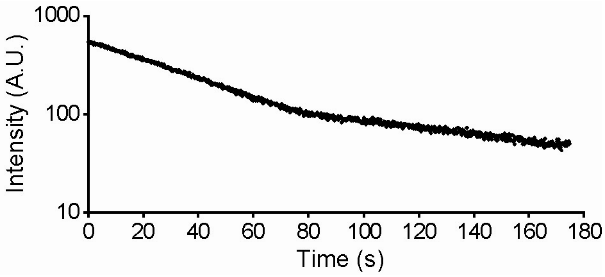

FIGURE 4.21: *The log intensity as a function of time during alignment of ILI. The excitation is ~360 nm and the emission ~580 nm.*

The emission spectra for five samples under 405 nm excitation are presented in Figure 4.22. The emission intensities are generally low, especially for ILI and SHI, revealed by the sloping background. No differences are observed between samples and all are dominated by the strong emission ~598 nm. The emissions are similar to those observed under 405 nm excitation of the synthetic Sm doped fluorapatite (Fig. 4.8).

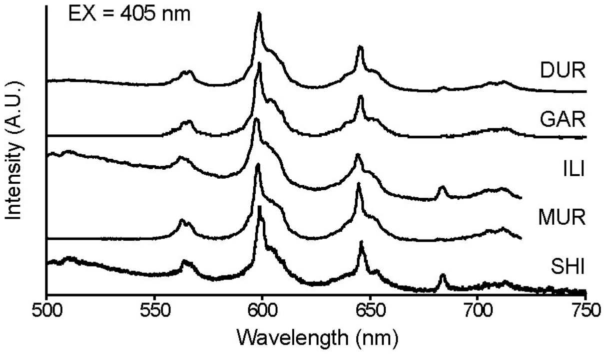

FIGURE 4.22: *PL emission spectra of five natural apatites*

Excitation spectra for the 598 nm emission of five apatites are shown in Fig. 4.23. A broad excitation ~310 nm is dominant in DUR and MOI, and for DUR it gradually decreases in intensity at higher energy whereas it for MOI decreases slightly to a constant level. All samples show the 405 and 475 nm excitation and for DUR and MUR the 449 nm excitation is very strong. The excitation spectra are similar to those of the synthetic Sm-bearing fluorapatite (Fig. 4.9), but lacking the fine structures.

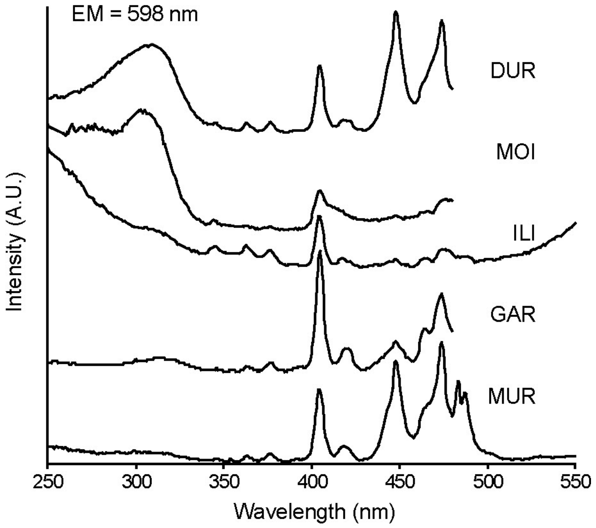

FIGURE 4.23: *Excitation spectra of five natural apatites.*

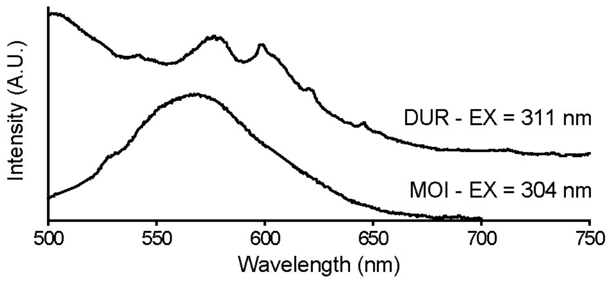

FIGURE 4.24: *Emission spectra of two natural apatites under UV excitation.*

To explore the nature of the broad excitation band ~310 nm two emission spectra are presented in Figure 4.24. The emission spectrum of DUR consists of a series of line emissions similar to the RL and CL (Fig. 4.20), whereas MOI consists of one broad emission band centred ~565 nm.

4.3.8 XRD

The unit cell parameters for 11 natural apatites (from single-crystal structure refinement) and five synthetic (from powder refinement) are presented in Figure 4.25. There is an inverse correlation between the length of the *a* and *c* axes (Fig. 4.25A) for the natural samples, but a positive one for the synthetic samples. MOI and GAR do not follow the general trend of the natural samples. Fig. 4.25B shows a positive correlation between the unit cell volume and the length of the *a* axis, whereas the influence of the *c* axis on the volume is less prominent (Fig. 4.25C). Figure 4.25 also presents a selection of distortion parameters for the *Ca* polyhedra of the natural apatites calculated using IVTON (see Section 2.4.1.2). Distortion parameters for the

Cl containing samples are not plotted because the *z* coordinate of the anion differs between the apatite minerals, *i.e.* in fluorapatite it lies on the mirror plane (0,0,¼), in hydroxylapatite it is slightly offset from the mirror plane and in chlorapatite it is almost halfway between the mirror planes (Hughes & Rakovan 2002). The difference in anion positions makes it impossible to make a direct comparison of the distortion of the *Ca* polyhedra between members with different anion composition. The distortion of the *Ca1* polyhedra increases with increasing REE content, whereas both volume distortion and asphericity decreases with increasing REE content for the *Ca2* polyhedra.

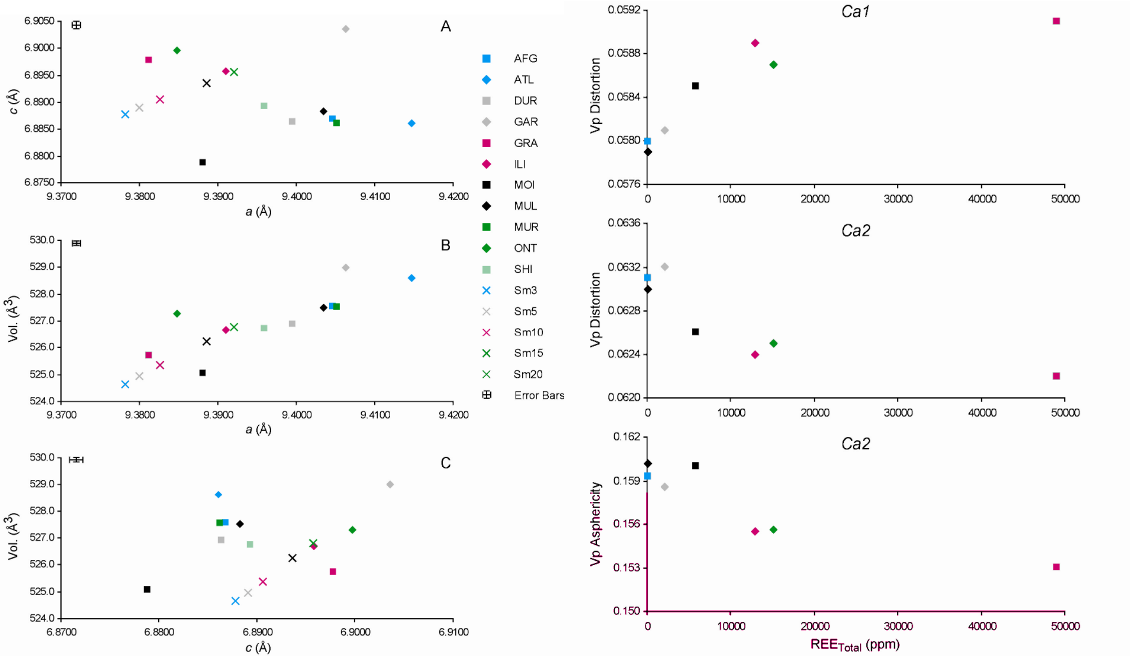

FIGURE 4.25: *Unit cell parameters of natural and synthetic apatite (A-C). The error bars are based on ILI, which has the largest errors. Figures to the right are selected distortion parameters of the* Ca1 *and* Ca2 *polyhedra calculated with IVTON as a function of REE content.*

4.4 Discussion

4.4.1 XRD

The continuous increase in unit cell parameters with increasing dopant level for the synthetic samples is expected as Na is significantly larger and Sm slightly smaller than Ca (Shannon 1976). Both natural and synthetic apatites show a strong correlation between increasing unit cell volume and increasing *a* axis, whereas correlations involving the *c* axis differ between natural and synthetic apatites. Such differences imply that Na and REE have a big structural effect in the **a** direction, but less so in the **c** direction. Consequently, the *c* axis effect on the volume is controlled by other element substitutions, *e.g.* Si substituting for P or the presence of divalent elements like Mn^{2+} or Sr^{2+}. The structural difference between natural and synthetic apatites implies that luminescence information decoded from synthetic apatites may not be applied directly to interpret luminescence spectra of natural samples.

The unit cell parameters for some samples plot outside the general trends, for example MOI has the smallest, and GAR the longest *c* axis. From the trace element content of these two samples (Table 1.4), GAR has the highest Sr and MOI the largest Mn content. The difference in ionic radius between the atoms can explain the changes in *c* axis as Ca^{2+} is 1.06, Mn^{2+} is 0.90 and Sr^{2+} is 1.21 Å in a seven-fold coordination (Shannon 1976).

The changes in distortion parameters of the *Ca* polyhedra with increasing REE content occurs rapidly with small concentrations of REE. However, if the incorporation of REE continues, the structure reaches a steady state, where further increase in REE has little effect. Similar behaviour has also been described for leucophanite (Friis *et al.* 2007a).

4.4.2 Eu^{3+}

Both PL and IL efficiently excite Eu in the apatite structure (Figs. 4.1 and 4.4). However, concentration and temperature dependencies are observed. A broad emission ~450 nm is ascribed to Eu^{2+} emission and is only present at low temperature. Eu^{3+} has a relatively strong excitation band ~466 nm ($^7F_0 \rightarrow {}^5D_2$) and at higher temperatures, suggesting, that the energy from the Eu^{2+} is efficiently transferred to Eu^{3+}, rather than being emitted. At low temperature the lattice vibration decreases and radiationless energy transfer between the two Eu oxidation states is no longer efficient, resulting in the Eu^{2+} emission. Another possible origin of the emission could be an intrinsic defect, but as the emission is only observed in the Eu^{3+} doped sample, it is considered unlikely.

The broad excitation bands ~260 and 300 nm (Fig. 4.3) have previously been ascribed to a charge transfer band connected to *O4*, which is the only oxygen not bonded to a tetrahedral site (Jagannathan & Kottaisamy 1995; Marimuthu *et al.* 2001; Piriou *et al.* 2001; Li *et al.* 2006). The narrow line excitation bands can be ascribed to the following transitions in Eu^{3+}: $^7F_0 \rightarrow {}^5H_3$ (320 nm), $^7F_0 \rightarrow {}^5D_4$ (363 nm), $^7F_0 \rightarrow {}^5G_2$ (377 nm), $^7F_1 \rightarrow {}^5L_7$ (383 nm), $^7F_0 \rightarrow {}^5L_6$ (394 + 401 nm), $^7F_0 \rightarrow {}^5D_3$ (414 nm), $^7F_0 \rightarrow {}^5D_2$ (466 nm) and $^7F_0 \rightarrow {}^5D_1 + {}^7F_1 \rightarrow {}^5D_1$ (531 nm) (Babu *et al.* 2006; Li *et al.* 2006; Krebs & Brownstein 2007).

The presence of just one $^5D_0 \rightarrow {}^7F_0$ emission indicates Eu^{3+} in just one site. Hence, the presence of at least three emissions (Fig. 4.2) indicates Eu^{3+} in different sites at low dopant level, which has been described previously (*e.g.* Gaft *et al.* 1997; Ternane *et al.* 1999). The weak splitting of the 572 nm emission suggests that four sites are present, which has also been observed by Piriou *et al.* (2001) for $Na_2Pb_8(PO_4)_6{:}Eu^{3+}$. Based on site-selective excitation and time-resolved PL, Gaft *et al.* (1997) ascribed two of the sites found to Eu^{3+} in the *Ca2* site and one to Eu^{3+} in *Ca1*.

The $^5D_0 \rightarrow {}^7F_2$ transition is an electric-dipole transition whereas the $^5D_0 \rightarrow {}^7F_1$ transition is a magnetic-dipole transition making the former strongly and the latter weakly sensitive to local symmetry. The intensity ratio (*R*) between these transitions has been proposed as an estimate for relative site distribution of non-symmetrical equivalent sites (Mai *et al.* 2006; Jayasundera *et al.* 2007).

Table 4.1. *The intensity ratio (*R*) defined as I_{589}/I_{614} as a function of excitation and composition*

	EX = 300 nm	EX = 363 nm	EX = 394 nm	EX = 464 nm
FAPEu3	0.73	0.20	0.92	0.22
FAPEu20	0.20	0.92	0.22	0.92

Table 4.1 shows that using the intensity ratio (*R*) between the J = 1 and 2 is highly dependent on the excitation. Two processes influence *R*. First, the $^5D_0 \rightarrow {}^7F_2$ transition probability decreases with increasing symmetry, which means *R* should be smaller for Eu^{3+} in the *Ca2 site* than for Eu^{3+} in the *Ca1* site, as *Ca1* has the higher symmetry. Hence, *R* is a probe of the distribution of Eu over the *Ca1* and *Ca2* sites.

For FAPEu3 with 394 nm excitation *R* is ~1, suggesting Eu is equally distributed between the two *Ca* sites. Increased Eu^{3+} content reduces *R*, implying the majority of Eu is occupying *Ca2*.

Second, values of *R* are inconsistent between different excitation wavelengths (Table 4.1). This is because different excitation wavelengths preferentially excite Eu in one site or the other; 363 and 464 nm excitations are site-selective, 300 nm excites both but with a preference for one and 394 nm gives site-independent excitation. For example, Li *et al.* (2006) found that 464 nm excitation specifically excited Eu^{3+} in the *Sr(I)* site in $Sr_2La_8(GeO_4)O_2$:Eu^{3+}, which is equivalent to the *Ca1* site in fluorapatite and supports the finding of Gaft *et al.* (1997). Determining which site is accessed by the different PL excitation energies is not trivial.

The crystal structural analyses of the 11 natural apatites in this study and 14 natural and synthetic apatites from the literature reveal that the average polyhedra volume sphericity of the *Ca1* and *Ca2* sites are 0.78 and 0.85, respectively (Mayer & Cohen 1983; Hughes *et al.* 1991b; Fleet & Pan 1995, 1997; Toumi *et al.* 2000). The higher sphericity of *Ca2* compared to *Ca1* may mimic a symmetry environment closer to that with an inversion centre. The change in *R* with increasing Eu^{3+} content is a result of multiple effects taking place in the structure. First, based on single-crystal XRD, Mayer & Cohen (1983) found the composition of the *Ca1* site to be ($Na_{0.50}Ca_{0.49}Eu_{0.01}$) and *Ca2* ($Ca_{0.73}Eu_{0.27}$), indicating that Eu is present in both sites, but preferentially enters *Ca2*. Na preferentially enters *Ca1*, which may also influence the coordination polyhedron. Second, Fig. 4.25 shows increasing deformation of the *Ca1* site with increasing REE content, whereas it decreases for the *Ca2* site. This change in *Ca2* symmetry will especially influence the $^5D_0 \rightarrow {}^7F_2$ transition. Third, Figs. 4.1 and 4.3 show that the site-selective excitation by 464 nm is only apparent at low concentration, suggesting that increased concentration desensitises site-selectiveness, therefore reflecting a significant modification of the electronic structure of the material. All of the analyses above assume that Eu^{3+} approximates to a ‘free ion’, in which intra-ion cascades are the same in the solid as they would be in an isolated ion. Although the free ion model is useful in interpreting the gross behaviour of lanthanide ions in solids, it assumes that interaction between ions (clustering) and between the ion and the lattice are negligible. Neither assumption may be fully true and the degree to which the system can be modelled as a free ion will change as function of the solid (*i.e.* crystal structure) and concentration in a manner that will be difficult to predict.

The combined observation from the luminescence and the structure analyses are consistent with a model whereby at low concentration, luminescence from Eu on *Ca1* is important and, as concentration increases, Eu^{3+} then preferentially enters *Ca2*. However, the use of luminescence as a reliable structural probe is hampered by the changing site-selectiveness of each excitation wavelength as a function of composition. Different responses could either be true changes in the distribution of Eu across the sites, a reflection of changing site-selectiveness (caused by subtle structural changes) or a complex response of both. Therefore, increased structural changes and/or cluster effects makes it difficult to use luminescence as a reliable structural probe.

4.4.3 Dy^{3+}

The four main emission bands observed in Fig. 4.5 can be ascribed to the following transitions in Dy^{3+} from the excited state ($^4F_{9/2}$) → $^6H_{15/2}$ (480 nm), $^6H_{13/2}$ (580 nm), $^6H_{11/2}$ + $^6F_{11/2}$ (666 nm) and $^6H_{9/2}$ (765 nm). The emissions ~845 and 966 nm observed with IL (Fig. 4.6) cannot be ascribed to transitions, but Baumer *et al.* (1997) described an emission at 835 nm in a cathodoluminescence study of synthetic anhydrite doped with Dy^{3+} and Nasdala *et al.* (2004a) ascribed an emission at 833 nm to the $^4F_{9/2} \rightarrow {}^6H_{7/2}$ transition.

The main excitation bands can be ascribed to the following transitions from the ground state: $^6H_{15/3} \rightarrow {}^4K_{15/2}$ (326 nm), → $^4P_{7/2}$ or $^4M_{15/2}$ (352 nm), → $^4I_{11/2}$ (366 nm), → $^4M_{21/2}$ + $^4K_{17/2}$ + $^4M_{19/2}$ (390 nm), → $^4G_{11/2}$ (453 nm), → $^4I_{15/2}$ (475 nm) (Liu *et al.* 2005).

The fine structure of the Dy emissions is reduced with increasing Dy content (Fig. 4.5B). One change that influences the sharpness of the emission bands is the crystallinity or short-range order of the material, *i.e.* peak broadening occurs with decreasing crystallinity (Nasdala *et al.* 2004b). Decreasing crystallinity also causes

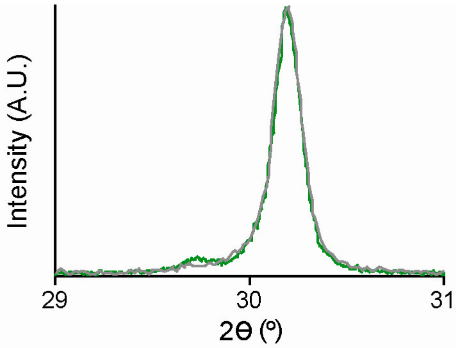

FIGURE 4.26: *X-ray diffraction peak of FAPDy15 (grey) superimposed onto FAPDy3 (green).*

broadening of x-ray diffraction peaks. However, Fig. 4.26 shows no difference in the shape of the diffraction peaks between FAPDy3 and FAPDy15, indicating that a change in crystallinity cannot explain the broadening of the Dy^{3+} emission with increased dopant-level. The change in luminescence, but not in XRD, indicates that the overall structure does not change with increasing dopant level but that REE clusters are created. Formation of clusters will have a big impact on luminescence as the distances between adjacent REE will be greatly reduced and hence the probability of interaction between them increased.

4.4.4 Sm^{3+}

The excitation bands in Fig. 4.9 can be ascribed to transitions from the ground state ($^6H_{5/2}$) to $^3H_{7/2}$ (346 nm), $^4F_{9/2}$ (363 nm), $^4D_{1/2}$ (376 nm), $^4H_{11/2}$ (392 nm), $^6P_{3/2}$ + $^4F_{7/2}$ (405 nm), $^4M_{19/2}$ + $^6P_{5/2}$ + $^4P_{5/2}$ (411, 415, 418, 424 nm), $^4F_{9/2}$ + $^4M_{17/2}$ (464, 469 nm), $^4I_{13/2}$ +$^4I_{11/2}$ (474, 479 nm), $^4I_{9/2}$ + $^4M_{15/2}$ (493 nm) (Jayasankar & Babu 2000; Kodaira *et al.* 2004; Liu *et al.* 2005; Rao *et al.* 2007). For the series of excitation bands around 415 and 470 nm, a number of transitions are possible and only a few are listed above. The broad excitation band ~266 nm has been ascribed to direct excitation of Sm^{3+} (Annapurna *et al.* 2003) or charge transfer band (Kodaira *et al.* 2004), whereas Rao *et al.* (2007) do not assign the excitation band.

The emissions observed in Figs. 4.8 and 4.10 correspond to transitions from the excited $^4G_{5/2}$ state to $^6H_{5/2}$ (~565 nm), $^6H_{7/2}$ (~600 nm), $^6H_{9/2}$ (~650 nm), $^6H_{11/2}$ (~705 nm), $^6H_{13/2}$ (~705 nm) and $^6H_{15/2}$ + $^6F_{5/2}$ (~900 nm) (Jayasankar & Babu 2000; Wells & Reeves 2000; Annapurna *et al.* 2003; Kodaira *et al.* 2004; Liu *et al.* 2005; Rao *et al.* 2007; Sun *et al.* 2007).

The 598/607 nm emissions are mixed magnetic and electronic dipole, where the latter dominates and the 644/658.5 nm emissions are pure electric dipole (Annapurna *et al.* 2003). The split of the emissions into two different peaks suggests that Sm^{3+} is present in both *Ca* sites. Since electric dipoles emissions are more likely at low symmetry Reisfeld *et al.* (1996) ascribed the 607 and 654 nm emissions to Sm^{3+} in *Ca2*. The emission spectrum under 260 nm excitation only excites those emissions indicating that it is site-selective. However, as the Sm concentration increases, the intensity of the 260 nm excitation band and the 607 + 658.5 nm emissions decrease.

Fleet & Pan (1995) argued that in natural fluorapatite Sm^{3+} is better accommodated in *Ca1* than in *Ca2*. However, Toumi *et al.* (2000) found that the majority of Sm^{3+} in $Ca_6Sm_2Na_2(PO_4)_6F_2$ is in *Ca2*. This, combined with the change in emission with increasing dopant level, suggests that Sm^{3+} at low concentrations occupies *Ca1*, but as the concentration increases the majority of samarium occupies *Ca2*. This contradicts Reisfeld *et al.* (1996), but as the electron dipole transition is hypersensitive to site-symmetry, it is possible that the difference expresses changes in the distortion of the Ca polyhedra with increasing REE content (Fig. 4.25).

4.4.5 Ho^{3+} and Er^{3+}

Both elements are luminescent under IL but not in PL. The broad emission bands found in both samples with low dopant levels are ascribed to intrinsic defects in the fluorapatite structure and are only visible in these samples as the REE^{3+} related luminescence is very weak. The major emission bands in Ho can be ascribed to: $^3H_6 \rightarrow {}^5I_8$ (358 nm), $^5G_5 \rightarrow {}^5I_8$ (410 nm), $^5F_3 \rightarrow {}^5I_8$ (487 nm), $^5F_4/^5S_2 \rightarrow {}^5I_8$ (544 nm), $^5F_5 \rightarrow {}^5I_8$ (659 nm), $^5F_4 \rightarrow {}^5I_7$ (753 nm) and in Er to: $^2P_{3/2} \rightarrow {}^4I_{13/2}$ (402 nm), $^2P_{3/2} \rightarrow {}^4I_{11/2}$ (471 nm), $^2D_{7/2} \rightarrow {}^4F_{9/2}$ (529 nm), $^2H_{9/2} \rightarrow {}^4F_{13/2}$ or $^4S_{3/2} \rightarrow {}^4I_{15/2}$ (551 nm), $^4F_{3/2} \rightarrow {}^4F_{13/2}$ (617 nm), $^2F_{9/2} \rightarrow {}^4I_{15/2}$ (659 nm), $^4I_{9/2} \rightarrow {}^4I_{15/2}$ (808 nm), $^4S_{3/2} \rightarrow {}^4I_{13/2}$ (858 nm) $^4I_{11/2} \rightarrow {}^4I_{15/2}$ (978 nm) (Karali *et al.* 2000; Karmakar 2005; Liu *et al.* 2005; Moizan *et al.* 2008)

The strong absorption band ~521 nm for FAPEr10 (Fig. 4.13) arises from the transition from the ground state $^4I_{15/2} \rightarrow {}^2H_{11/2}$ in Er^{3+}. The presence of the strong absorption band indicates that the energy deposited during PL does reach and excite Er^{3+}. However, the lack of luminescence suggests that the energy is either transferred to the ground state in a radiationless manner or to low energy levels prior to emission in the infrared region outside the PL detector range. The latter explanation is more likely as IL revealed strong emission bands in the IR region for Er^{3+} (Fig. 4.12).

4.4.6 Sm^{3+} and Dy^{3+} Co-doped

Both PL and IL experiments show no indication of energy transfer between Dy^{3+} and Sm^{3+} at room temperature or 77 K (Figs. 4.14, 4.15 and 4.18), *e.g.* excitation directly of Dy^{3+} results only in Dy^{3+} emissions. Furthermore, when the Dy content is doubled, so does the intensity of the Dy emissions, whereas no difference is observed for the Sm emissions (Fig. 4.15). This effect further stresses the lack of interaction between Dy and Sm.

The broad, weak emission between 370 and 540 nm is only present at 77 K and is strongest in the sample with the highest dopant level. This suggests that the emission is related to a structural defect caused by high REE content. It is possible that the chemical reaction is not ideal at high concentrations or that other charge balance mechanisms occur, especially at higher temperatures *e.g.* O^{2-} for F^{1-}, which would explain the defect emission. Since the region of the broad emission overlaps with several Dy^{3+} and Sm^{3+} excitation bands (Figs. 4.17 and 4.18) it is plausible that at RT the defect emission is simply activating the REE emissions, and hence is absent.

During ion implantation permanent defects (*e.g.* F-centres) are generated especially at the end of the ion track. Often emission intensity decreases during luminescence experiments (*e.g.* Barbarand & Pagel 2001; Brooks *et al.* 2002; Götze 2002; Kempe & Götze 2002; Finch *et al.* 2004; Götze *et al.* 2005; Friis *et al.* 2007b). Fig. 4.16 shows that the ion implantation reduces the intensity of the emissions, and that the intensity reduction is larger for Sm than for Dy emissions. One explanation for the observed intensity change is that the formed F-centres open pathways for energy to be transferred from Sm to Dy. Another possibility is that the F-centres form new pathways from the conduction band that favour cascade to Dy^{3+} rather than Sm^{3+}.

The fact that Sm and Dy show different degrees of intensity loss during implantation questions the validity of using luminescence as a qualitative tool for determining trace element concentrations (*e.g.* Homman *et al.* 1994; Habermann *et al.* 1998, 1999; Gillhaus *et al.* 2001; Habermann 2002). Another problem when attempting to apply luminescence intensity as a measure for trace element concentration is that self-quenching becomes a problem at high concentrations. However, as Figure 4.27 shows, the relationship between concentration and intensity differs between different REE, even in the same host, *i.e.* concentration quenching occurs at very different dopant levels depending on REE. Dy^{3+} has an optimum dopant level less than 0.15 *apfu* and, based on the results from the co-doped material, the optimum level is between 0.05 and 0.15 *apfu*. In contrast to Dy^{3+}, the ideal dopant level for Sm^{3+} is between 0.25 and 0.50 *apfu*, whereas for Eu^{3+} it is between 0.75 and 1.00 *apfu*. However, most studies seek to develop luminescent materials with high efficiency at ppm or ppb concentrations of the activator. Therefore, concentrations are likely to be far below the limits of self-quenching and the lanthanide centres may be considered as isolated and luminescence intensity linearly dependent on concentration. Nevertheless, the greater realisation and understanding of the relationships between luminescence intensity and concentration makes it increasingly unlikely that luminescence will ever be developed as a compositional probe. Furthermore, secondary ion mass spectrometry (SIMS), synchrotron x-ray fluorescence (SXRF) and laser-ablation inductively coupled plasma mass spectrometry (LA-ICPMS) all have ppm to ppb limits of detection and suffer from fewer complex matrix effects.

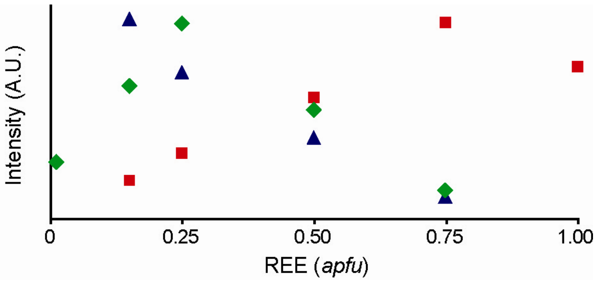

FIGURE 4.27: *Intensity of PL versus dopant level for Dy^{3+} (blue; EX/EM 352/577 nm), Eu^{3+} (red; EX/EM 394/576 nm) and Sm^{3+} (green; EX/EM 405/598 nm) in synthetic fluorapatite.*

4.4.7 Natural Apatites

The emissions observed for IL, CL and RL (Figs. 4.19 and 4.20) can be ascribed to different REE based on comparison with the synthetic samples. However, some emissions like those ~313, 548 nm and the IR emissions can be ascribed to Gd^{3+}, Tb^{3+} or Ho^{3+} and Nd^{3+}, respectively, based on previous studies of natural apatite (Roeder *et al.* 1987; Homman *et al.* 1994; Mitchell *et al.* 1997; Barbarand &

Pagel 2001; Gorobets & Rogojine 2002; Kempe & Götze 2002). The two broad emissions ~360 and ~450 nm have been ascribed to Ce^{3+} and Eu^{2+}, respectively, and generally the spectra are similar to spectra in these publications. However, the presence of intrinsic defects cannot be ruled out.

An interesting result is the difference in relative intensity between the ~360 and ~450 nm emission in RL and CL, where the former dominates in CL but the latter in RL. One explanation for this difference is that in CL only the surface of the sample is excited whereas in RL the whole sample is excited. In accordance with Fig. 1.2 the 360 nm emission will not be significantly absorbed by the sample in CL, whereas in RL more of the 360 nm emission relative to the 450 nm emission will be absorbed by the sample. Hence, the 450 nm emission will appear more intense in RL than in CL for a similar chemistry. Another possible explanation is connected with the ability of x-rays to change the oxidation state of some $REE^{3+} \rightarrow REE^{2+}$ (*e.g.* Lakshmanan & Tomita 1999; Park *et al.* 2006; Peng & Hong 2007; and references therein). If x-rays during RL reduce $Eu^{3+} \rightarrow Eu^{2+}$, it would explain the more intense RL of the 450 nm emission than CL. However, if Eu^{3+} is being reduced, a reduction of $Sm^{3+} \rightarrow Sm^{2+}$ may also be expected, but no observed differences between the CL and RL suggest the presence of Sm^{2+}.

The PL emissions are generally weak (Figs. 4.22 and 4.24) and excitation of five different samples with 405 nm only shows emission relating to Sm^{3+} indicating that little energy from Sm^{3+} is transferred to other activators. The excitation spectra for different samples reveal typical excitation bands for Sm^{3+} (Fig. 4.23). However, a broad excitation band ~310 nm indicates the presence of a structurally-related excitation band. Excitation using the broad UV excitation band reveals emissions related to several REE for DUR, where a broad emission ~565 nm is observed for MOI. Broad emission in apatite bands around 565 nm have previously been ascribed to Mn^{2+} (*e.g.* Barbarand & Pagel 2001; Kempe & Götze 2002; Waychunas 2002), which is further supported by the fact that MOI has the highest Mn content (Table 1.4).

The continuous reduction in the luminescence intensity of ILI (Fig. 4.21) during alignment is similar to Optically Stimulated Luminescence (OSL), which is used for dating young sediments. The method is based on the formation of traps within the band-gap, caused by radiation damage from the surrounding rocks/sediments. The number of defects relates to the integrated radiation dose of the material, which is in turn dependent on the age of the material, *i.e.* high luminescence intensity equals old sediments. The number of traps present in the band-gap can be estimated by the number of decay curves, or lifetimes of the emissions. The modelling of at least two components with different life-times in ILI (Section 4.3.7.2) indicates the presence of at least two traps in the band gap. However, the apatite samples have been exposed to sunlight, *i.e.* any OSL signal would have been bleached prior to my luminescence studies.

It is more likely that during continuous UV irradiation the sample is being electronically modified, either in form of exciton or electron-hole recombination. Another possibility is that an electron is changing state and creates an effect similar to the colour change of hackmanite. The observed reduction in intensity during PL could explain why PL of apatite often is weak, whereas high-energy excitation like CL is strong. The high-energy continuously populates the traps or creates the special electron states, whereas PL only has sufficient energy to change it back or create the recombination. However, intriguing as this effect is, it will be very time-consuming to fully characterise and is therefore beyond the scope of this thesis.

4.5 Conclusions

REE luminescence is not associated with valence electrons and therefore considered to be fully or only weakly linked with the host structure. However, the Ho and Er data, in which PL is absent, but luminescence is present with high-energy excitation, show that the host structure plays an important role in the generation of REE luminescence. Furthermore, this study has shown that different REE respond differently to sample degeneration or defect formation during irradiation. For example, if Sm is more strongly coupled to the host than Dy, then the intensity of Sm emissions will be reduced more than Dy emissions by modifications to the lattice.

The emission and excitation spectra for the co-doped sample show that when an excitation wavelength specific for an energy transition in one REE is chosen, only emissions from that REE are observed. This indicates that very little energy is transferred between the two activators. The synthetic sample only contained two different activators, but the same is observed for the natural samples where only Sm^{3+} emissions are observed after specific excitation of a Sm^{3+} absorption band. However, when the natural samples are excited with wavelengths in the broad UV excitation band, more emissions appear and the resulting spectrum resemble that acquired with high-energy excitations. Broad excitation bands are coupled to the structure, either as an anion charge transfer band (as observed for some single doped REE samples) or related to structural defects.

At low dopant levels both Eu and Sm show site-selective excitation and fine structures. At high dopant levels, the fine emission structures of the Dy doped sample disappear and for the Eu doped sample the site-selective excitation and the ability to define the number of sites based on the J = 0 transition ceases. The single-crystal analyses of natural apatites show that increasing REE content changes the distortion of the two *Ca* polyhedra and powder XRD shows how the crystallinity of the synthetic material does not change with increasing dopant level. Most likely, the changes in the distortion of the *Ca* polyhedra modify the site-symmetry, which is reflected in the hypersensitive electronic dipole transitions. Furthermore, the powder XRD of the Dy doped sample indicates that clusters are formed at high dopant levels, which also greatly affect the interpretation of the luminescence for estimating site population in non-symmetric equivalent sites.

In RL the broad emission ~450 nm is stronger than the ~360 nm emission, whereas in CL the latter dominates. If the 450 nm emission is ascribed to Eu^{2+} it is possible that during the RL experiment Eu^{3+} is being reduced to Eu^{2+} by x-rays. Alternatively, the difference can be explained by a combination of CL exciting only the surface region, whereas RL excites the entire sample. As fluorapatite absorbs UV then all of the 450 nm, emission generated deep inside the sample will pass through and reach the detector, whereas a large proportion of the UV (360 nm) generated deep in the sample will be absorbed and not escape the sample. Hence, in RL the 360 nm appears suppressed compared to the 450 nm emission, but with the corresponding CL, the absorption of the UV signal is minimal.

The ideal dopant level for Dy^{3+}, Sm^{3+} and Eu^{3+} also varies significantly from 0.05 - 0.15 *apfu* for Dy^{3+} to 0.75 - 1.00 *apfu* for Eu^{3+}. The fact that the ideal dopant level varies for different REE, combined with the REE dependent intensity difference through radiation damage, demonstrates that luminescence cannot be used to determine trace element concentration. Such compositional analysis may be possible for well-characterised samples after major testing of synthetic material with different dopant levels, and then most likely only within a narrow compositional area, but not for natural samples where several emission bands overlap. Luminescence is unlikely to compete routinely with other analytical methods with ppm-ppb limits of detection and micron-scale spatial resolution.

Chapter 5

Multiple Luminescent Spectroscopy of the Two Related Minerals Leucophanite and Meliphanite

Multiple Luminescent Spectroscopy of the Two Related Minerals Leucophanite and Meliphanite

5.1 Introduction

Leucophanite, ideally $NaCaBeSi_2O_6F$ and meliphanite, ideally $Ca_4(Na,Ca)_4Be_4AlSi_7O_{24}(F,O)_4$ are two structurally and chemically related minerals belonging to the melilite group. For details on the structural and chemical relationship between the two minerals see Grice & Hawthorne (1989, 2002) and Friis *et al.* (2007a). The luminescence properties of the two minerals are very different despite chemical and structural similarities. Leucophanite is a very efficient luminescent mineral under all types of excitation (Gorobets & Prokofiev 1981; Prokofiev *et al.* 1982; Gorobets & Rogojine 2002; Gaft *et al.* 2005; Friis *et al.* 2007b), whereas to my knowledge, only photo- and radioluminescence spectra have been published for meliphanite, and only the latter technique resulted in emission bands that could be interpreted (Gorobets & Rogojine 2002).

This study will investigate the luminescent properties of leucophanite and meliphanite by using photoluminescence (PL), cathodoluminescence (CL), radioluminescence (RL) and ionoluminescence (IL). It will compare and contrast the luminescence for these two related minerals and use their behaviour to understand more fully the complex relationships between composition, structure and luminescence in this important system. Furthermore, changes in luminescence caused by the choice of excitation type will be explored.

5.2 Materials and Methods

Three samples of leucophanite (Leuco5, Leuco8 and Leuco9) from various localities have been investigated. For details on the samples ionoluminescence and their trace element compositions see Friis *et al.* (2007a,b). The IL of Leuco8 and 9 is dominated by a broad emission centred around 600 nm ascribed to Mn^{2+}, whereas Leuco5 has a series of line emissions in this region ascribed to REE^{3+}. All samples have a broad emission ~380 nm ascribed to a structural defect, which dominates the Leuco5 emission. Chemically Leuco9 has the lowest and Leuco5 the highest trace element content. For both Leuco8 and 9, cleavage fragments were analysed, but for Leuco5, in addition to cleavage fragments (Leuco5C), a very fine powder (Leuco5P) was also analysed. Eight samples of meliphanite from different localities within the Permian alkaline area of the Langesundsfjord in Norway were investigated (see Table 1.5) using a standard UV-lamp. Only a few were luminescent to the naked eye. Three samples were chosen for detailed study based on their luminescence, chemical and structural data (see Section 5.3.2.1). ARS forms thin, strong, yellow transparent cleavage fragments up to 4 cm in size associated with feldspar and aegirine. HAK occurs as almost colourless platy cleavage groups in feldspar. OST occurs as up to 15 cm large groups of thick, platy rosettes in feldspar often associated with a gadolinite-group mineral.

The luminescence spectroscopies (PL, CL, RL and IL) applied are described in Section 2.1. The instruments used for determining major and trace element content are described in Sections 2.2.1 and 2.2.2 and the structural analyses in Section 2.4.2.1. The photomicrograph setup is described in Section 2.3.3.

5.3 Results

5.3.1 Leucophanite

5.3.1.1 UV to Blue Region

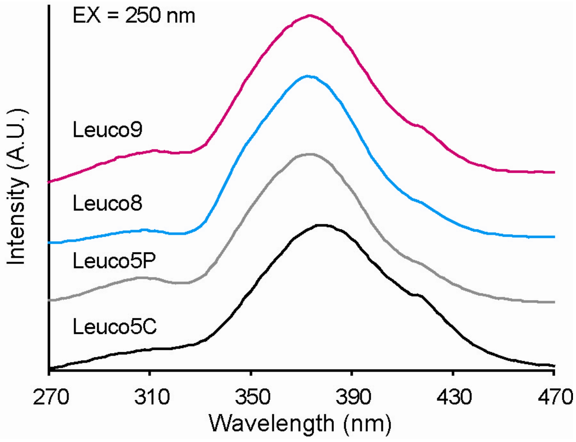

FIGURE 5.1: *PL Emission spectrum of the UV-Blue region of leucophanite under 250 nm excitation.*

Figure 5.1 shows a strong UV-blue emission centred at 374 nm for all samples except Leuco5C, in which the peak is centred at 380 nm. Another weak, broad emission is present ~308 nm and a small shoulder indicates a narrow emission ~418 nm. The position of the 418 nm emission is consistent for all samples confirming that the shift to 380 nm is beyond instrumental error.

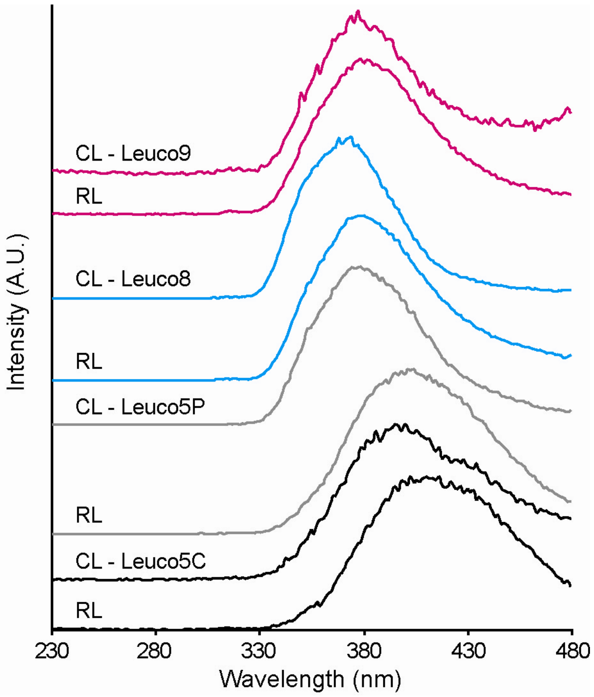

FIGURE 5.2: *CL and RL of the UV-Blue emission in leucophanite.*

Figure 5.2 shows that the emission band shifts towards lower energy when excited with x-rays compared to electrons. The shift is strongly sample dependent, with the smallest shift in Leuco9 and the largest in Leuco5P, *i.e.* the shift increases with increasing trace element concentration. The shift is smaller for Leuco5C than for Leuco5P, but the emission is at lower energy for the cleavage fragment than for the powder sample in both CL and RL. In CL of Leuco8 and Leuco5P the broad emission has a shoulder on the high-energy side and the RL of Leuco5 indicates the presence of another emission centre ~425 nm. The positions observed for the broad emission under different excitations are summarised in Table 5.1.

TABLE 5.1. *Position (nm) of the broad UV-blue emission band in leucophanite with different excitations*

	PL	CL	RL
Leuco9	374	378	381
Leuco8	374	371	380
Leuco5P	374	380	404
Leuco5C	380	395	416

5.3.1.2 Visible to IR Region

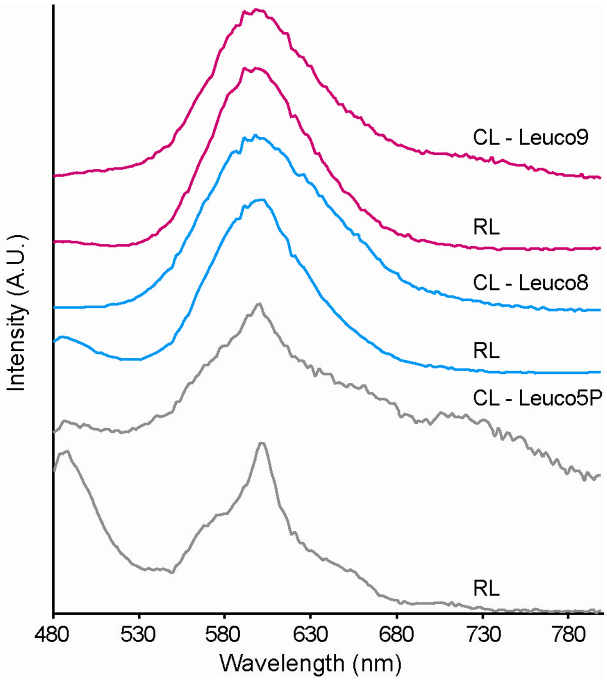

FIGURE 5.3: *CL and RL spectra of leucophanite.*

The CL and RL spectra of Leuco5P and Leuco5C do not differ in the visible region and therefore only data for Leuco5P are presented together with data for Leuco8 and Leuco9 in Figure 5.3. Both excitations result in a broad emission band centred ~602 nm for Leuco8 and 9. Both samples show a weak emission ~485 nm, which is only present under RL excitation. A weak emission ~485 nm is present in CL of Leuco5P and the broad emission ~602 is replaced by a narrower emission with a weak shoulder around 580 nm. With RL the 485 nm emission becomes almost as intense as the sharp 602 nm emission and the shoulder ~580 nm becomes more defined.

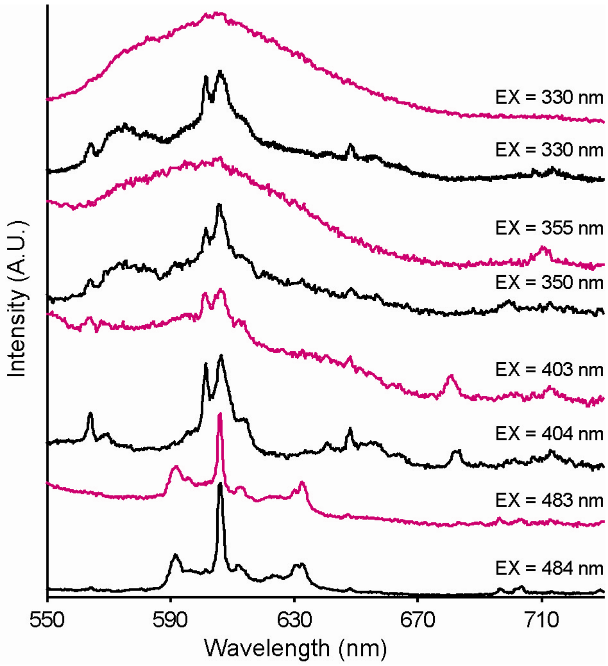

FIGURE 5.4: *PL emission of Leuco9 (pink) and Leuco5C (black) with different excitations.*

Under a range of excitations Leuco5C shows only line emissions, although ~580 nm the lines are merged giving the appearance of a broad emission (Fig. 5.4). Leuco9 is dominated by a broad emission ~602 nm under both 330 and 355 nm excitation (Fig. 5.4), similar to CL and RL (Fig. 5.3). The spectra for the two samples are similar under the same excitation, but a change in excitation results in different spectra. The following line emissions are identified: 564, 570, 580, 592, 596, 602, 606, 612, 623, 632, 641, 648, 656, 664, 683, 697, 699, 704, 707 and 713 nm. The 606 nm emission is dominant under all excitations.

The excitation spectra of selected emission bands in Leuco9 and 5C are presented in Fig. 5.5, revealing broad, weak excitation bands around 270-280 nm and at least two strong broad excitation bands between 330 and 355 nm. The broad excitation bands ~340 nm dominate, except for the excitation of the 606 nm emission in Leuco5C, where the 484 nm excitation dominates. The following line excitations are identified: 375, 404, 414, 420, 423, 442, 462, 466, 471, 484 and 487 nm. The intensity of the 330 and 404 nm excitation bands is the same for the 602 and 606 nm emissions. The excitation bands between 440 and 490 nm are more intense for the 606 nm than for the 602 nm emission.

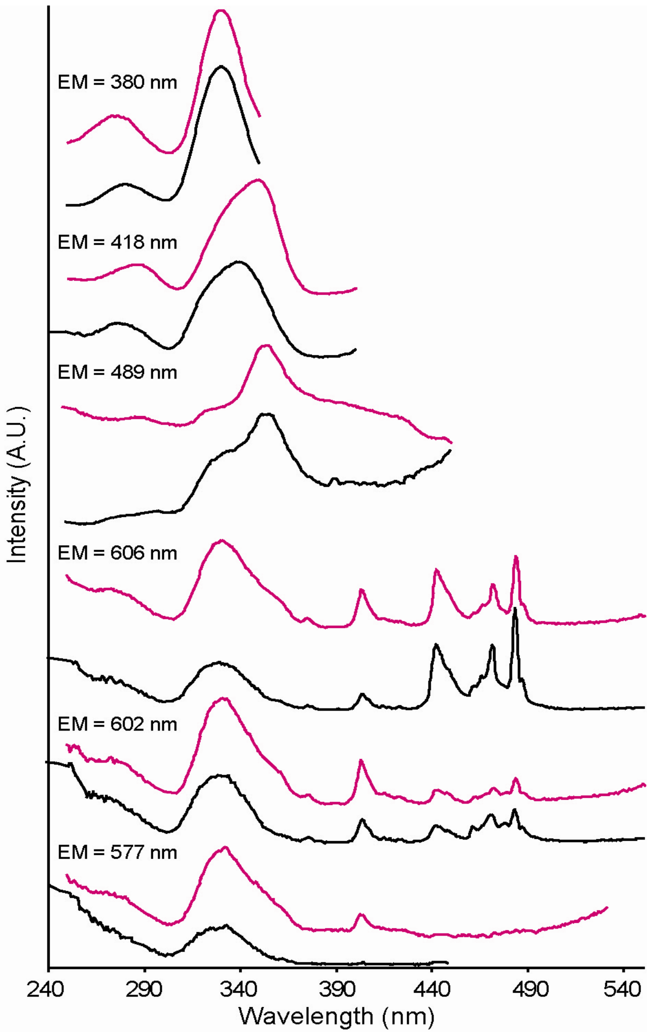

FIGURE 5.5: *Excitation spectra of selected emission bands in Leuco9 (pink) and Leuco5C (black).*

5.3.2 Meliphanite

5.3.2.1 Chemistry and Structure

The trace element concentrations for eight meliphanites are presented in Table 5.2.

TABLE 5.2. *Trace element concentration (ppm) of the analysed meliphanite samples*

	ARS	BJO	HAK	OST	SAR	STO	TEL	TRE
n	*5*	*6*	*6*	*5*	*5*	*5*	*5*	*5*
Mn	444	1916	3578	2194	643	463	1104	1745
Fe	1036	961	1433	1184	1158	1110	1216	1444
Zn	162	206	301	300	222	183	256	271
Sr	685	30	4	19	284	650	137	31
Y	44	1437	1116	1468	165	105	299	755
La	289	550	1085	522	329	305	540	572
Ce	844	1377	2215	1326	914	864	1135	1781
Pr	79	125	178	115	82	91	91	173
Nd	251	404	421	336	255	295	257	571
Sm	43	103	78	92	51	56	55	123
Eu	8	12	6	9	12	10	12	10
Gd	28	120	82	106	42	41	52	115
Tb	3	28	17	27	7	5	9	21
Dy	16	215	139	215	40	30	59	144
Ho	2	42	30	44	6	5	10	28
Er	4	114	95	123	15	9	24	71
Tm	0	14	14	15	2	1	3	9
Yb	1	74	90	80	7	4	12	43
Lu	0	6	9	7	1	0	1	4
Pb	5	7	15	9	6	5	9	9
Th	51	53	38	46	51	47	69	41
U	13	1	0	1	8	8	10	5

n - Number of analyses

The concentration of trace elements reveals two groups with ARS, SAR, STO and TEL having the lowest concentration of both di- and trivalent trace elements. The two groups also have different REE distributions. ARS has the lowest total trace element content, whereas HAK has the highest. In leucophanite, REE substitutes for Ca and the incorporation of REE is charge balanced by additional incorporation of Na and the formation of vacancies (Friis *et al.* 2007a).

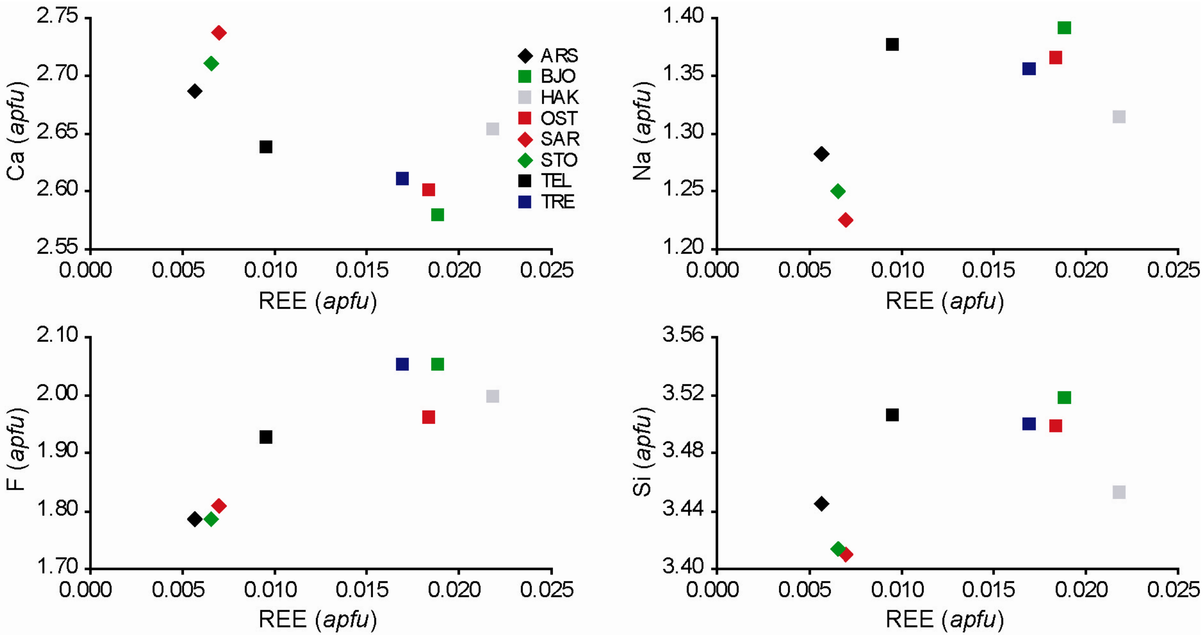

FIGURE 5.6: *Major vs. trace element (REE+Y) concentrations of the analysed meliphanites.* apfu *values are calculated on the basis of 14 anions. The errors on the major elements are between 0.01 and 0.07* apfu *and on the REE ~10%.*

Fig. 5.6 shows a general decrease in Ca content with increasing REE. The samples with high REE concentrations also have high Na and Si content, although no clear correlation is observed. However, fluorine shows a clear increase with increasing REE. These correlations indicate that meliphanite has a different mode of charge compensation than leucophanite. REE, especially the lighter REE, can substitute for Ca because their ionic radii are similar in an eightfold coordination, *e.g.* Ca (1.12 Å), La (1.300 Å), Gd (1.053 Å) and Yb (0.985 Å) (Shannon 1976). However, the slight difference in ionic size between the major elements in meliphanite and the trace elements being incorporated results in subtle structural changes. Figure 5.7 indicates that a good correlation exists between the different unit cell parameters, and also between the unit cell parameters and REE content. The unit cell volume and *c* decrease when *a* increases; where the decrease in *c* correlates with the increase in REE content. The samples HAK and STO only follow the trends of the other samples for *c vs.* REE, indicating that there is a reduction in the accuracy of the refinement of *a*, but the cause could not be identified.

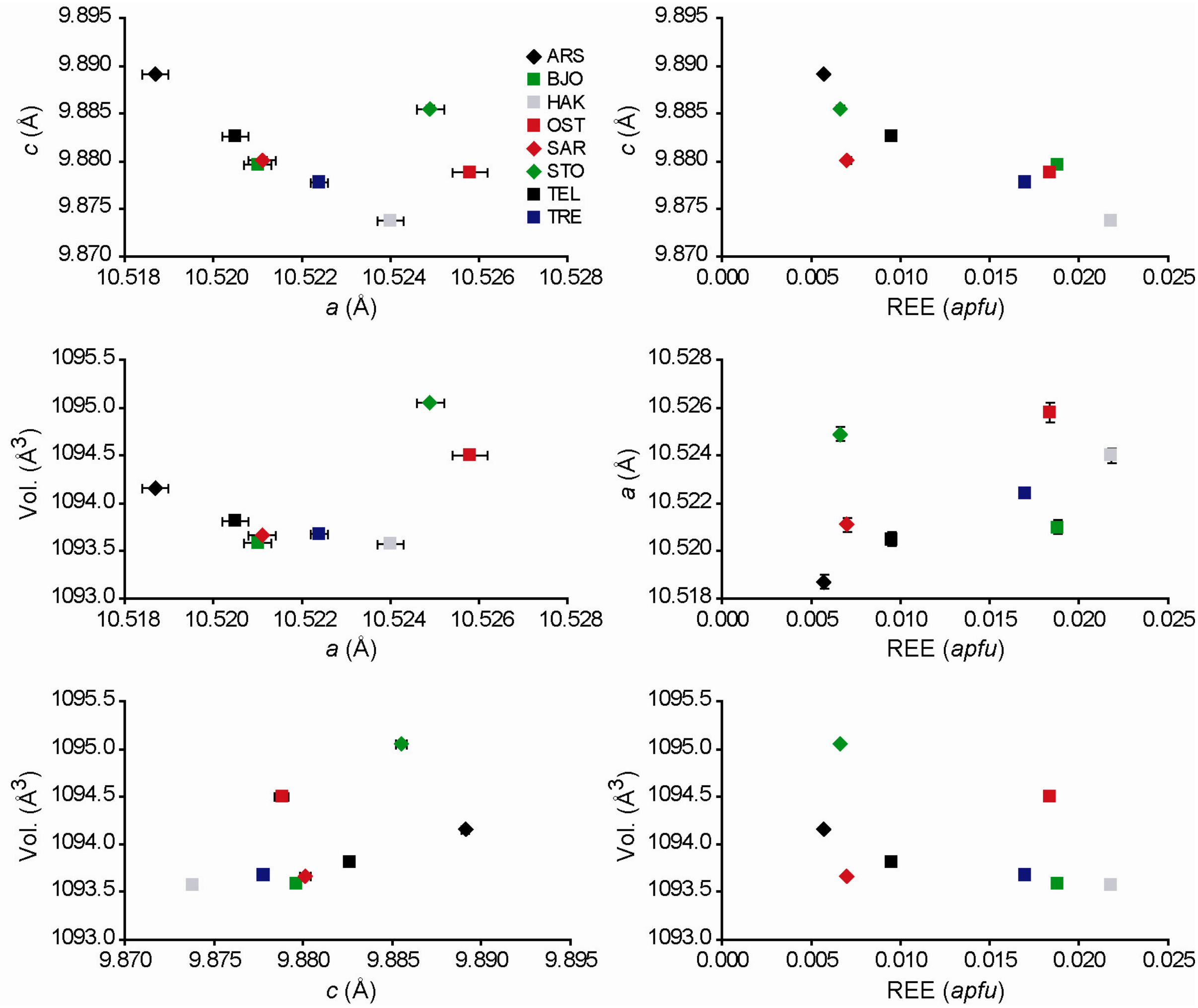

FIGURE 5.7: *Unit cell parameters based on powder XRD and the content of REE+Y from LA-ICPMS. The error bars are 1σ on the cell parameters and the error non the REE is ~10%.*

5.3.2.2 IL

The ionoluminescence spectra of the three meliphanites (Fig. 5.8A) consist of two broad emissions ~380 and 630 nm where the 380 nm emission has a shoulder around 350 nm and the 630 nm emission a shoulder ~580 nm. The relative intensity of the red and UV emissions changes so that HAK is dominated by the 630 nm emission, whereas ARS is dominated by the 380 nm emission. Line emissions are present at ~312, ~480, ~600 and ~880 nm. The detailed spectrum of OST (Fig. 5.8B) resolves the shoulder at 580 nm into a series of emissions at 566, 571 and 577 nm and emissions at 540, 601, 608, 755, 978, 998, 1048 and 1062 nm and at least six emission bands around 880 nm are observed.

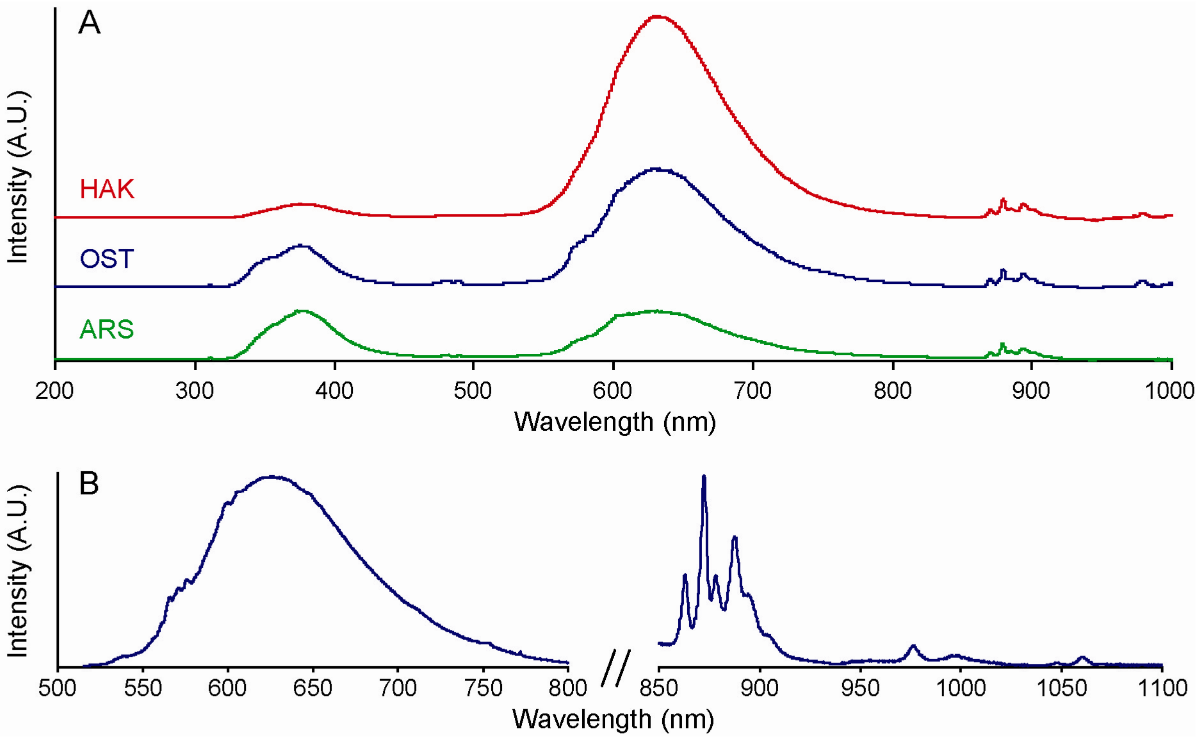

FIGURE 5.8: *Comparison of the IL of three meliphanites (A) and details of sample OST (B).*

5.3.2.3 CL

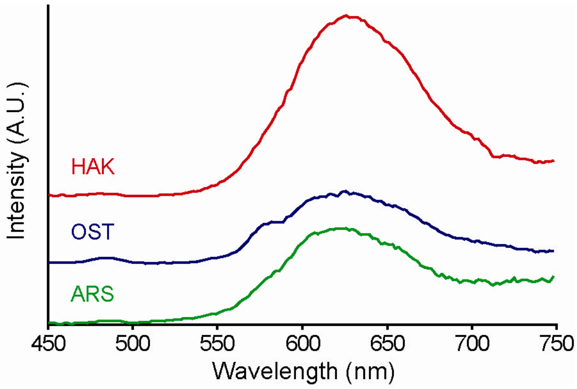

FIGURE 5.9: *CL spectra of three meliphanite samples.*

The CL spectra of three meliphanites are presented in Fig. 5.9 and are similar to the IL data. All spectra are dominated by a broad emission ~630 nm and the shoulder ~580 nm is particular well defined in OST. A weak emission ~480 nm is also present in all samples. Figure 5.10 demonstrates how the luminescence intensity decreases during exposure to the electron beam.

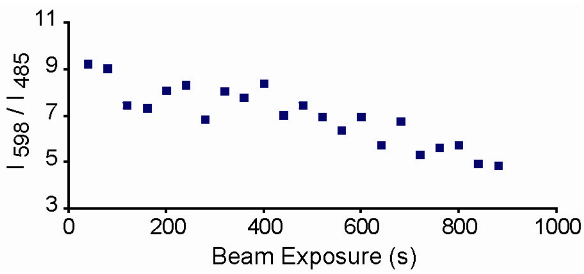

FIGURE 5.10: *Change in relative intensity of different emission bands during CL of OST.*

5.3.2.4 PL

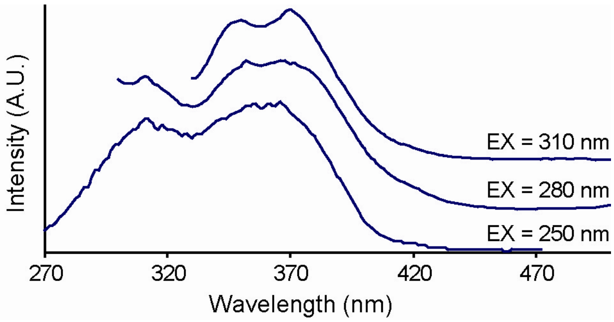

FIGURE 5.11: *PL of the UV-Blue region of OST under different excitations.*

From IL and CL it is found that sample OST displays the different luminescence emissions particularly well and therefore PL data for this sample only will be presented. The PL of OST (Fig. 5.11) shows broad emission bands in the UV-Blue region. A dip in intensity ~330 nm suggests the presence of more than one emission in the region centred ~350 and 370 nm, in accordance with the findings for leucophanite (Fig. 5.1). An additional narrow emission may be present ~312 nm. The PL of OST under four different excitations is presented in Figure 5.12. With both 338 and 349 nm excitation, the spectra have a broad emission around 630 nm and also a series of line emissions around 570 nm. With 404 and 484 nm excitation only line emissions are present and the series around 570 nm is no longer present. The following line emissions are identified: 563, 568, 572, 577, 582, 589, 594, 601, 605, 611, 628, 641, 644, 652, 659, 674, 683, 698 and 712 nm. Generally, the emission spectra resemble those of leucophanite (Fig. 5.4); the main difference being that in meliphanite the emissions ~570 nm are clearly seen as individual emission lines, whereas in leucophanite they merge into one broad band.

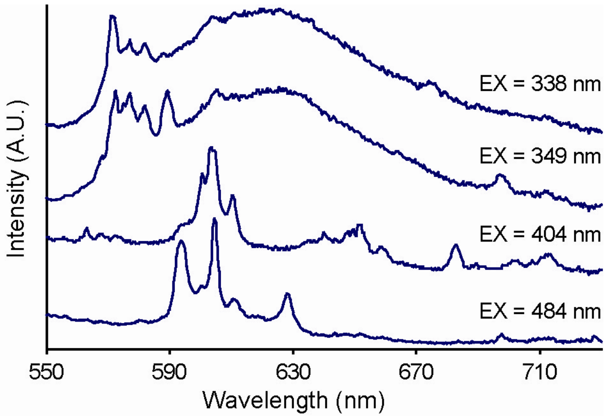

FIGURE 5.12: *PL of OST under different excitations.*

The excitation spectra of different emission bands in OST (Figure 5.13) are dominated by a broad excitation band varying in position between 330 and 338 nm for the 378 and 608 nm emissions, respectively. A weak, broad excitation band is present ~270 nm. The excitation spectra for the 571, 577 and 582 nm emissions are similar, but distinct from the excitation of the 601, 604 and 608 nm emissions. Line excitations for the former group are at 349, 365, 388, 428, 454, 468 and 474 nm, while the line bands in the latter group are at 375, 404, 415, 422, 445, 464, 471 and 484 nm.

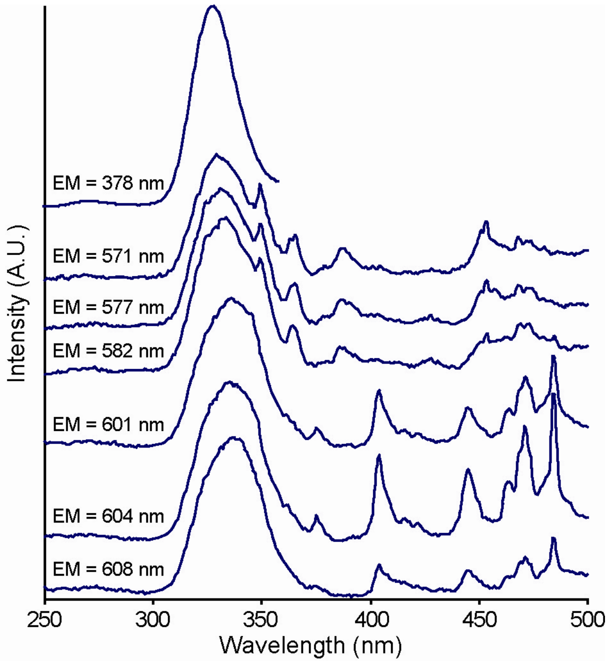

FIGURE 5.13: *Excitation spectra for different emission bands in OST.*

5.3.3 Low Temperature

The IL spectrum of meliphanite at 77 K shows no significant changes compared to that at room temperature.

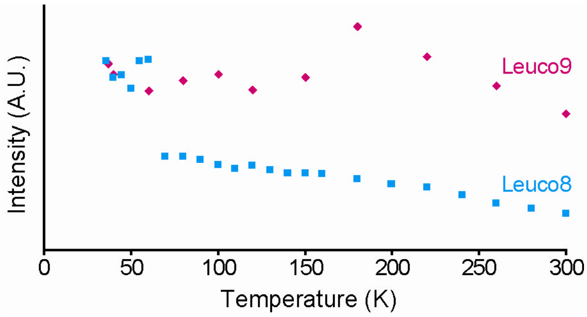

FIGURE 5.14: *IL intensity of the Mn^{2+} emission in leucophanite as a function of temperature.*

The intensity of the Mn^{2+} emission in leucophanite from the low temperature experiment reported by Friis *et al.* (2007b) is presented in Fig. 5.14. For Leuco8 the intensity decreases steadily from ~60 K until room temperature. The temperature profile for Leuco9 is less smooth and shows a sudden intensity increase between 160 and 180 K. Maghrabi *et al.* (2001) ascribed a sudden intensity increase at 175 K to the presence of Cl. Kurt *et al.* (2002) ascribed a similar intensity increase at 170 K to a phase transition from cubic to hexagonal ice in water that had been adsorbed onto the surface of the sample. The cause of the intensity jumps are explained as changes in stress within the lattice associated with these phase transitions, which will change the crystal-field effect and consequently the luminescence. Both Leuco8 and 9 were cleavage fragments that were treated and stored under the same conditions. Therefore, it is considered unlikely that only one sample would have adsorbed water.

5.4 Discussion

5.4.1 Meliphanite IL

The emission bands are similar to those found by Friis *et al.* (2007b) for leucophanite and can be assigned to Gd^{3+} (312 nm), a defect related to a tetrahedral site or exciton (380 nm), Dy^{3+} (480 and 580 nm), Sm^{3+} (601 and 606 nm), Mn^{2+} (630 nm) and Nd^{3+} (880 nm). Table 5.3 presents all the observed emission bands and suggests energy transitions. These data are consistent with the structural similarities between leucophanite and meliphanite.

TABLE 5.3. *Activators and possible energy transfer for IL in meliphanite*

Wavelength (nm)	Energy (eV)	Activator	Possible Transitions
312	3.97	Gd^{3+}	$^6P_{7/2} \rightarrow {}^8S_{7/2}$
380	3.26	Defect	
479 489	2.59 2.54	Dy^{3+}	$^4F_{9/2} \rightarrow {}^6H_{15/2}$
540	2.30	Tb^{3+} Ho^{3+}	$^5D_4 \rightarrow {}^7F_5$ $^5F_4/{}^5S_2 \rightarrow {}^5I_8$
566	2.19	Sm^{3+}	$^4G_{5/2} \rightarrow {}^6H_{5/2}$
571 577	2.17 2.15	Dy^{3+}	$^4F_{9/2} \rightarrow {}^6H_{13/2}$
601	2.06	Sm^{3+}	$^4G_{5/2} \rightarrow {}^6H_{5/2}$
608	2.04	Sm^{3+}	$^4G_{5/2} \rightarrow {}^6H_{5/2}$
630	1.97	Mn^{2+}	$^4T_1 \rightarrow {}^6A_1$
755	1.64	Dy^{3+} Ho^{3+}	$^4F_{9/2} \rightarrow {}^6H_{9/2}$
863-905	1.44-1.37	Nd^{3+}	$^4F_{3/2} \rightarrow {}^4I_{9/2}$
978	1.27	Ho^{3+} Dy^{3+}	?
998	1.24	Ho^{3+} Dy^{3+}	?
1048 1062	1.18 1.17	Nd^{3+}	$^4F_{3/2} \rightarrow {}^4I_{11/2}$

The main difference between the IL of the two minerals is the shift in the Mn^{2+} emission from 607 nm in leucophanite to 630 nm in meliphanite. Mn^{2+} is presumed to substitute into the *Ca* site, which in both minerals is a square anti-prism with seven bonds to O and one to F. However, the average bond length <*Ca*-φ> of the *Ca* polyhedron in meliphanite is 2.497 Å (Grice & Hawthorne 2002) and 2.509 and 2.510 Å for Leuco8 and Leuco9, respectively (Friis *et al.* 2007a). Sommer (1972) explained the Mn^{2+} emission shift towards longer wavelength in the calcite-magnesite solid-solution to increasing crystal-field interaction with decreasing bond distances. The small change in *Ca*-φ of the *Ca* polyhedron in the two minerals is consistent with the different position of the Mn^{2+} emission observed. Gorobets & Rogojine (2002) found no difference in the position of the Mn^{2+} emission between meliphanite and leucophanite, but found an additional broad emission in meliphanite around 730 nm, which they ascribed to Fe^{3+}. The Norwegian meliphanites of this study do not demonstrate such a centre.

5.4.2 Comparison of PL

The broad excitation band around 330 nm in both minerals is a charge transfer band (CT), which efficiently excites all activators. One difference between the two minerals is that Mn^{2+} is easily excited by PL in meliphanite but only weakly by PL in leucophanite (Leuco9). The strongest Mn^{2+} emission is found in HAK followed by OST and ARS, which all have Mn concentrations higher than that of the leucophanite suite, suggesting that the Mn content is too dilute in leucophanite for it to act as an efficient activator of PL. Also, the subtle difference in <*Ca*-φ> between the two minerals could result in a more favourable position of the Mn^{2+} energy levels in the band-gap for meliphanite compared to leucophanite. The Mn^{2+} emission is coupled to phonon activation and is therefore only observed under the CT excitation, *i.e.* excitation through the lattice. Excitation with the line bands shown in Figs. 5.5 and 5.13 results in emissions associated with specific REE. The emission spectra for the two species reveal that very little energy is transferred between different REE upon excitation (Figs. 5.4 and 5.12). The Dy^{3+} emissions ~570 nm are clearly resolved for meliphanite, but not in leucophanite, which can be interpreted as the formation of clusters in the latter. However, the concentration of Dy in OST (215 ppm) is slightly higher than in Leuco5 (198 ppm) (Table 5.2 and Table 5 in Friis *et al.* 2007a), which is inconsistent with the formation of Dy^{3+} clusters. Although the Dy content is slightly higher in OST than in Leuco5, the total REE content is significantly higher in Leuco5 (9594 ppm) than in OST (3017 ppm), which may result in the formation of REE clusters in leucophanite.

5.4.3 UV-Blue Emission

The UV-Blue emission is observed in all samples under all types of excitation.

The origin of this emission has been attributed to both element and defect activation (Gorobets and Prokofiev 1981; Prokofiev *et al.* 1982; Gorobets and Rogojine 2002; Gaft *et al.* 2005). Friis *et al.* (2007b) found the same degree of temperature quenching in three leucophanite samples, despite chemical differences, which was not the case for the element activated centers. They therefore ascribed the centre to be defect related. A similar defect has also been reported for the Be-minerals chrysoberyl, phenakite and beryl (Korotaev *et al.* 2002). Gorobets and Prokofiev (1981) and Prokofiev *et al.* (1982) showed luminescence spectra of both natural and synthetic leucophanite. Interestingly, they ascribe emissions around 380 nm to Ce^{3+} in natural samples, but in an undoped synthetic sample they suggested it was caused by an oxygen defect.

The change in position of the emission band in leucophanite (Table 5.1) suggests that more than one activator is causing the emission. The dip in intensity observed for both minerals ~330 nm is caused by the strong charge transfer band. This may be mistaken as two individual peaks, but in reality is only one (Figs. 5.1 and 5.11). In CL the peaks are at higher energy than RL and the difference increases with REE content. The difference is also greater for the powder than for the cleavage fragment of Leuco5. Townsend *et al.* (1999) showed that CL is very surface dependent and the difference between CL and RL suggests that at least one component of the emission is a surface-related defect or a centre more readily excited in the surface region compared to the bulk. The presence of a defect emission is further supported by the fact that the broad excitation band is orders of magnitude stronger for this emission than for any other.

Ce^{3+} is inferred to contribute to luminescence in leucophanite (Gorobets & Prokofiev 1981; Prokofiev *et al.* 1982; Gorobets & Rogojine 2002; Gaft *et al.* 2005). PL and IL of meliphanite (Figs. 5.8 and 5.11) reveal a broad emission around 350 nm that is not observed for leucophanite. This band can either be caused by another defect or it could relate to an element activator like Ce^{3+}. One explanation for the presence of this emission in meliphanite and not in leucophanite is that the higher concentration of REE in leucophanite results in cluster formation, the efficiency of which are greatly reduced with respect to isolated centres. Another explanation is structural; Ce^{3+} luminescence is caused by *f-d* transitions and Blanc *et al.* (2000)

showed how the emission band shifts depending on the mineral host. The *Na* site in leucophanite is fully occupied by Na, where meliphanite has a surplus of Ca to fill the *Ca* site and the *Na* site becomes disordered with Ca. The presence of Ca in the *Na* site in meliphanite shows that this site is capable of incorporating higher valance cations. Rather than having just one site, it is likely that both *Ca* and *Na* in meliphanite can accommodate REE^{3+}. In studies of yttrium silicate doped with Ce^{3+} and co-doped with Gd^{3+} or Tb^{3+} Bosze *et al.* (2003) and Gonzalez-Ortega *et al.* (2005) typically ascribed emissions ~380 to 450 nm to Ce^{3+} depending on structure type. Furthermore, they ascribed a structurally independent emission at 419 nm to Tb^{3+}.

The shift to longer wavelength in RL compared to CL can also be explained by increased absorption with decreasing wavelength, combined with the difference in volume and depth from the surface where luminescence is generated with the two techniques. This concept is explained in Fig. 1.2 and discussed further for fluorapatite (Section 4.4.7).

5.4.4 Leucophanite vs. Meliphanite

The difference in luminescence efficiency between leucophanite and meliphanite can be interpreted in several ways. Meliphanite has a higher Fe content than leucophanite and Fe is a strong quencher of luminescence (Marfunin 1979). However, Table 5.2 shows that the samples with the highest Fe concentration also show the strongest luminescence. Therefore, the presence of Fe in meliphanite cannot account for the difference in luminescent efficiency. Friis *et al.* (2007b) showed that the element-activated luminescence centres experienced self-quenching. The meliphanites analysed in this study have higher Mn contents than any of the leucophanites analysed by Friis *et al.* (2007b), but again the strongest luminescent samples are also those with the highest Mn content (Table 5.2). Hence, self-quenching due to higher Mn content in meliphanite than in leucophanite cannot explain the observed differences. Pb^{2+} often works as a sensitizer for Mn^{2+} luminescence (Leverenz 1968; Marfunin 1979). However, the differences in Pb contents between the two minerals do not vary enough to account for the difference in luminescence.

The substitution of REE^{3+} for Ca^{2+} in leucophanite involves incorporation of additional Na and vacancies for Ca with no evidence for additional mechanisms, *e.g.* O^{2-} for F^- (Friis *et al.* 2007a). However, Fig. 5.6 indicates that several mechanisms are involved in the charge balance of REE^{3+} substituting for Ca^{2+} in meliphanite. Consequently, the formation of vacancies in leucophanite may facilitate energy transfer to the activators and hence explain differences in luminescence between the two minerals.

The luminescence of OST and HAK is as intense as data for leucophanite. Hence, there is no systematic reduction in efficiency compared with leucophanite. Furthermore, the well-defined emission bands in meliphanite compared to those of leucophanite potentially make meliphanite a more efficient phosphor than leucophanite, if it has the correct chemistry. One possibility for the lack of data on meliphanite could be related to the fact that meliphanite is rare outside the Langesundsfjord in Norway, whereas leucophanite is relatively common in most alkaline complexes.

5.4.5 Energy Transfer

Excitation via the CT band results in efficient excitation of all centres. This is also the case for CL, RL and IL, indicating that excitation related to the crystal structure or from the conduction band transfers energy to all activators. Excitation at specific wavelengths that corresponds to one particular activator, primarily generates luminescence from that one activator. Therefore, energy deposited onto one activator is not readily transferred to other activators. In other words, under selective excitation the minerals can be considered as single-doped closed systems, whereas under high energy or structural excitation the minerals behave as multi-doped systems. Since excitation with the CT band effectively transfers energy to all centres, REE luminescence in these minerals cannot be considered as free ions, because the structure influences the emission. Figure 5.10 shows that the intensity of the luminescence of OST decreases with beam exposure, which is a common feature. However, the intensity of the Dy^{3+} and the Sm^{3+}/Mn^{2+} emissions does not decrease at the same rate. Such behaviour further indicates that REE^{3+} do interact with the structure and that different REE have different degrees of interaction. The excitation spectra for Dy^{3+} and Sm^{3+} in both leucophanite and meliphanite show excitation bands characteristic for the respective elements and not for other REE. However, all show excitation via the structure, emphasising the lack of energy transfer between different REE and the strong interaction with the structure.

5.4.6 Leucophanite Low Temperature

Thick sections were prepared of several leucophanite samples. Fig. 5.15 shows that Leuco9 contains numerous two-phase fluid inclusions. Neither the fluid nor gas phases have been investigated further, hence their compositions are unknown. However, the gas phase does not move at room temperature indicating that it is not CO_2. The sample was formed after alteration of the primary pegmatite, therefore it is most likely that the liquid phase is H_2O, which supports the proposal by Kurt *et al.* (2002) that the sudden luminescence intensity increase observed in Fig. 5.14 for Leuco9 between 160 and 180 K could be related to a phase transition from cubic to hexagonal ice.

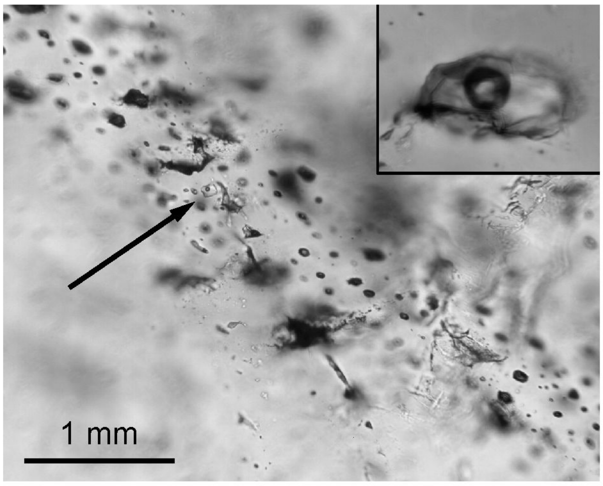

FIGURE 5.15: *Photomicrograph of a thick section of Leuco9 showing a trail of fluid inclusions running across the image. The arrow points towards a clearly imaged inclusion. The inset shows a ~0.4 mm inclusion demonstrating the two phase nature of the inclusion.*

5.5 Conclusions

The application of multiple forms of excitation reveals that the UV-Blue emission in leucophanite and meliphanite consists of more than one emission centre and is therefore more complex than previously thought. The most likely centres are defects related to the structure, *e.g.* in connection with the tetrahedral sites, and a Ce^{3+} centre. The difference in Na/Ca ratio between the two minerals make it possible for REE to substitute into two sites in meliphanite contrary, to just one in leucophanite.

This study reveals that meliphanite has the same emission centres as leucophanite and greatly expands on the only previous study of meliphanite (Gorobets & Rogojine 2002). The lower total REE content in meliphanite compared to leucophanite is consistent with a model whereby the formation of clusters is reduced and consequently generates sharper line emissions.

The small difference in the average bond-length of the *Ca* coordination between the two minerals is consistent with the shift observed in the position of the Mn^{2+} emission. Such observations are consistent with data from the calcite magnesite solid solution (Sommer 1972).

The excitation of specific REE in both leucophanite and meliphanite show that very little energy transfer occurs between different REE. Conversely, excitation through the lattice excites all emission centres.

Both leucophanite and meliphanite have excellent luminescence properties, especially at low dopant levels. Furthermore, the structural difference between the two related species indicates that meliphanite might be a promising phosphor.

Chapter 6

Conclusions

Conclusions

6.1 REE Luminescence - Recapped

Many REE have strong luminescence and have many applications, *e.g.* phosphors and scintillators. The energy levels in most REE are relatively closely spaced, which typically results in several emission bands in the visible part of the electromagnetic spectrum. Because the electrons involved in the luminescence are not valence electrons, luminescence from REE is not as dependent on the host matrix as, for example, luminescence from Mn^{2+}. Consequently, excitation and emission processes in REE are often explained using a “free ion” model. Such an assumption explains why REE emissions are generally found at the same wavelengths in different materials. However, small differences do occur, *e.g.* minute wavelength shifts between hosts and some REE have efficient luminescence in certain hosts, but not in others.

Some luminescence transitions are only allowed under certain site-symmetries, which makes it possible to use luminescence spectroscopy as a probe of local structure at concentrations far below techniques like NMR and XAFS. In other words, there is a great potential for determining REE distribution between non-symmetrical equivalent sites in a material. To further understand the interaction between REE and the structure and between different REE single- and multidoped materials are ideal. Minerals can be considered as extreme multidoped systems as they often contain all the REE, and in spite of, or because of, their complexity many fundamental luminescence mechanisms can be understood from studying minerals.

6.2 Luminescence for Site Distribution

This study has shown that the application of site-selective excitation and emission transitions to determine the number of non-equivalent activator sites is not straightforward. In particular, the dopant level has an effect that may lead to an underestimation of the number of non-equivalent sites. For example:

- The $^5D_0 \rightarrow {}^7F_0$ emission in Eu^{3+} (~580 nm) consists of only one peak in ZirEu, suggesting Eu^{3+} is present in only one site. However, site-selective excitation shows that Eu^{3+} is present in at least two different sites.

- In FAPEu3 the $^5D_0 \rightarrow {}^7F_0$ emission is split into at least three, possibly four, sharp emissions and the site-selective excitation also indicates Eu^{3+} is present in multiple sites. However, at higher dopant levels the main $^5D_0 \rightarrow {}^7F_0$ emission broadens and the total number of emissions is reduced. Furthermore, site-selective excitation does not result in different emission spectra.

These differences between the $^5D_0 \rightarrow {}^7F_0$ emission and site-selective excitation with concentration show that different structures react differently to increased dopant levels.

Not only the site-selection behaviour is affected by high dopant levels. The following effects are also influencing the luminescence at high dopant levels:

- The PL and XRD of FAPDy indicate that clusters are formed at higher dopant levels which reduces the quantum efficiency.
- The single-crystal XRD analyses of the natural apatites show that the distortion of the *Ca* polyhedra changes with increasing REE content, which has also been described for leucophanite (Friis *et al.* 2007a). For both apatite and leucophanite, changes in the distortion parameters are greatest for small concentrations of REE and as the concentration increase the distortion effects level out.

It is not possible to determine whether the changes in the $^5D_0 \rightarrow {}^7F_0$ for FAPEu with increasing dopant level reflects a reduction of sites, or if the changes in the coordination polyhedra modify the site-symmetry elements and hence influence the allowed/forbidden transitions. Another possibility is that the changes reflect cluster formation. Although applying luminescence as a structural probe is not straightforward and does not seem to be effective at high dopant levels in the mineral systems of this study, much information was deciphered at low dopant levels.

6.3 Energy Transfer between REE

Excitation with specific wavelengths like 352 and 404 nm of the Dy^{3+} and Sm^{3+} co-doped fluorapatite showed that 352 nm excited Dy^{3+} only, while 404 nm excited Sm^{3+} alone. This was also observed for natural fluorapatite, leucophanite and meliphanite, indicating that energy cascade between different REE is limited to interaction between specific REE, such as Gd^{3+} to Eu^{3+} in the synthetic zircons (Section 3.5.4). This also indicates that preferential luminescence from certain REE and not others in specific minerals cannot solely be explained by energy transfer between REE, but must involve interactions between the REE and the structure.

6.4 Interaction with Host

The IL analysis of the co-doped apatite and the CL of meliphanite show that the intensity reduction during implantation varies for different activators, providing further evidence that REE luminescence is affected by the surrounding structure. Furthermore, excitation by the broad UV absorption band, working as a charge transfer band in natural fluorapatite, leucophanite and meliphanite, excited most REE activators simultaneously. Broad excitation bands in the UV region are related to the structure and if this can be emulated in synthetic materials, it opens up the possibility for a whole new range of phosphors. Figure 5.1 shows schematically how the combination of multi-doped phosphor, containing a strong charge transfer band, can be used as a colour changing and “white-light” phosphor. By using the results from the natural minerals studied in this Thesis, it is concluded that little energy is transferred between different REE, so Fig. 5.1 could represent a material containing Eu^{2+}, Tb^{3+}, Dy^{3+} and Eu^{3+}. By choosing the correct excitation energy, each of the activators can be excited independent of the others to give the following colours: blue (Eu^{2+}), green (Tb^{3+}), yellow (Dy^{3+}) and red (Eu^{3+}). In contrast, if the excitation energy coincides with the charge transfer band, all activators will be excited simultaneously and hence the resulting colour would be close to white. Materials with such properties are highly sought for LEDs in low energy light sources with good colour representation.

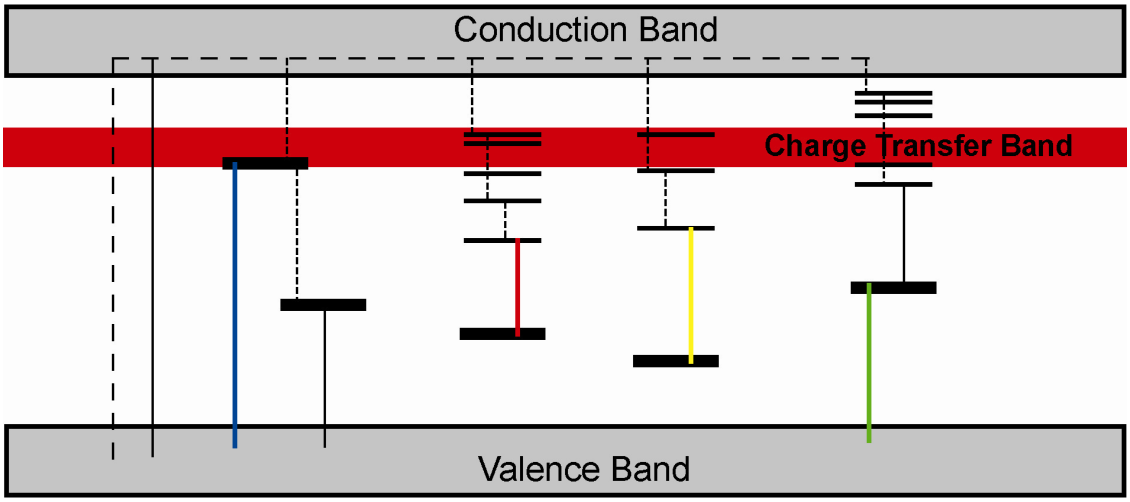

FIGURE 5.1: *Schematic drawing explaining how a charger transfer band in a multi-doped material can create a tuneable and "white-light" phosphor.*

6.5 Effect of Excitation Source

As mentioned in Section 1.2.2, the majority of luminescence studies use one type of excitation to explain the processes of excitation and emission. However, this study clearly demonstrates that valuable information is gained from using multiple techniques, as well as showing that application of different excitation types will result in different emissions for the same sample.

For example:

- the PL of ZirHo could not activate the minor Dy present in the sample, whereas Dy^{3+} emissions were reported with both RL (Karali *et al.* 2000) and IL (Finch *et al.* 2004).
- the Mn^{2+} emission dominates IL (Friis *et al.* 2007b), RL and CL of Leuco8, whereas in PL, Sm^{3+} and possibly other REE^{3+} emissions dominate the visible region. As the Sm^{3+} and Mn^{2+} emissions have similar peak positions in leucophanite, the luminescent colour does not differ to the naked eye between excitation techniques and could, without spectroscopy, be incorrectly interpreted.
- both leucophanite and fluorapatite show a change in the UV-blue emission between CL and RL. In leucophanite the broad UV emission shifts towards lower energy when changing from CL to RL and in fluorapatite a ~360 nm emission dominates over a ~450 nm emission in CL, whereas the converse is true for RL. One explanation is that the 450 nm emission in fluorapatite is

related to Eu^{2+} and during RL Eu^{3+} is reduced to Eu^{2+}, and hence dominates the RL and not CL. However, if that was the case it would also be expected to occur in leucophanite, but no emission ~450 nm is observed, while the ~419 nm emission increases and causes the shift. The 419 nm emission could be Eu^{2+}, but in a study of synthetic leucophanite, Prokofiev *et al.* (1982) showed that the Eu^{2+} emission is at 450 nm. A more likely explanation is that since minerals are generally more absorbing of UV than longer wavelength radiation, then UV emissions will be re-absorbed by the mineral more, than emissions in the visible region. As CL has shallow penetration, luminescence is generated close to the surface and only has to travel a short distance before exiting the material. In contrast, RL generates luminescence from the entire sample, therefore the luminescence has to travel through a much greater volume of the material. Consequently, a significant amount of the UV emission generated will never leave the sample, whereas the majority of the visible emissions will.

6.6 Luminescence as a Tool for Trace Element Concentration

Three findings of this study demonstrate that the application of luminescence as a routine technique for determining trace element concentration is not possible at the moment.

- During excitation the luminescence intensity of all emissions decreases as a function of dose.
- The decrease in intensity is not uniform but depends on activator.
- Self-quenching occurs at very different dopant levels depending on REE.

Furthermore, other analytical techniques have better LOD and less complex matrix corrections.

6.7 Luminescence Spectroscopy of Natural and Synthetic REE-bearing Minerals

The present study shows that important new information is gained by comparing light from different types of excitation. Furthermore, many of the conclusions benefit from combining the study of synthetic materials with that of natural mineral systems. It is possible to understand much about the local coordination state of REE ions in solids at concentrations below the LOD of XAFS and NMR from luminescence, but hard and fast rules about how to interpret luminescence data applicable to all systems are avoided. Interpretation of luminescence needs to be done in a system specific manner. The possibility to investigate both excitation and emission over a large wavelength range, made it possible to identify energy transfers in synthetic zircon with potential quantum cutting properties. The present study has also indicated that physical properties, like absorption, play a more important role for understanding excitation and emission, than currently expressed in the majority of luminescent studies. Finally, the strong interaction between the structure and REE, combined with the weak interaction between REE shown in this study, opens up the possibility to design new type of phosphors. Particularly, the luminescence and structure of meliphanite makes it a potentially interesting phosphor.

Acknowledgements

Acknowledgements

I would like to thank my supervisors Adrian A. Finch and Colin H. Donaldson from the University of St Andrews and C. T. Williams from the Natural History Museum, London, for constructive discussions and motivation, which led to the completion of this thesis. I am especially grateful for Adrian and Terry's courage to take me on as a student and securing funding from the University of St Andrews and NHM for this study. Furthermore, I'm grateful to them for letting me work on non-thesis related projects, too.

Many people have been extremely helpful and valuable over the past three years and I apologise if I have forgotten some. From St Andrews I would like to recognise the help I have received from Angus Calder and Donald Herd with XRD and EPMA analyses, not to mention for keeping me up-to-date with Scottish slang, and tales from the past, Colin D Cameron for being there when my computers were not, Helen Olaez for always being helpful and sorting out admin stuff, Stuart G. Allison for several guided tours through the Scottish geology and ales; as well as several other members of staff who have been very helpful with constructive discussions. At the NHM in London I would like to thank Tony Wighton for excellent and fast sample preparation, Teresa Jeffries for help with LA-ICPMS analyses and John Spratt and Anton Kearsley for assistance during EPMA analyses.

From the University of Sussex I would like to acknowledge the help I received from Dave E. Hole with IL data collection and Peter D. Townsend for subsequent fruitful discussions. I am grateful for the support from Nordic Mineralogical Network, which made it possible to visit Copenhagen to collect single-crystal and powder XRD data. Without the assistance of and discussions with Tonči Balić-Žunić, Helene Almind and Anna Katerinopoulou my data collection and interpretation would have been significantly more scattered.

I am particular in debt to John M. Hanchar for making his synthetic REE-doped zircons available for my study. I would like to thank private collector Alf Olav Larsen for his assistance during visits to the Langesundsfjord and also making samples and his vast knowledge available to me. Private collector Tom Weidner is likewise thanked for supplying samples for this study. Furthermore, I would like to thank the Hunterian Museum in Glasgow and the Geological Museum in Copenhagen for making samples available.

Greatly acknowledged is also the opportunity made available by Mark T. Weller to use the laboratory in Southampton and to join him and Jennifer A. Armstrong on three visits to ILL in Grenoble.

I am also grateful for all the help and support I have received from my girlfriend Joanna, without whom I would not have been fed for the past six months and still be speaking Denglish.

I am especially pleased with the support I have received from fellow students in St Andrews, in particular the moral and physical support from Jamie McCreath - to and from the pub. Georgina King, Cheryl Wood, Keziah Stott, Tom Clemens and David Small are thanked for making my visits to St A less scientific. I would also like to thank my previous housemates Graham “Speed Programmer” Milne and Paul “Parrot” Everett for convincing me that not all Scottish guys drink pink tea, AND for introducing me to such fine dining as Scotch and Pickled Eggs, not to mention Tennent’s. I would also like to thank Ellen De Man and Stefaan Van Simaeys for not living in Scotland, as that would definitely have delayed my Thesis. I would like to thank Bugge, Hougaard and Jebens for the “occasional” Skype beer (or two), they have kept me sane. Andreas O. Harstad and Asbjørn Brekke are thanked for always bringing back sunshine on grey Nordic days.

And finally, I would like to thank my parents, Eva and Per, for abandoning me at numerous Norwegian roadcuts over the years and also for letting me fill their house with minerals.

References

References

ALIVISATOS, A.P. (1996) Perspectives on the physical chemistry of semiconductor nanocrystals. *Journal of Physical Chemistry*, **100**, 13226-13239.

ANNAPURNA, K., DWIVEDI, R.N., KUNDU, P. and BUDDHUDU, S. (2003) Fluorescence properties of Sm^{3+}: $ZnCl_2$-$BaCl_2$-LiCl glass. *Materials Research Bulletin*, **38**, 429-436.

ANTONAKOS, A., LIAROKAPIS, E. and LEVENTOURI, T. (2007) Micro-Raman and FTIR studies of synthetic and natural apatites. *Biomaterials*, **28**, 3043-3054.

ASHBROOK, S.E. and FARNAN, I. (2004) Solid-state ^{17}O nuclear magnetic resonance spectroscopy without isotopic enrichment: Direct detection of bridging oxygen in radiation damaged zircon. *Solid State Nuclear Magnetic Resonance*, **26**, 105-112.

ATKINS, P., OVERTON, T., ROURKE, J., WELLER, M. and ARMSTRONG, F. (2006) *Inorganic Chemistry*. 822 p. Oxford University Press, Oxford.

BABU, P., JANG, K.H., SEO, H.J. and JAYASANKAR, C.K. (2006) Optical and site-selective spectral studies of Eu^{3+}-doped zinc oxyfluorotellurite glass. *Journal of Applied Physics*, **99**, Article 53522.

BADENES, J.A., VICENT, J.B., LLUSAR, M., TENA, M.A. and MONRÓS, G. (2002) The nature of Pr-$ZrSiO_4$ yellow ceramic pigment. *Journal of Materials Science*, **37**, 1413-1420.

BALIĆ-ŽUNIĆ, T. and MAKOVICKY, E. (1996) Determination of the centroid or "the best centre" of a coordination polyhedron. *Acta Crystallographica*, **B52**, 78-81.

BALIĆ-ŽUNIĆ, T. and VICKOVIĆ, I. (1996) IVTON. A program for the calculation of geometrical aspects of crystal structures and some crystal chemical applications. *Journal of Applied Crystallography*, **29**, 305-306.

BARBARAND, J. and PAGEL, M. (2001) Cathodoluminescence study of apatite crystals. *American Mineralogist*, **86**, 473-484.

BAUMER, A., BLANC, P., CESBRON, F. and OHNENSTETTER, D. (1997) Cathodoluminescence of synthetic (doped with rare-earth elements) and natural anhydrites. *Chemical Geology*, **138**, 73-80.

BERAN, A., VOLL, D. and SCHNEIDER, H. (2004) IR spectroscopy as a tool for the characterisation of ceramic precursor phases. In A. Beran and E. Libowitzky, Eds. *EMU Notes in Mineralogy*, **6**, p. 189-226. European Mineralogical Union, Budapest.

BLANC, P., BAUMER, A., CESBRON, F., OHNENSTETTER, D., PANCZER, G. and RÉMOND, G. (2000) Systematic cathodoluminescence spectral analysis of synthetic doped minerals: anhydrite, apatite, calcite, fluorite, scheelite and zircon. In M. Pagel, V. Barbin, P. Blanc and D. Ohnenstetter, Eds. *Cathodoluminescence in Geosciences*, p. 127-160. Springer, Berlin.

BLASSE, G. (1975) Influence of local charge compensation on site occupation and luminescence of apatites. *Journal of Solid State Chemistry*, **14**, 181-184.

BOSZE, E.J., HIRATA, G.A., SHEA-ROHWER, L.E. and MCKITTRICK, J. (2003) Improving the efficiency of a blue-emitting phosphor by an energy transfer from Gd^{3+} to Ce^{3+}. *Journal of Luminescence*, **104**, 47-54.

BROOKS, R.J., FINCH, A.A., HOLE, D.E., TOWNSEND, P.D. and WU, Z. (2002) The red to near-infrared luminescence in alkali feldspar. *Contributions to Mineralogy and Petrology*, **143**, 484-494.

BURKE, E.A.J. (2008) Tidying up mineral names: An IMA-CNMNC scheme for suffixes, hyphens and diacritical marks. *The Mineralogical Record*, **39**, 131-135.

CAMARGO, A.S.S.D., DAVOLOS, M.R. and NUNES, L.A.O. (2002) Spectroscopic characteristics of Er^{3+} in two crystallographic sites of Gd_2SiO_5. *Journal of Physics: Condensed Matter*, **14**, 3353-3363.

CAMPBELL, L.S. and HENDERSON, P. (1997) Apatite paragenesis in the Bayan Obo REE-Nb-Fe ore deposit, Inner Mongolia, China. *Lithos*, **42**, 89-103.

CANNILLO, E., GIUSEPPETTI, G. and TAZZOLI, V. (1967) The crystal structure of leucophanite. *Acta Crystallographica*, **23**, 255-259.

CHAKHMOURADIAN, A.R., REGUIR, E.P. and MITCHELL, R.H. (2002) Strontium-apatite: New occurrences, and the extent of Sr-for-Ca substitution in apatite-group minerals. *The Canadian Mineralogist*, **40**, 121-136.

CHEN, N., PAN, Y. and WEIL, J.A. (2002a) Electron paramagnetic resonance spectroscopic study of synthetic fluorapatite: Part I. Local structural environment and substitution mechanism of Gd^{3+} at the Ca2 site. *American Mineralogist*, **87**, 37-46.

CHEN, N., PAN, Y., WEIL, J.A. and NILGES, M.J. (2002b) Electron paramagnetic resonance spectroscopic study of synthetic fluorapatite: Part II. Gd^{3+} at the Ca1 site, with a neighboring Ca2 vacancy. *American Mineralogist*, **87**, 47-55.

COMODI, P., LIU, Y., STOPPA, F. and WOOLLEY, A.R. (1999) A multi-method analysis of Si-, S- and REE-rich apatite from a new find of kalsilite-bearing leucitite (Abruzzi, Italy). *Mineralogical Magazine*, **63**, 661-672.

DORENBOS, P., VAN LOEF, E.V.D., VINK, A.P., VAN DER KOLK, E., VAN EIJK, C.W.E., KRÄMER, K.W., GÜDEL, H.U., HIGGINS, W.M. and SHAH, K.S. (2006) Level location and spectroscopy of Ce^{3+}, Pr^{3+}, Er^{3+} and Eu^{2+} in $LaBr_3$. *Journal of Luminescence*, **117**, 147-155.

ELLIOTT, C.J. (1994) *Structure and Chemistry of the Apatites and Other Calcium Orthophophates*. 389 p. Elsevier, Amsterdam.

EWING, R.C., LUTZE, W. and WEBER, W.J. (1995) Zircon - a host-phase for the disposal of weapons plutonium. *Journal of Materials Research*, **10**, 243-246.

EWING, R.C., MELDRUM, A., WANG, L., WEBER, W.J. and CORRALES, L.R. (2003) Radiation effects in zircon. In J.M. Hanchar and P.W.O. Hoskin, Eds. *Reviews in Mineralogy & Geochemistry*, **53**, p. 387-425. Mineralogical Society of America, Washington D.C.

FARGES, F. and CALAS, G. (1991) Structural analysis of radiation damage in zircon and thorite: An X-ray absorption spectroscopic study. *American Mineralogist*, **76**, 60-73.

FARGES, F. (1994) The structure of metamict zircon: A temperature-dependent EXAFS study. *Physics and Chemistry of Minerals*, **20**, 504-514.

FARNAN, I. and SALJE, E.K.H. (2001) The degree and nature of radiation damage in zircon observed by ^{29}Si nuclear magnetic resonance. *Journal of Applied Physics*, **89**(4), 2084-2090.

FARNAN, I., CHO, H., WEBER, W.J., SCHEELE, R.D., JOHNSON, N.R. and KOZELISKY, A.E. (2004) High-resolution solid-state nuclear magnetic resonance experiments on highly radioactive ceramics. *Review of Scientific Instruments*, **75**(12), 5232-5236.

FERDOV, S., SÁ FERREIRA, R.A. and LIN, Z. (2008) Optical properties and local structure of Eu^{3+}-doped synthetic analogue of microporous titanosilicate mineral sitinakite. *Journal of Luminescence*, **128**, 1108-1112.

FINCH, R.J., HANCHAR, J.M., HOSKIN, P.W.O. and BURNS, P.C. (2001) Rare-earth elements in synthetic zircon: Part 2. A single-crystal X-ray study of xenotime substitution. *American Mineralogist*, **86**, 681-689.

FINCH, R.J. and HANCHAR, J.M. (2003) Structure and chemistry of zircon and zircon-group minerals. In J.M. Hanchar and P.W.O. Hoskin, Eds. *Reviews in Mineralogy & Geochemistry*, **53**, p. 1-25. Mineralogical Society of America, Washington D.C.

FINCH, A.A., GARCIA-GUINEA, J., HOLE, D.E., TOWNSEND, P.D. and HANCHAR, J.M. (2004) Ionoluminescence of zircon: rare earth emissions and radiation damage. *Journal of Physics D: Applied Physics*, **37**, 2795-2803.

FLEET, M.E. and PAN, Y. (1995) Site preference of rare earth elements in fluorapatite. *American Mineralogist*, **80**, 329-335.

FLEET, M.E. and PAN, Y. (1997) Site preference of rare earth elements in fluorapatite: Binary (LREE+HREE)-substituted crystals. *American Mineralogist*, **82**, 870-877.

FLEET, M.E. and LIU, X. (2008) Accommodation of the carbonate ion in fluorapatite synthesized at high pressure. *American Mineralogist*, **93**, 1460-1469.

FRIIS, H., BALIĆ-ŽUNIĆ, T., PEKOV, I.V. and PETERSEN, O.V. (2004) Kuannersuite-(Ce), $Ba_6Na_2REE_2(PO_4)_6FCl$, a new member of the apatite group, from the Ilímaussaq alkaline complex, South Greenland: Description and crystal chemistry. *Canadian Mineralogist*, **42**, 95-106.

FRIIS, H., BALIĆ-ŽUNIĆ, T., WILLIAMS, C.T. and GARCIA-SANCHEZ, R. (2007a) Incorporation of REE into leucophanite: a compositional and structural study. *Mineralogical Magazine*, **71**, 625-640.

FRIIS, H., FINCH, A.A., TOWNSEND, P.D., HOLE, D.E. and EL MKAMI, H. (2007b) Ionoluminescence of leucophanite. *American Mineralogist*, **92**, 254-260.

GAFT, M. (1992) Application of thermal treatment of zircon for the interpretation of luminescence centers. *Journal of Thermal Analysis*, **38**, 2281-2290.

GAFT, M., REISFELD, R., PANCZER, G., SHOVAL, S., CHAMPAGNON, B. and BOULON, G. (1997) Eu^{3+} luminescence in high-symmetry sites of natural apatites. *Journal of Luminescence*, **72-74**, 572-574.

GAFT, M., REISFELD, R., PANCZER, G., BLANK, P. and BOULON, G. (1998) Laser-induced time-resolved luminesncece of minerals. *Spectrochimica Acta Part A*, **54**, 2163-2175.

GAFT, M., REISFELD, R., PANCZER, G., USPENSKY, E., VARREL, B. and BOULON, G. (1999) Luminescence of Pr^{3+} in minerals. *Optical Materials*, **13**, 71-79.

GAFT, M., PANCZER, G., REISFELD, R. and SHINNO, I. (2000a) Laser-induced luminescence of rare-earth elements in natural zircon. *Journal of Alloys and Compounds*, **300-301**, 267-274.

GAFT, M., PANCZER, G., REISFELD, R., SHINNO, I., CHAMPAGNON, B. and BOULON, G. (2000b) Laser-induced Eu^{3+} luminescence in zircon $ZrSiO_4$. *Journal of Luminescence*, **87-89**, 1032-1035.

GAFT, M., PANCZER, G., REISFELD, R. and USPENSKY, E. (2001) Laser-induced time-resolved luminescence as a tool for rare-earth element identification in minerals. *Physics and Chemistry of Minerals*, **28**, 347-363.

GAFT, M., SHINNO, I., PANCZER, G. and REISFELD, R. (2002) Laser-induced time-resolved spectroscopy of visible broad luminescence bands in zircon. *Mineralogy and Petrology*, **76**, 235-246.

GAFT, M., REISFELD, R. and PANCZER, G. (2005) *Luminescence Spectroscopy of Minerals and Materials*. 358 p. Springer-Verlag, Heidelberg.

GILLHAUS, A., RICHTER, D.K., MEIJER, J., NEUSER, R.D. and STEPHAN, A. (2001) Quantitative high resolution cathodoluminescence spectroscopy of diagenetic and hydrothermal dolomites. *Sedimentary Geology*, **140**, 191-199.

GONZALEZ-ORTEGA, J.A., TEJEDA, E.M., PEREA, N., HIRATA, G.A., BOSZE, E.J. and MCKITTRICK, J. (2005) White light emission from rare earth activated yttrium silicate nanocrystalline powders and thin films. *Optical Materials*, **27**, 1221-1227.

GOROBETS, B.S. and PROKOFIEV, I.V. (1981) Luminescence of beryllium minerals. *Izvestiya Akademii Nauk SSSR Seriya Geologicheskaya*, **4**, 117-130.

GOROBETS, B.S. and ROGOJINE, A.A. (2002) *Luminescent Spectra of Minerals*. 300 p. RPC VIMS, Moscow.

GÖTZE, J., HABERMANN, D., NEUSER, R.D. and RICHTER, D.K. (1999) High-resolution spectrometric analysis of rare earth elements-activated cathodoluminescence in feldspar minerals. *Chemical Geology*, **153**, 81-91.

GÖTZE, J. (2002) Potential of cathodoluminescence (CL) microscopy and spectroscopy for analysis of minerals and materials. *Analytical and Bioanalytical Chemistry*, **374**, 703-708.

GÖTZE, J., PLÖTZE, M. and TRAUTMANN, T. (2005) Structure and luminescence characteristics of quartz from pegmatites. *American Mineralogist*, **90**, 13-21.

GRICE, J.D. and HAWTHORNE, F.C. (1989) Refinement of the crystal structure of leucophanite. *Canadian Mineralogist*, **27**, 193-197.

GRICE, J.D. and HAWTHORNE, F.C. (2002) New data on meliphanite, $Ca_4(Na,Ca)_4Be_4AlSi_7O_{24}(F,O)_4$. *Canadian Mineralogist*, **40**, 971-980.

HABERMANN, D., NEUSER, R.D. and RICHTER, D.K. (1998) Low limit of Mn^{2+}-activated cathodoluminescence of calcite: state of the art. *Sedimentary Geology*, **116**, 13-24.

HABERMANN, D., MEIJER, J., NEUSER, R.D., RICHTER, D.K., ROLFS, C. and STEPHAN, A. (1999) Micro-PIXE and quantitative cathodoluminescence spectroscopy: Combined high resolution trace element analyses in minerals. *Nuclear Instruments and Methods in Physics Research Section B*, **150**, 470-477.

HABERMANN, D. (2002) Quantitative cathodoluminescence (CL) spectroscopy of minerals: possibilities and limitations. *Mineralogy and Petrology*, **76**, 247-259.

HANCHAR, J.M., FINCH, R.J., HOSKIN, P.W.O., WATSON, E.B., CHERNIAK, D.J. and MARIANO, A.N. (2001) Rare earth elements in synthetic zircon: Part 1. Synthesis, and rare earth element and phosphorus doping. *American Mineralogist*, **86**, 667-680.

HANSEN, T.C., HENRY, P.F., FISCHER, H.E., TORREGROSSA, J. and CONVERT, P. (2008) The D20 instrument at the ILL: a versatile high-intensity two-axis neutron diffractometer. *Measurement Science & Technology*, **19**, 1-6.

HAWTHORNE, F.C. and HUMINICKI, D.M.C. (2002) The crystal chemistry of beryllium. In E.S. Grew, Ed. *Reviews in Mineralogy and Geochemistry*, **50**, p. 333-403. The Mineralogical Society of America, Washington, D. C.

HOMMAN, N.P.-O., YANG, C. and MALMQVIST, K.G. (1994) A highly sensitive method for rare-earth element analysis using ionoluminescence combined with PIXE. *Nuclear Instruments and Methods in Physics Research A*, **353**, 610-614.

HUGHES, J.M., CAMERON, M. and CROWLEY, K.D. (1991a) Ordering of divalent cations in the apatite structure: Crystal structure refinements of natural Mn- and Sr-bearing apatite. *American Mineralogist*, **76**, 1857-1862.

HUGHES, J.M., CAMERON, M. and MARIANO, A.N. (1991b) Rare-earth-element ordering and structural variations in natural rare-earth-bearing apatites. *American Mineralogist*, **76**(7-8), 1165-1173.

HUGHES, J.M. and RAKOVAN, J. (2002) The crystal structure of apatite, $Ca_5(PO_4)_3(F,OH,Cl)$. In M.J. Kohn, J. Rakovan and J.M. Hughes, Eds. *Reviews in Mineralogy & Geochemistry*, **48**, p. 1-12. Mineralogical Society of America, Washington D.C.

JAGANNATHAN, R. and KOTTAISAMY, M. (1995) Eu^{3+} luminescence: a spectral probe in $M_5(PO_4)_3X$ apatites (M = Ca or Sr; X = F^-, Cl^-, Br^- or OH^-). *Journal of Physics: Condensed Matter*, **7**, 8453-8466.

JAYASANKAR, C.K. and BABU, P. (2000) Optical properties of Sm^{3+} ions in lithium borate and lithium fluoroborate glases. *Journal of Alloys and Compounds*, **307**, 82-95.

JAYASUNDERA, A., FINCH, A.A., TOWNSEND, P.D. and LIGHTFOOT, P. (2007) Hydrothermal synthesis and luminescent properties of a new family of organically templated lanthanide fluorides. *Journal of Materials Chemistry*, **17**, 4178-4183.

JIA, W., JIA, D., RODRIGUEZ, T., EVANS, D.R., MELTZER, R.S. and YEN, W.M. (2006) UV excitation and trapping centers in $CaTiO_3$:Pr^{3+}. *Journal of Luminescence*, **119**, 13-18.

JIA, W., JIA, D., RODRIGUEZ, T., WANG, Y., JIANG, H. and LI, K. (2007) Emission of Pr^{3+} from two sites in $CaHfO_3$ perovskite. *Journal of Luminescence*, **122-123**, 55-57.

KAR, J.K., STEVENS, R. and BOWEN, C.R. (2004) Novel terbium-zircon yellow pigment. *Journal of Materials Science*, **39**, 5755-5763.

KARALI, T., CAN, N., TOWNSEND, P.D., ROWLANDS, A.P. and HANCHAR, J.M. (2000) Radioluminescence and thermoluminescence of rare earth element and phosphorus-doped zircon. *American Mineralogist*, **85**, 668-681.

KARMAKAR, B. (2005) IRRS, UV-Vis-NIR absorption and photoluminescence upconversion in Ho^{3+}-doped oxyfluorophosphate glasses. *Journal of Solid State Chemistry*, **178**, 2663-2672.

KEMPE, U. and GÖTZE, J. (2002) Cathodoluminescence (CL) behaviour and crystal chemistry of apatite from rare-metal deposits. *Mineralogical Magazine*, **66**, 151-172.

KIMATA, M. and OHASHI, H. (1982) The crystal structure of synthetic gugiaite, $Ca_2BeSi_2O_7$. *Neues Jahrbuch für Mineralogie-Abhandlungen*, **143**, 210-222.

KIRSH, Y. and TOWNSEND, P.D. (1987) Electron and hole centres produced in zircon by x-irradiation at room temperature. *Journal of Physics C: Solid State Physics*, **20**, 967-980.

KLEVTSOVA, R.F. and BORISOV, S.V. (1964) The crystal structure of belovite. *Structure Reports*, **29**, 374.

KNUTSON, C., PEACOR, D.R. and KELLY, W.C. (1985) Luminescence, color and fission track zoning in apatite crystals of the Panasqueira tin-tungsten deposit, Beira-Baixa, Portugal. *American Mineralogist*, **70**, 829-837.

KODAIRA, C.A., BRITO, H.F., TEOTONIO, E.E.S., FELINTO, M.C.F.C., MALTA, O.L. and BRITO, G.E.S. (2004) Photoluminescence behavior of the Sm^{3+} and Tb^{3+} ions doped into the $Gd_2(WO_4)_3$ matrix prepared by the Pechini and ceramic methods. *Journal of the Brazilian Chemical Society*, **15**, 890-896.

KOROTAEV, A.V., IVANOV, V.Y., PUSTOVAROV, V.A., KRUZHALOV, A.V. and SHULGIN, B.V. (2002) Time-resolved spectroscopy of complex scintillators Al_2BeO_4, Be_2SiO_4 and $Al_2Be_3Si_6O_{18}$. *Nuclear Instruments and Methods in Physics Research A*, **486**, 417-421.

KREBS, J.K. and BROWNSTEIN, J.M. (2007) Site-selective spectroscopy of Eu^{3+} in bioactive glass. *Journal of Luminescence*, **124**, 257-259.

KURT, K., RAMACHANDRAN, V., MAGHRABI, M., TOWNSEND, P.D. and YANG, B. (2002) Influence of phase transitions of ice on near-surface cathodoluminescence. *Journal of Physics: Condensed Matter*, **14**, 4319-4328.

LAKSHMANAN, A.R. and TOMITA, A. (1999) Thermostimulated luminescence, exoelectron emission and X-ray induced luminescence studies in $CaSO_4$: Eu and $CaSO_4$: Eu, Na. *Physica Status Solidi a-Applied Research*, **173**, 503-520.

LARSON, A.C. and VON DREELE, R.B. (2000) *General Structure Analysis System (GSAS)*.Report LAUR 86-748. Los Alamos National Laboratory

LARUHIN, M.A., VAN ES, H.J., BULKA, G.R., TURKIN, A.A., VAINSHTEIN, D.I. and DEN HARTOG, H.W. (2002) EPR study of radiation-induced defects in the thermoluminescence dating medium zircon ($ZrSiO_4$). *Journal of Physics: Condensed Matter*, **14**, 3813-3831.

LEE, J.H. and KIM, Y.J. (2008) Luminescent properties of Pr doped $ZrSiO_4$ phosphors. *Ceramics International*, **34**, 1113-1116.

LEVERENZ, H.W. (1968) *An Introduction to Luminescence of Solids*. 569 p. Dover Publications, inc., New York.

LI, Y.-C., CHANG, Y.-H., TSAI, B.-S., CHEN, Y.-C. and LIN, Y.-F. (2006) Luminescent properties of Eu-doped germanate apatite $Sr_2La_8(GeO_4)O_2$. *Journal of Alloys and Compounds*, **416**, 199-205.

LI, Y.C., CHANG, Y.-H., LIN, Y.-F., CHANG, Y.S. and LIN, Y.J. (2007) Luminescent properties of trivalent praseodymium-doped lanthanum aluminum germanate $LaAlGe_2O_7$. *Journal of Physics and Chemistry of Solids*, **68**, 1940-1945.

LIDE, D.R. (1994) CRC Handbook of Chemistry and Physics, p. 2380. CRC Press, Inc., Boca Raton.

LIU, F.S., LIU, Q.L., LIANG, J.K., LUO, J., YANG, L.T., SONG, G.B., ZHANG, Y., WANG, L.X., YAO, L.N. and RAO, G.H. (2005) Optical spectra of Ln^{3+} (Nd^{3+}, Sm^{3+}, Dy^{3+}, Ho^{3+}, Er^{3+})-doped Y_3GaO_6. *Journal of Luminescence*, **111**, 61-68.

LONG, M., HONG, F., LI, W., LI, F., ZHAO, H., LV, Y., LI, H., HU, F., SUN, L., YAN, C. and WEI, Z. (2008) Size-dependent microstructure and europium site preference influence fluorescent properties of Eu^{3+}-doped $Ca_{10}(PO_4)_6(OH)_2$ nanocrystal. *Journal of Luminescence*, **128**, 428-436.

LOUIS-ACHILLE, V., DE WINDT, L. and DEFRANCESCHI, M. (2000) Electronic structure of minerals: The apatite group as a relevant example. *International Journal of Quantum Chemistry*, **77**, 991-1006.

LUFF, B.J. and TOWNSEND, P.D. (1993) High sensitivity thermoluminescence spectrometer. *Measurement Science & Technology*, **4**, 65-71.

MAGHRABI, M., TOWNSEND, P.D. and VAZQUES, G. (2001) Low temperature luminescence from the near surface region of Nd:YAG. *Journal of Physics: Condensed Matter*, **13**, 2497-2515.

MAI, H.X., ZHANG, Y.W., SI, R., YAN, Z.G., SUN, L.D., YOU, L.P. and YAN, C.H. (2006) High-quality sodium rare-earth fluoride nanocrystals: Controlled synthesis and optical properties. *Journal of the American Chemical Society*, **128**, 6426-6436.

MAKOVICKY, E. and BALIĆ-ŽUNIĆ, T. (1998) New measure of distortion for coordination polyhedra. *Acta Crystallographica*, **B54**, 766-773.

MALINS, A.E.R., POOLTON, N.R.J., QUINN, F.M., JOHNSEN, O. and DENBY, P.M. (2004) Luminescence excitation characteristics of Ca, Na and K-aluminosilicates (feldspars) in the stimulation range 5-40 eV: determination of the band-gap energies. *Journal of Physics. D: Applied Physics*, **37**, 1439-1450.

MARFUNIN, A.S. (1979) *Spectroscopy, Luminescence and Radiation Centers in Minerals*. 352 p. Springer-Verlag, Berlin.

MARIMUTHU, K., NEHRU, L.C., MANI, A., RAMESH, R., MURALIDHARAN, G. and JAGANNATHAN, R. (2001) Apatites and britholites, are they akin - as probed by Eu^{3+} luminescence? *Journal of Physics: Condensed Matter*, **13**, 537-547.

MARSHALL, D.J. (1988) *Cathodoluminescence of Geological Materials*. 146 p. Unwin Hyman, Boston.

MAYER, I. and COHEN, S. (1983) The crystal structure of $Ca_6Eu_2Na_2(PO_4)_6F_2$. *Journal of Solid State Chemistry*, **48**, 17-20.

MITCHELL, R.H., XIONG, J., MARIANO, A.N. and FLEET, M.E. (1997) Rare-earth-element-activated cathodoluminescence in apatite. *Canadian Mineralogist*, **35**, 979-998.

MOIZAN, V., NAZABAL, V., TROLES, J., HOUIZOT, P., ADAM, J-L., DOUALAN, J-L., MONCORGÉ, R., SMEKTALA, F., GADRET, G., PITOIS, S. and CANAT, G. (2008) Er^{3+}-doped GeGaSbS glasses for mid-IR fibre laser application: Synthesis and rare earth spectroscopy. *Optical Materials*, **31**, 39-46.

NASDALA, L., ZHANG, M., KEMPE, U., PANCZER, G., GAFT, M., ANDRUT, M. and PLÖTZE, M. (2003) Spectroscopic methods applied to zircon. In J.M. Hanchar and P.W.O. Hoskin, Eds. *Reviews in Mineralogy & Geochemistry*, **53**, p. 427-467. Mineralogical Society of America, Washington D.C.

NASDALA, L., GÖTZE, J., HANCHAR, J.M., GAFT, M. and KRBETSCHEK, M.R. (2004a) Luminescence techniques in Earth Sciences. In A. Beran and E. Libowitzky, Eds. *EMU Notes in Mineralogy*, **6**, p. 43-91. European Mineralogical Union, Budapest.

NASDALA, L., REINERS, P.W., GARVER, J.I., KENNEDY, A.K., STERN, R.A., BALAN, E. and WIRTH, R. (2004b) Incomplete retention of radiation damage in zircon from Sri Lanka. *American Mineralogist*, **89**, 219-231.

NICHOLAS, J.V. (1967) Origin of the luminescence in natural zircon. *Nature*, **215**, 1476.

NIESERT, A., SIEVERS, R., SIGGEL, A., LANGER, K. and JANSEN, M. (2004) Preparation and optical absorption of zircons, co-doped with vanadium and rare earth elements. *Solid State Sciences*, **6**, 1149-1154.

NIKČEVIĆ, I., JOKANOVIĆ, V., MITRIĆ, M., NEDIĆ, Z., MAKOVEC, D. and USKOKOVIĆ, D. (2004) Mechanochemical synthesis of nanostructured fluorapatite/fluorhydroxyapatite and carbonated fluorapatite/fluorhydroxyapatite. *Journal of Solid State Chemistry*, **177**, 2565-2574.

OCANÃ, M., CABALLERO, A., GONZÁLEZ-ELÍPE, A.R., TARTAJ, P. and SERNA, C.J. (1998) Valence and localization of praseodymium in Pr-doped zircon. *Journal of Solid State Chemistry*, **139**, 412-415.

OOMEN, E.W.J.L., VAN DER VLIST, K., SMIT, W.M.A. and BLASSE, G. (1986) Luminescence of iron (III) in zircon-structured phosphates MPQ_4 (M = Sc, Lu, Y). *Chemical Physics Letters*, **129**(1), 9-12.

OSKAM, K.D., HOUTEPEN, A.J. and MEIJERINK, A. (2002) Site selective 4f5d spectroscopy of $CaF_2:Pr^{3+}$. *Journal of Luminescence*, **97**, 107-114.

PAGEL, M., BARBIN, V., BLANC, P. and OHNENSTETTER, D. (2000) *Cathodoluminescence in Geosciences*, p. 514. Springer, Berlin.

PAN, Y., CHEN, N., WEIL, J.A. and NILGES, M.J. (2002a) Electron paramagnetic resonance spectroscopic study of synthetic fluorapatite: Part III. Structural characterization of sub-ppm-level Gd and Mn in minerals at W-band frequency. *American Mineralogist*, **87**, 1333-1341.

PAN, Y., FLEET, M.E., CHEN, N., WEIL, J.A. and NILGES, M.J. (2002b) Site preference of Gd in synthetic fluorapatite by single-crystal W-band EPR and X-ray refinement of the structure: A comparative study. *Canadian Mineralogist*, **40**, 1103-1112.

PARK, S., JANG, K., KIM, S., KIM, I. and SEO, H. (2006) X-ray-induced reduction of Sm^{3+}-doped SrB_6O_{10} and its room temperature optical hole burning. *Journal of Physics: Condensed Matter*, **18**, 1267-1274.

PEKOV, I.V., KULIKOVA, I.M., KABALOV, Y.K., ELETSKAYA, O.V., CHUKANOV, N.V., MENSHIKOV, Y.P. and KHOMYAKOV, A.P. (1996) Belovite-(La) $Sr_3Na(La,Ce)(PO_4)_3(F,OH)$, a new rare earth mineral in the apatite group. *Zapiski Vsesoyuznogo Mineralogicheskogo Obshchestva*, **125**, 101-109.

PENG, M. and HONG, G. (2007) Reduction from Eu^{3+} to Eu^{2+} in $BaAl_2O_4$:Eu phosphor prepared in an oxidizing atmosphere and luminescent properties of $BaAl_2O_4$:Eu. *Journal of Luminescence*, **127**, 735-740.

PIRIOU, B., ELFAKIR, A. and QUARTON, M. (2001) Site-selective spectroscopy of Eu^{3+} -doped sodium lead phosphate apatite. *Journal of Luminescence*, **93**, 17-26.

POUCHOU, J.L. and PICHOIR, F. (1984) Quantitative microanalytic possibilities using a new formulation of matrix effects. *J. de Physique*, **45**, 17-20.

PROKOFIEV, I.V., GOROBETS, B.S., GAFT, M.L. and LURIE, Y.S. (1982) Rare earth centers of luminescence in leucophanite, shortite, meionite and monazite. *Mineralogicheskij Sbornik Lvovskogo Universiteta*, **36**, 76-79.

RAKOVAN, J.F. and HUGHES, J.M. (2000) Strontium in the apatite structure: Strontian fluorapatite and belovite-(Ce). *The Canadian Mineralogist*, **38**, 839-845.

RAKOVAN, J.F. (2002) Growth and surface properties of apatite. In M.J. Kohn, J. Rakovan and J.M. Hughes, Eds. *Reviews in Mineralogy & Geochemistry*, **48**, p. 51-86. Mineralogical Society of America, Washington D.C.

RAO, B.V., RAMBABU, U. and BUDDHUDU, S. (2007) Emission analysis of Sm^{3+} :$Ca_4GdO(BO_3)_3$ powder phosphor. *Materials Letters*, **61**, 2868-2871.

REISFELD, R., GAFT, M., BOULON, G., PANCZER, G. and JØRGENSEN, C.K. (1996) Laser-induced luminescence of rare-earth elements in natural fluor-apatites. *Journal of Luminescence*, **69**, 343-353.

RINTOUL, L., WENTRUP-BYRNE, E., SUZUKI, S. and GRØNDAHL, L. (2007) FT-IR spectroscopy of fluoro-substituted hydroxyapatite: Strengths and limitations. *Journal of Materials Science-Materials in Medicine*, **18**, 1701-1709.

RIWOTZKI, K. and HAASE, M. (1998) Wet-chemical synthesis of doped colloidal nanoparticles: YVO_4 : Ln (Ln = Eu, Sm, Dy). *Journal of Physical Chemistry B*, **102**, 10129-10135.

ROEDER, P.L., MACARTHUR, D., MA, X-P., PALMER, G.R. and MARIANO, A.N. (1987) Cathodoluminescence and microprobe study of rare-earth elements in apatite. *American Mineralogist*, **72**, 801-811.

RØNSBO, J.G. (1989) Coupled substitutions involving REEs and Na and Si in apatites in alkaline rocks from the Ilímaussaq Intrusion, South-Greenland, and the petrological implications. *American Mineralogist*, **74**, 896-901.

SAVOINI, B., SANTIUSTE, J.E.M. and GONZALEZ, R. (1997) Optical characterization of Pr^{3+}-doped yttria-stabilized zirconia single crystals. *Physical Review B*, **56**, 5856-5865.

SHANNON, R.D. (1976) Revised effective ionic radii and systematic studies of interatomic distances in halides and chalcogenides. *Acta Crystallographica*, **A32**, 751-767.

SHELDRICK, G.M. (1997a) *SHELXS-97, a Program for the Solution of Crystal Structures*. Univ. Göttingen, Göttingen.

SHELDRICK, G.M. (1997b) *SHELXL-97, a Program for Crystal Structure Refinement*. Univ. Göttingen, Göttingen.

SHINNO, I. (1987) Color and photo-luminescence of rare earth element-doped zircon. *Mineralogical Journal*, **13**, 239-253.

SHINNO, I. and SUGIHARA, S. (1989) Artificial luminescence center of zircon irradiated with thermal neutrons. *Mineralogical Journal*, **14**, 237-245.

SOMMER, S.E. (1972) Cathodoluminescence of carbonates, 1. Characterization of cathodoluminescence from carbonate solid solutions. *Chemical Geology*, **9**, 257-273.

SUN, L-N., YU, J-B., ZHANG, H-J., MENG, Q-G., MA, E., PENG, C-Y. and YANG, K-Y. (2007) Near-infrared luminescent mesoporous materials covalently bonded with ternary lanthanide [Er(III), Nd(III), Yb(III), Sm(III), Pr(III)] complexes. *Microporous and Mesoporous Materials*, **98**, 156-165.

SUYVER, J.F., WUISTER, S.F., KELLY, J.J. and MEIJERINK, A. (2001) Synthesis and photoluminescence of nanocrystalline $ZnS:Mn^{2+}$. *Nano Letters*, **1**, 429-433.

SUYVER, J.F., KELLY, J.J. and MEIJERINK, A. (2003) Temperature-induced line broadening, line narrowing and line shift in the luminescence of nanocrystalline $ZnS:Mn^{2+}$. *Journal of Luminescence*, **104**, 187-196.

TANAKA, M. and MASUMOTO, Y. (2000) Very weak temperature quenching in orange luminescence of $ZnS:Mn^{2+}$ nanocrystals in polymer. *Chemical Physics Letters*, **324**, 249-254.

TENNANT, W.C., CLARIDGE, R.F.C., WALSBY, C.J. and LEES, N.S. (2004) Point defects in crystalline zircon (zirconium silicate), $ZrSiO_4$: Electron paramagnetic resonance studies. *Physics and Chemistry of Minerals*, **31**, 203-223.

TERNANE, R., TRABELSI-AYEDI, M., KBIR-ARIGUIB, N. and PIRIOU, B. (1999) Luminescent properties of Eu^{3+} in calcium hydroxyapatite. *Journal of Luminescence*, **81**, 165-170.

TOBY, B.H. (2001) EXPGUI, a graphical user interface for GSAS. *Journal of Applied Crystallography*, **34**, 210-213.

TOUMI, M., SMIRI-DOGGUY, L. and BULOU, A. (2000) Crystal structure and polarized Raman spectra of $Ca_6Sm_2Na_2(PO_4)_6F_2$. *Journal of Solid State Chemistry*, **149**, 308-313.

TOWNSEND, P.D., KARALI, T., ROWLANDS, A.P., SMITH, V.A. and VAZQUEZ, G. (1999) Recent examples of cathodoluminescence as a probe of surface structure and composition. *Mineralogical Magazine*, **63**, 211-226.

WANG, Y. (2007) *Luminescence detection of the structural changes in ZnO, KTa-xNbxO$_3$ and Gd$_2$O$_3$:Eu*. p. 218. Physics Department. Beijing Normal University. Beijing.

WAYCHUNAS, G.A. (2002) Apatite luminescence. In M.J. Kohn, J. Rakovan and J.M. Hughes, Eds. *Reviews in Mineralogy & Geochemistry*, **48**, p. 701-742. Mineralogical Society of America, Washington D.C.

WEGH, R.T., DONKER, H., OSKAM, K.D. and MEIJERINK, A. (1999) Visible quantum cutting in Eu^{3+}-doped gadolinium fluorides via downconversion. *Journal of Luminescence*, **82**, 93-104.

WELLS, J-P.R. and REEVES, R.J. (2000) Polarized laser-selective excitation and Zeeman infrared absorption of Sm^{3+} centers in CaF_2 and SrF_2 crystals. *Physical Review B*, **61**, 13593-13608.

WYBOURNE, B.G. (1966) Energy levels of trivalent gadolinium and ionic contributions to the ground-state splitting. *Physical Review*, **148**, 317-327.

YANG, B., LUFF, B.J. and TOWNSEND, P.D. (1992) Cathodoluminescence of natural zircons. *Journal of Physics: Condensed Matter*, **4**, 5617-5624.

YANG, Z., FLECK, M., PERTLIK, F., TILLMANNS, E. and TAO, K. (2001) The crystal structure of natural gugiaite, $Ca_2BeSi_2O_7$. *Neues Jahrbuch für Mineralogie-Monatshefte* (4), 186-192.

YOU, F., HUANG, S., MENG, C., WANG, D., XU, J., HUANG, Y. and ZHANG, G. (2007) 4f5d configuration and photon cascade emission of Pr^{3+} in solids. *Journal of Luminescence*, **122-123**, 58-61.

ZIEGLER, J.F. and BIERSACK, J.P. (2003) *SRIM-2003-20*. (www.srim.org), Annapolis.